Osmotic Energy Harvesting using Polymeric Cation Selective Membranes

Fachbereich Material- und Geowissenschaften
der Technischen Universität Darmstadt

Zur Erlangung des akademischen Titels **Dr. rer. nat.** genehmigte Dissertation von
Muhammad Hamza Ali Haider, **M.Sc. (Hons)**,
aus Lahore, Pakistan
Darmstadt 2024 – D 17

Tag der Einreichung: 29.12.2023 Tag der Prüfung: 14.02.2024

1. Gutachten: Prof. Dr. Wolfgang Ensinger
2. Gutachten: Prof. Dr. Jan Philipp Hofmann

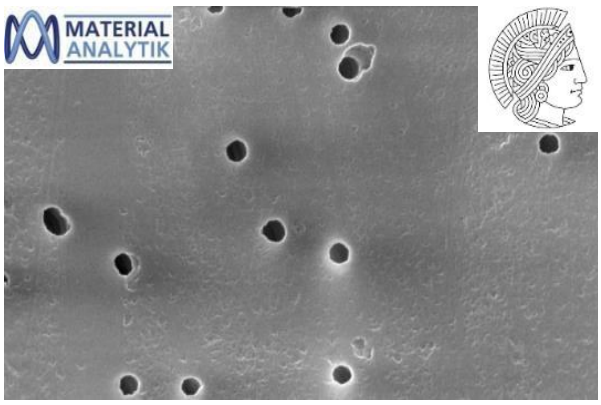

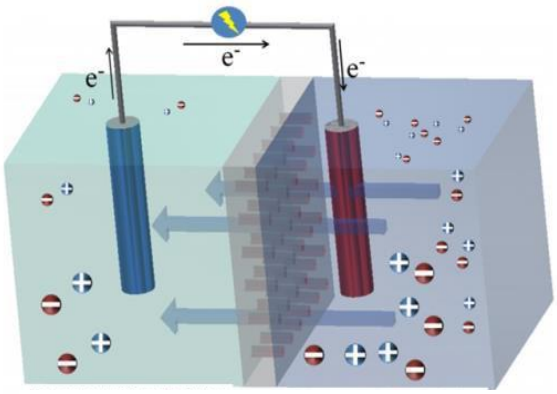

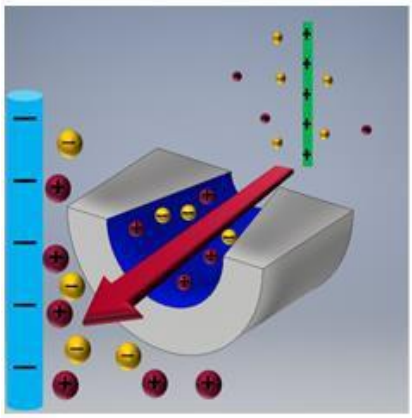

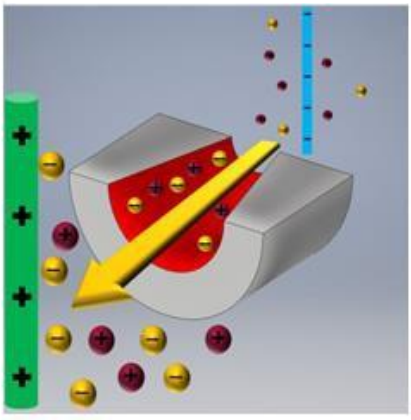

Osmotic Energy Harvesting using Polymeric Cation Selective Membranes
Osmotische Energiegewinnung mit polymeren kationenselektiven Membranen

Dissertation von Muhammad Hamza Ali Haider aus Lahore, Pakistan

Darmstadt, Technische Universität Darmstadt

1. Gutachten: Prof. Dr. Wolfgang Ensinger
2. Gutachten: Prof. Dr. Jan Philipp Hofmann

Tag der Einreichung: 29th December 2023
Tag der Prüfung: 14th February 2024

Jahr der Veröffentlichung der Dissertation in TUprints: 2024

Darmstadt 2024 – D 17

Please cite the thesis as:

URN: urn:nbn:de:tuda-tuprints-267512
URI: https://tuprints.ulb.tu-darmstadt.de/id/eprint/26751

This thesis is published by TUprints,
TU Darmstadt publication service
http://tuprints.ulb.tu-darmstadt.de
tuprints@ulb.tu-darmstadt.de

Declaration/Erklärung

I declare that this thesis has not been submitted to any other university to obtain any sort of degree. This thesis has been written independently. Some of the thesis work has already been published in journal articles. The presented data is original.

Ich erkläre, dass diese Arbeit an keiner anderen Universität zur Erlangung irgendeines Grades eingereicht wurde. Diese Arbeit wurde unabhängig verfasst. Ein Teil der Arbeit wurde bereits in Zeitschriftenartikeln veröffentlicht. Die vorgelegten Daten sind Originaldaten.

Muhammad Hamza Ali Haider
29th December 2023
Darmstadt

Acknowledgement

I would like to express my gratitude to Prof. Dr. Wolfgang Ensinger and Dr. Mubarak Ali for providing me with the opportunity to pursue my PhD at the Department of Material Analytics, TU Darmstadt. I am also grateful for their supervision and support throughout the course of my studies.

I would like to express my gratitude to Maria Walker, Dr. Tim Böttcher, Dr. Torsten Walbert, Dr. Falk Münch, Brunhilde Thybusch, Patrick Bräuer, Dr. Umme Habiba Hossain, Dr. Saima Nasir, Dr. Adnan Khalil, Marco Colombo and Dr. Khalid Amin for their assistance and help with academic and bureaucratic matters.

Finally, I would like to express my gratitude to my parents, brother and maternal aunt for providing me with the confidence and emotional support I needed throughout my studies.

Abstract

A nanopore with a charged surface can preferentially transport counterions, due to the presence of overlapping double layers. A charged nanoporous membrane can be utilised in various applications, such as heavy metal ion filtration and osmotic energy harvesting. The osmotic energy harvesting technique requires a porous membrane that performs either osmosis or selective ion transportation. The efficiency of the osmotic energy harvesting system is crucially dependent upon the membrane's performance. In this thesis, two different cation selective membranes were fabricated for the application of osmotic energy harvesting: a sub-nanometre polyimide membrane and an acrylic acid hydrogel PET membrane (HP membrane). The membranes were negatively charged and selectively transported cations down the concentration gradient. The PI membrane was fabricated using the soft-etching technique. To achieve this, PI foil with latent tracks, was immersed inside DMF solution. DMF dissolves the polymeric material within the PI foil resulting in the fabrication of the pore in the sub-nanometre range. The HP-membrane was fabricated by incorporating acrylic acid hydrogel within a porous PET support membrane with sub-micrometre-sized pores. The performances of the membranes were analysed in various conditions, e.g, various concentration folds, pH, fluence, exposure to multivalent cation and time dependent investigation. The PI membrane exhibited the highest power output of 0.45 μW, while the HP membrane exhibited the maximum power of 1.10 μW. Acidic medium and multivalent cations were extremely detrimental to the membranes. A sharp decline in power output was observed in the acidic or multivalent cation solutions. A gradual increase in the power output was observed with the increase in concentration folds but subsequently declined after a certain value of concentration fold. The power output increased up to a certain fluence, after which a decline in power was observed.

In the thesis, cation and anion transport behaviour in the negative and positively charged conical nanopore was investigated. The conical nanopore was fabricated within PET foil using the asymmetrical etching technique. Due to the etching, pore's surface carry a net negative surface charge and can be modified to positive via electrostatic self-assembly of PAH. Monovalent cations did not invert the surface charge of the unmodified conical nanopore. However, exposure to multivalent cations resulted in either surface charge neutralisation or inversion. The surface charge of the modified conical nanopore was neutralised or inverted by certain monovalent and multivalent anions such as HCO_3^-, $H_2PO_4^-$ and HPO_4^{2-}.

Zusammenfassung

Eine Nanopore mit einer geladenen Oberfläche kann aufgrund des Vorhandenseins überlappender Doppelschichten bevorzugt Gegenionen transportieren. Eine geladene nanoporöse Membran kann für verschiedene Anwendungen genutzt werden, z. B. für die Filtration von Schwermetallionen und die Gewinnung osmotischer Energie. Die Technik des osmotischen Energy Harvesting erfordert eine poröse Membran, die entweder Osmose oder selektiven Ionentransport ermöglicht. Die Effizienz des Systems zur Gewinnung osmotischer Energie hängt entscheidend von der Leistung der Membran ab. In dieser Arbeit wurden zwei verschiedene kationenselektive Membranen für die Anwendung der osmotischen Energiegewinnung hergestellt: eine Sub-Nanometer-Polyimid-Membran und eine Acrylsäure-Hydrogel-PET-Membran (HP-Membran). Die Membranen waren negativ geladen und transportierten Kationen selektiv den Konzentrationsgradienten hinunter. Dir PI-Membran wurde mit der Soft-etching-Technik hergestellt. Zu diesem Zweck wurde PI mit latenten Spuren in eine DMF-Lösung getaucht. DMF löst das polymere Material in der PI-Folie auf, was zur Herstellung von Poren im Sub-Nanometerbereich führt. Die HP-Membran wurde durch den Einbau von Acrylsäure-Hydrogel in eine poröse PET-Trägermembran mit Poren im Submikrometerbereich hergestellt. Die Leistungen der Membranen wurden unter verschiedenen Bedingungen analysiert, z. B. verschiedene Konzentrationsstufen, pH-Wert und Durchflussmenge, Exposition gegenüber mehrwertigen Kationen und zeitabhängige Untersuchungen. Die PI-Membran wies die höchste Ausgangsleistung von 0,45 μW auf, während die HP-Membran die maximale Leistung von 1,10 μW zeigte. Saures Medium und mehrwertige Kationen waren äußerst nachteilig für die Membranen. In sauren Lösungen oder Lösungen mit mehrwertigen Kationen wurde ein starker Rückgang der Ausgangsleistung beobachtet. Ein allmählicher Anstieg der Ausgangsleistung wurde mit der Zunahme der Konzentrationsfalten beobachtet, nahm aber nach einem bestimmten Wert der Konzentrationsfalten wieder ab. Die Leistungsabgabe stieg bis zu einer bestimmten Fluence an, danach wurde ein Leistungsabfall beobachtet.

In dieser Arbeit wurde das Transportverhalten von Kationen und Anionen in einer negativ und positiv geladenen konischen Nanopore untersucht. Die konische Nanopore wurde mit Hilfe der asymmetrischen Ätztechnik in einer PET-Folie hergestellt. Aufgrund der Ätzung trägt die Porenoberfläche eine negative Oberflächenladung und kann durch elektrostatische Selbstmontage von PAH in eine positive umgewandelt werden. Monovalente Kationen kehrten die

Oberflächenladung der unmodifizierten konischen Nanopore nicht um. Die Exposition gegenüber mehrwertigen Kationen führte jedoch entweder zu einer Neutralisierung oder einer Umkehrung der Oberflächenladung. Die Oberflächenladung der modifizierten konischen Nanopore wurde durch bestimmte monovalente und multivalente Anionen wie HCO_3^-, $H_2PO_4^-$ and HPO_4^{2-} neutralisiert.

Table of Content

Chapter 1. General Introduction

A ‘nanochannel’ or a ‘nanopore’ is a structure having a dimension smaller than 100 nm [1]. Note, the terms, i.e., ‘nanochannel’ and ‘nanopore’ are used synonymously in the thesis. In nature, nanochannels are encased inside a lipid layer of a cell [2]. Biological channels play a crucial role in the maintenance of osmoregulation within a cell by transporting different ions [2,3,4]. The channels within cells exhibit selectivity for specific chemical species [2]. Furthermore, the channels transition to an ON or OFF state in response to external stimuli [5]. A cell can contain three types of transporters, i.e., an uniporter, a symporter and an anti-porter [6,7]. The Uni-porter transports chemical species in one direction, the symporter transports two chemical species in a particular direction, and the antiporter is responsible for transporting chemical species in both directions, i.e., into and out of a cell [6,7].

The transport behaviour of a biological nanochannel can be mimicked in a synthetic nanochannel [5,7]. Several methods have been developed to fabricate synthetic nanopores, namely, Focused Ion Beam (FIB), Dielectric Break Through (DBT) method, Electron Beam Lithography (EBL) and Ion Track Etch method [8,9,10,11]. Nanopores can be fabricated using the FIB technique by targeting an ion beam onto a substrate target [12,13]. In the DBT technique, nanopores are fabricated in the substrate material such as Silicon nitride (SiN_x) by applying an electric field [9]. The surface of the substrate material is introduced to a concentrated salt solution and a large voltage bias is applied [9]. The electric field causes the generation of a leak current which leads to the formation of charge traps, ultimately resulting in energy dissipation and the generation of pores [9]. Prior research findings have demonstrated that nanopores having an average diameter of 2nm have been fabricated in SiN_x using the DBT technique [9]. The EBL technique is also an important technique used for the fabrication of nanopores, where a resist (pattern) is coated to a substrate surface, which is then targeted by an electron beam [10,14]. The Ion-track etch method is the established technique for the fabrication of nanopores within a polymer material [15]. The method is regarded for its versatility in geometry and pore size. Moreover, a pore with a suitable surface functionalisation can be used for several applications [16]. Several different nanopore morphologies such as cylindrical, cigar-shaped and conical have been reported in the previous literature [17,18].

Some of the sentences, paragraphs and diagrams in this chapter of the thesis were already published in the following journal articles
“**Osmotic energy harvesting with soft-etched nanoporous polyimide membranes** || ***M.H.A. Haider***, *S. Nasir, M. Ali, P. Ramirez, J. Cervera, S. Mafe, W. Ensinger* || https://doi.org/10.1016/j.mtener.2021.100909

“**Anions effect on ion transport properties of polyelectrolyte modified single conical nanopores**” || ***M.H.A.Haider***, *M. Ali, W. Ensinger* || https://doi.org/10.1016/j.cplett.2021.138349

Synthetic nanopores have better mechanical and thermal properties compared to biological nanopores [19]. In addition, synthetic nanopores can be easily integrated into a working device [19]. Due to the aforementioned properties of synthetic nanopores, they can be used in diverse applications such as energy harvesting, sensors and filtration [20,21]. In addition, a nanoporous membrane can also be used to sieve out particles. The surface of nanopores can also be chemically functionalised to detect chemical species [23].

Charged nanopores can be used for the application of reverse electrodialysis (RED). The charged nanopore permits the diffusion of counterions and impedes the diffusion of coions when exposed to a concentration gradient, resulting in the generation of current [22]. Furthermore, negatively charged nanopores can also be used to filter heavy metal ions. Most heavy metal ions are positively charged and therefore form strong interactions with a negatively charged surface.

To date, approximately 80% of electricity is produced from fossil fuels. The substantial usage of fossil fuels is leading to global warming [24]. The average temperature of the earth is rising leading to the melting down of glaciers and sea level to rise [25]. Moreover, climate change and alterations in the natural rain cycle are creating adverse effects on the agriculture sector. The change in geopolitical circumstances affects the price of fossil fuels. The increase in the price of fossil fuels puts severe financial strain on developing countries. Over time, the increase in industrialisation and the world's population have escalated the demand for electricity. Factor such as dwindling oil reserves, surge in energy demand, and global warming are pushing governments to invest in alternative and renewable energy.

Presently, 22% of the total electricity production is obtained from renewable sources of energy, such as solar, wind, hydal and tidal [26,27]. The alternative energies offer advantages in terms of affordability, zero-emissions and renewable fuel [28]. To date, several devices have been developed that can convert other energy sources into electricity such as radio frequency (RF), thermal, pressure and salinity gradient (SGE) [29].

The SGE technique converts the energy resulting from difference in fluid concentration into electrical energy [30,31]. The SGE method generates clean energy and is independent of weather conditions, and according to an estimate, a large amount of electrical power, 2TW, can be obtained through the technique [30]. Pressure retarded osmosis (PRO) and RED are the examples of SGE [32].

1.1 Motivation and aim

The quality of a membrane used in an osmotic energy harvesting set-up determines the overall efficiency of the set-up. Therefore, considering the aforementioned statement, the primary aim and objective of the thesis was to fabricate cation selective membranes that improve the performance of the set-up. The performance of a membrane can be improved either by increasing the surface charge density or by reducing the pore size. In this respect, two different membranes were fabricated: a polyimide (PI) membrane with sub-nanometer pore size and a composite membrane of polyethylene terephthalate (PET) and acrylic acid hydrogel. The PI membrane with sub-nanometer pore size was initially documented by Ensinger et al [33]. An organic etching solution was used to fabricate sub-nanopores within the PI membrane. The pore size of the PI membrane was relatively small, therefore it can be predicted that the membrane would have superior cation selectivity, ultimately leading to a higher performance. The second type of membrane was prepared by incorporating acrylic acid hydrogel into the porous PET support membrane. The acrylic acid hydrogel has numerous carboxylic acid groups, which leads to a higher charge density of the membrane. Increasing the charge density of a membrane improves the performance of the osmotic energy harvesting set-up. In addition, the thesis aimed to evaluate the performance of the membranes under different conditions which include fluence dependent test, time dependent test and pH test. The performance of the membranes was also investigated by exposing them to a multivalent cation. In previous literature, researchers have predominantly used single nanopore membranes or membranes with small exposed test areas. However, in this thesis, a relatively larger test area (approximately 100 mm^2) was used. Moreover, the ion transport behaviour within the membranes was also part of the study.

Another aim and objective of the thesis was to investigate the cation and anion transport behaviour within a single conical nanopore in the PET membrane. The study examined the ion transport behaviour in the positively and negatively charged nanopores. The influence of pH on the ion transport behaviour within the conical nanopore was also investigated.

1.2 Latent track formation

Swift Heavy Ion Irradiation (SHI) is the process used to fabricate latent tracks within a polymer sample [34,35]. During the process, ions achieve a speed of 4.5 x10^7 m/s [34]. The universal accelerator (UNILAC) set-up illustrated in Figure 1 includes a magnetic lens, a high frequency ion accelerator, an electrostatic deflector and an ion detector [34]. The incident atoms are stripped of their electrons and accelerated by the high frequency ion accelerator. The magnetic lens regulates the fluence of the latent tracks within a polymer substrate [34]. The fluence normally is in the range of 1 to 10^{12} ions/cm^2. A metal sheet with a 200 microns diameter hole is placed in front of a polymer sample to fabricate a single track within a polymer foil [34]. The ions pass through the sample before hitting the metal detector (Faraday cup) [34,35].

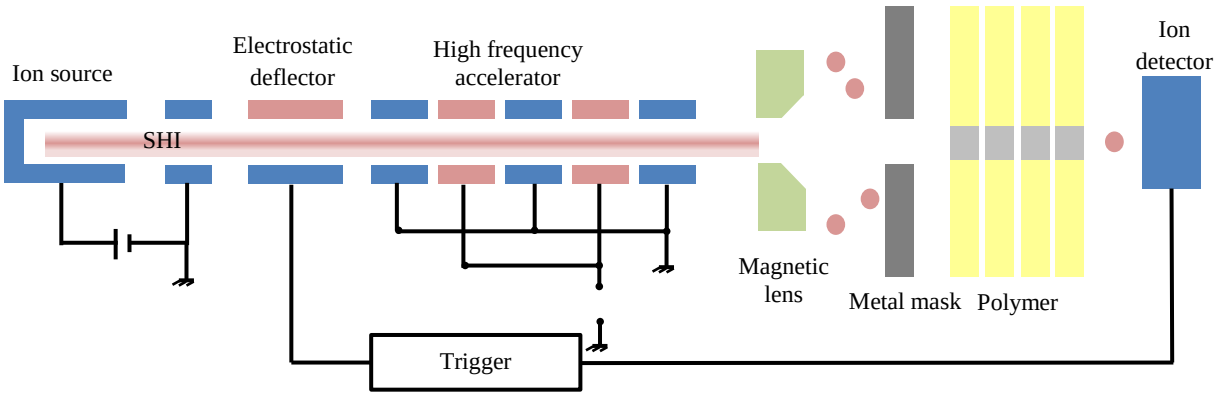

Figure 1: Schematic representation of fabrication of the single latent track within polymeric foils using the Universal Linear Accelerator (UNILAC) located at GSI [34].

The incident beam loses kinetic energy through nuclear energy loss and electronic energy loss [35]. With the increase in energy of the incident ions beam, the proportion of electronic energy loss becomes more significant [35]. The total energy loss saturates after reaching a certain threshold value [35]. The penetration depth of the incident beam increases with the increase in its energy [35].

The fabrication of a latent track within a target polymer substrate results from the cleavage of polymeric bonds [34,35]. Additionally, secondary electrons are emitted from the atoms as a result of the collision [34,35]. The secondary electrons trigger radical formation and chemical reactions in the area (halo area) adjacent to the tracks [35]. The halo region is comparatively more reactive

and crosslinked than the bulk region [35]. The quality of track formation depends upon the strength of the bonds present in a polymer substrate [34,35]. According to the literature, the quality of the tracks formed in polycarbonate (PC) and polyethylene terephthalate (PET) is of superior quality compared to those formed in polyimide (PI) [35]. This is due to the presence of ester bonds in PC and PET which are easily broken off during the irradiation process [35].

1.3 UV sensitisation

After undergoing the irradiation process, the polymer substrates are kept in the open air. The substrate undergoes an oxidation reaction which subsequently increases the reactivity of the substrate [35]. A further improvement in the reactivity of the substrate is achieved by the Ultraviolet (UV) sensitisation process [36]. In the process, the polymer foils are irradiated with UV rays having wavelength below 320 nm. According to the literature, UV irradiation triggers a photo-oxidation reaction which subsequently increases the chemical reactivity of the substrate [37,38].

1.4 Chemical etching

The nanochannels or nanopores are fabricated within a polymer substrate using the chemical etching technique. In the technique, the substrate is exposed to an inorganic etchant heated to a specific temperature. The etchant dissolves the material within and adjacent to the tracks by breaking the polymer bonds, e.g., ester bonds in PC and PET (Figure 2) [35]. The selection of an etchant depends on the polymer sample, e.g., sodium hydroxide is used to etch PC and PET, whereas PI polymer samples are etched with sodium hypochlorite solution [39,40]. The concentration and temperature of an etchant contribute to the etching rate and the symmetry of a nanopore [41].

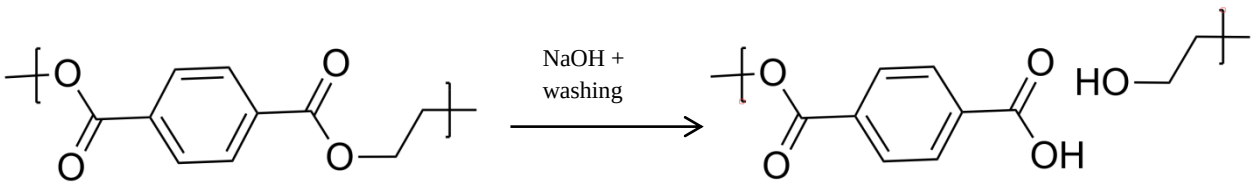

Figure 2: Scheme showing the cleavage of ester bond during chemical etching of PET [35].

The etching rate of the bulk material and the track are different, leading to discrepancies in reactivity as depicted in Figure 3 [35]. The tracks have higher reactivity than the bulk material.

As a result, when the polymeric foil is exposed to an etchant solution, the etching rate of the tracks is far greater compared to the bulk material [35]. The ratio between two etching rates can be computed through equation 1 [35]. A cylindrical nanopore is obtained when the track etch rate is substantially higher compared to the bulk etch rate, whereas a conical nanopore is obtained when both of the etching rates have evenly matched values [35].

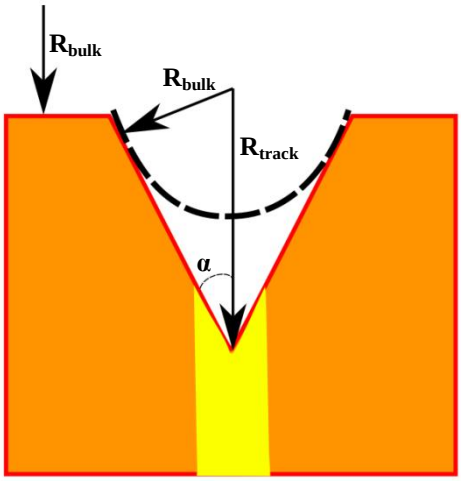

Figure 3: The scheme illustrates the etching procedure with two distinct etching: bulk etching and track etching [35].

$$\sin\alpha = \frac{bulk\ etching\ rate(R_{bulk})}{track\ etching\ rate(R_{track})} \quad (1)$$

The track etching technique is a quite flexible in terms of pore geometry and size. Several shapes such as conical, cylindrical, bullet-shaped and dumbbell-shaped nanopores can be fabricated using the track etching technique [42-45].

The illustration in Figure 4a shows a cylindrical nanochannel inside a PET foil. The nanochannel can be fabricated by exposing the foil to 2M NaOH etchant, which is heated to a temperature close to 50 ^{o}C during the process [35].

The asymmetrical etching technique is used to fabricate conical nanopores [42]. Figure 4b illustrates the conical nanopore fabricated in a polymer foil. In the process, a surface of the polymeric foil is introduced to a concentrated etchant solution and the other one to stopping

solution [42]. The stopping solution is composed of a weak acid and a salt solution and its purpose is to neutralise the etchant solution, thereby reducing the etching rate.

Surfactants are added to an etchant solution to fabricate a cigar-shaped nanopore (Figure 4c) [46]. The surfactant molecules adsorb onto the polymer surface, thereby reducing the etching rate at the surface, while leaving the rate of etching at the core remained unaffected [46]. This difference in etch rate between the core and the surface lead to the formation of cigar-shaped nanopore.

Figure 4d depicts a bullet-shaped nanopore. In the nanopore fabrication process, one end of a polymer foil is introduced to an etchant solution while the other end is introduced to a solution mixture that comprises of a surfactant and an etchant solution [44].

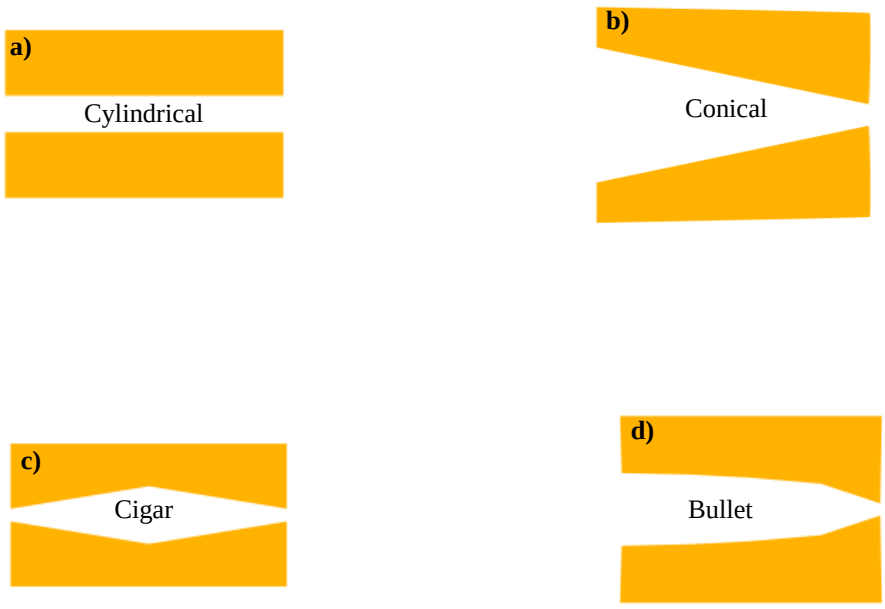

Figure 4: Different shape of nanopores (a) Cylindrical (b) Conical (c) Cigar-shaped (d) Bullet-shaped.

Dumbbell-shaped nanopores are fabricated by a two-step etching process [45]. Initially, a polymer foil is exposed to a concentrated etchant solution, resulting in the formation of two cones on both sides of the foil, as depicted in Figure 5a. In the second step, the polymer foil is exposed to a low concentrated etchant solution at an elevated temperature [45]. The channel formed connects the two cones, thereby resulting in an overall dumbbell-shaped nanopore, as shown in Figure 5b.

Figure 5: Schematic representation of different steps for the fabrication of dumbbell-shape nanopore (a) 1st step when a polymeric foil is exposed to a high concentrated etchant solution (b) 2nd step of the fabrication process in which the polymeric foil is exposed to a low concentrated etchant solution.

1.5 Electrical double layer

When a charged object is immersed inside an aqueous solution, an Electrical Double Layer (EBL) is formed adjacent to the surface, as depicted in Figure 6 [47]. The Stern layer model can explain the EBL; according to the model, counterions and coions are arranged in a particular manner around the charged surface [48]. The innermost layer is known as Stern layer, which comprises of Inner Helmholtz Plane (IHP) and the Outer Helmholtz Plane (OHP) [48]. Diffuse layer adjoins the Stern layer where the ions and have considerable degree of movement [48]. On the other hand, counterions are strictly constrained inside the IHP layer whilst the OHP layer comprises of tightly constrained hydrated ions [48]. The thickness of the Stern layer and the diffuse layer depends on the concentration of a salt solution. The electric potential at the interface of diffuse layer and bulk solution is at its minimum and increases exponentially with lateral distance (according to the Figure 6) [49]. The ions in the salt solution experience repulsion or attraction due to the potential of the charged surface.

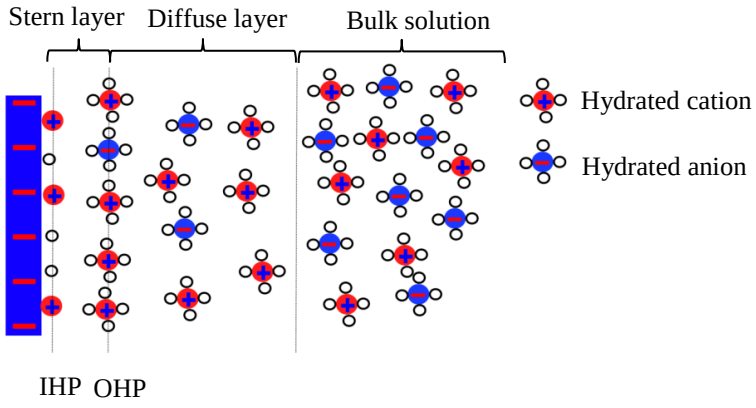

Figure 6: Schematic representation of Electrical Double Layer. Various layers are illustrated, i.e., Inner Helmholtz plane, Outer Helmholtz plane, Diffuse layer and Bulk solution [48].

1.6 Nano-fluidic pores

The study of fluid flow in a nanoscale channel is known as nano-fluidics [50]. The surface of the nanochannel within PI, PET and PC is negatively charged after the etching process [40,51,52]. An EDL is formed adjacent to the charged surface of a nanochannel upon immersion in a salt solution [50]. The selectivity of a nanochannel depends upon the thickness of the Debye length [50]. A charged nanochannel selectively transport counter ion preferentially due to their comparable radius with the Debye length [50]. Due to the selective transport of counterions, the concentration of counterions builds up within the nanochannel, as illustrated in Figure 7 [53]. Conversely, the concentration of anions within the nanochannel is lower compared to the bulk solution, as depicted in Figure 7 [53]. The concentration of ions near both ends of the nanochannel remains approximately constant at 0V [53]. Applying a voltage bias causes a build-up of cation's concentration at one end and depletion on the other end, resulting in a concentration difference [53]. The concentration gradient intensifies as the magnitude of the voltage increases [53]. Furthermore, due to the voltage bias, the solvent molecules follow the electromigration trajectory of the majority charge carrier (cations) due to collisions between the cations and the solvent molecules [53]. The motion of the molecules under the influence of voltage is called electroosmotic flow [53].

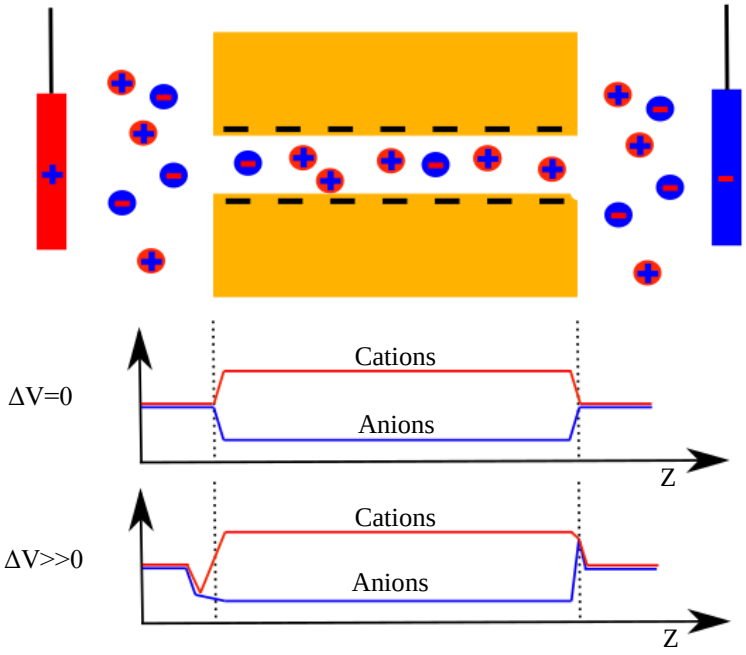

Figure 7: Scheme illustrating the selective transport of cations, moreover the graphs show the concentration profile of cations and anions at different axial positions [53].

The ionic conductance of a channel depends on the bulk solution concentration, charge density, and the diameter [50]. In the case of a nanochannel, below a critical value of the concentration of a bulk solution, the conductance is mainly influenced by the charge density [50]. Nonetheless, above the critical value, the conductance is influenced by the conductivity of a salt solution and the channel's diameter [50]. A microchannel with a charged surface carries out negligible preferential transport of counterions due to the low Debye length to diameter ratio (Figure 8) [50]. As a result, it demonstrates dissimilar transport behaviour to that of a nanochannel [50].

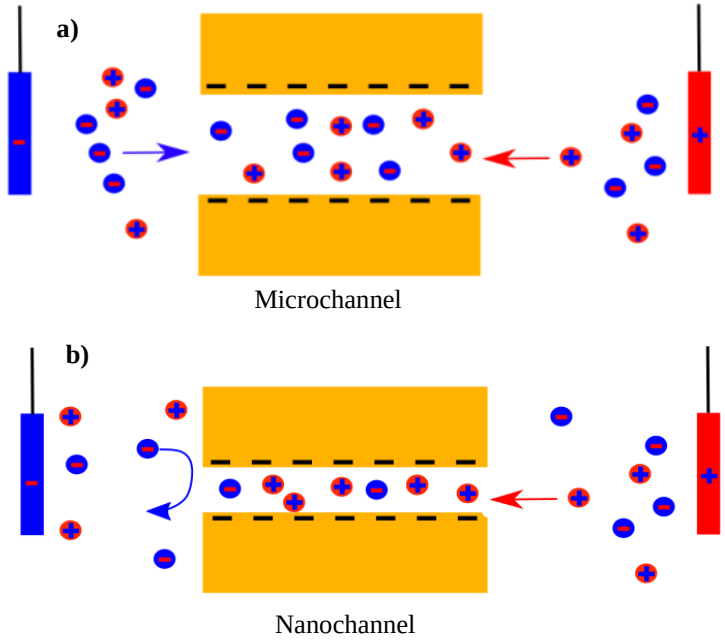

Figure 8: (a) Ions transport inside a microchannel (b) Ions transport inside a nanochannel.

The Debye length has an inverse relationship with the concentration of an electrolyte [54]. The increment in the concentration increases the electric field screening, which in turn decreases the Debye length, causing the nanochannel to lose its selectivity for counterions (Figure 9) [54]. Another theory also provides the explanation for the decrease in counterion selectivity of a nanochannel when exposed to a high salt concentration. The second theory suggests a decreased Dukhins number due to the increase in an electrolyte concentration, resulting in a lower selectivity according to equation 2 and 3 [50]. Multivalent counterions have a higher affinity for the surface charges, resulting in strong adsorption of the ions on the surface, leading to surface charge neutralisation or surface charge inversion, which subsequently reduces counterion selectivity. However, in certain cases, the net surface charge is reversed due to the strong interactions of multivalent counterions with surface charges.

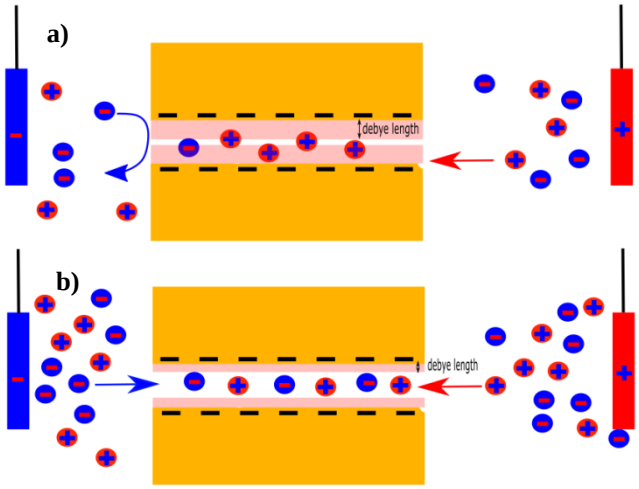

Figure 9: Scheme illustrating Debye length in (a) low concentrated electrolyte salt solution, cations are preferentially transported across the nanochannel (b) high concentrated salt solution, no preferential selectivity is observed.

$$f(perm) = 1 + 2Du \qquad 2)$$

$$Du = \frac{\sigma}{(C * R)^1} \qquad 3)$$

f: Permselectivity
Du: Dukkhins Number
C: Concentration of electrolyte
R: Radius of channel
σ: Surface charge

1.7 Ion current rectification

A symmetric nanochannel exposed to a symmetric salt solution exhibits a linear current-voltage (*I-V*) curve. However, a non-linear *I-V* behaviour can be observed by introducing an asymmetry in the system, the non-linear *I-V* behaviour is known as ion current rectification (ICR) [50]. The ICR phenomenon can be manifested by the introduction of asymmetry in the shape of the nanopore, asymmetric charge distribution and concentration gradient [50].

In Figure 10 a(i and ii), the asymmetry in the charge density is introduced [50]. The right hand side (RHS) of the nanochannel has a positively charged surface, whereas the left hand side (LHS) has a negatively charged surface, as illustrated in Figure 10a(i and ii) [50]. When the RHS end is facing the cathode (negative) whereas the LHS is facing the anode (positive) (Figure 10a(i)), the

nanochannel is in the ‘ON’ state [50]. At the RHS, anions can easily enter the nanochannel while cations are repelled [50]. On the other hand, the negative charges present at the LHS facilitate the entry of cations into the nanochannel [50]. Ions experience repulsion at the centre of the nanochannel where the surface charges switch, and thus making it difficult for the ions to exit the nanochannel [50]. Consequently, the ionic concentration inside the nanochannel increases due to the ease of entrance and difficulty of exiting leading to increase of current [50]. On the other hand, the nanochannel transitions into the ‘OFF’ state when the sign of the potential difference (P.D) is reversed, as illustrated in the Figure 10a(ii) [50]. In the ‘OFF’ state, cations and anions are attracted to the negatively and positively charged electrodes, respectively. Ions can easily exit the nanochannel but face difficulty during the entrance, leading to a depletion of the ionic concentration within the nanochannel [50]. Consequently, the resistance value of the nanochannel is increased, resulting in a low current value [50].

In the second case scenario, a nanochannel is introduced to a concentration gradient, as illustrated in Figure 10b(i) [50]. It is assumed that the surface of the nanochannel has a net negative charge, allowing only cations to migrate through the nanochannel [50]. The nanochannel is considered to be in the ‘ON’ state when both the migration flux and the diffusion flux occur in the same direction, i.e., down the concentration gradient, as depicted in Figure 10b(ii) [50]. The nanochannel transitions to the ‘OFF’ state when the polarity of P.D is reversed, causing the direction of the migration flux to oppose the direction of the diffusion flux [50]. In the ‘OFF’ state, the diffusion of cations decreases, resulting in low current values [50].

Ion current rectification can also occur by breaking the symmetry of a nanochannel, e.g., a conical nanopore [50,55]. The negatively charged nanopore is in the ‘ON’ state when the tip is facing the positively charged electrode (Figure 10c(i)) [55]. On the other hand, the nanopore transitions to the ‘OFF’ state when the polarity of the P.D is reversed (Figure 10c(ii)) [55]. In the ‘ON’ state, cations selectively migrate from the tip to the base. The magnitude of the current decreases in the ‘OFF’ state, and negative charges present on the surface prevent anions from entering into the nanopore [55]. Furthermore, the emergence of electrical potential cation trap impedes the cations from electromigrating, resulting in low current value [56].

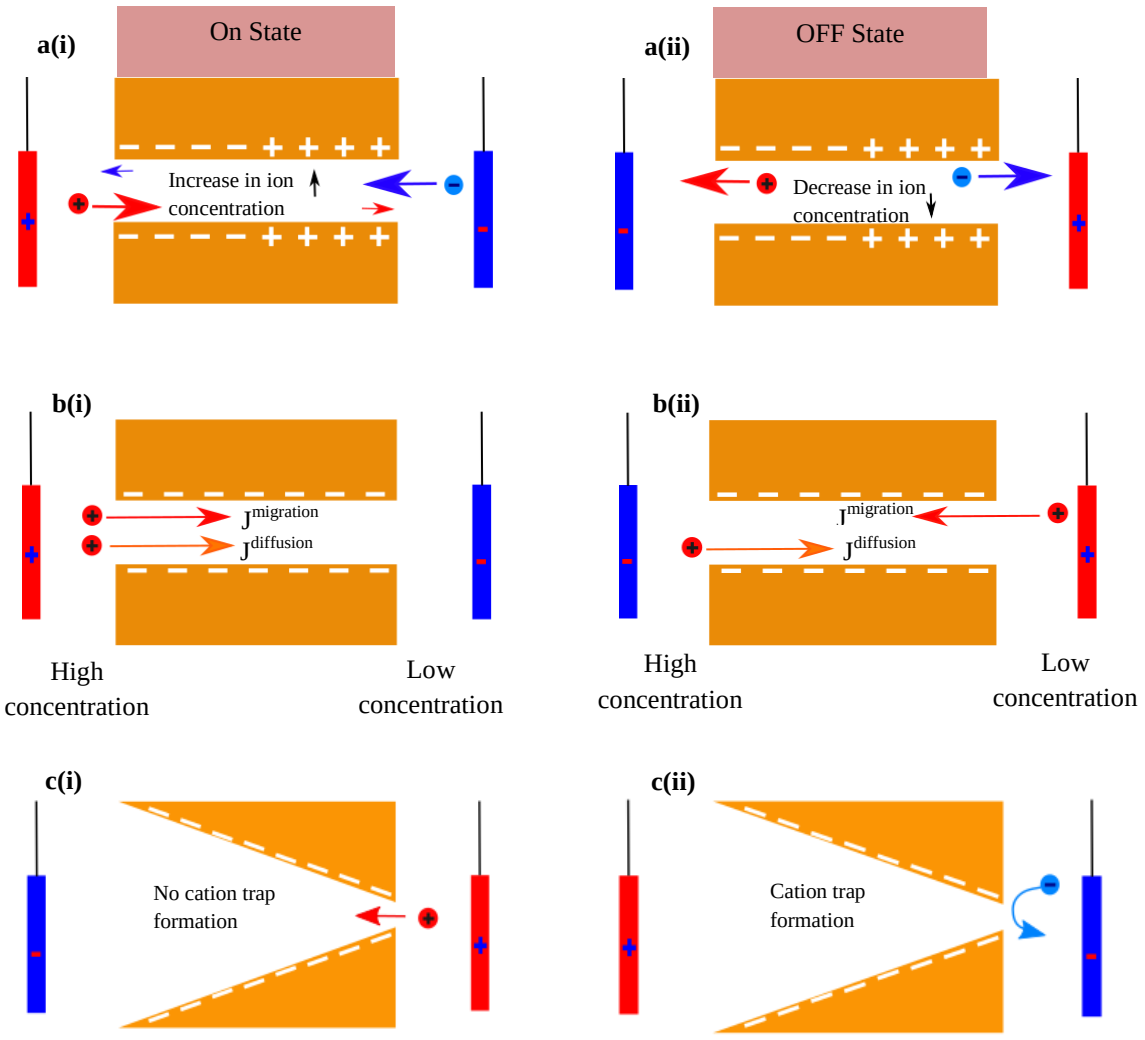

Figure 10: Schematic illustration of a nanochannel having an asymmetric charge distribution a(i) ON state a(ii) OFF state. The nanochannel was exposed to a concentration gradient b(i) ON state b(ii) OFF state. Conical shaped nanopore in c(i) ON state c(ii) OFF state [50].

The conical nanopore generates an asymmetric *I-V* curve, while the cylindrical nanopore generates a linear straight line. The rectification was quantified by the rectification factor (RF), which was calculated using the following equations 4 and 5 in the study [55].

$$RF = \frac{|I_{(+2V)}|}{|I_{(-2V)}|} \quad I_{+2V} > I_{-2V} \qquad 4)$$

$$RF = \frac{I_{(-2V)}}{I_{(+2V)}} \quad I_{+2V} < I_{-2V} \qquad 5)$$

1.8 Functionalisation of nanopore surface

Surface modification or surface functionalisation is necessary to tailor material properties to a particular application or to improve performance [34]. Functionalisation is applied in a wide variety of areas, such as biomaterials, membranes, and nanoparticle surface modification [34].

The surface of nanochannels within PET, PC and PI membranes is negatively charged due to the presence of carboxylate ions. Electrostatic self-assembly method, covalent coupling method and metal ion complexation are the methods used to functionalise the surface of a nanochannel [34,55]. By tailoring the surface, the polymer membrane can be used in sensing applications. The charges on the nanopore surface can be switched to positive by suitable adsorption of a polyelectrolyte such as poly(allylamine hydrochloride) (PAH) [55]. PAH can adsorbed on a nanochannel's surface using the electrostatic self-assembly method, as depicted in Figure 11a [55]. In this method, a polymeric membrane is submerged in the polycationic solution. The positive charges present on the polymer chains experience a force of attraction and are adsorbed on the surface of the nanochannel [55]. The adsorption of a polyelectrolyte depends on several factors such as the pore's diameter, net charge and the weight of polyelectrolyte [55].

Surface functionalisation, such as carbodiimide coupling, can be achieved by the covalent coupling method [34]. The method is carried out at low pH values. Initially, the polymer membrane is immersed in a solution of EDC (1-3-Dimethylaminopropyl-3-ethylcarbodiimide hydrochloride), a vital step for the activation of the carboxylic acid groups and later treatment with pentaflourophenol (PFP) (Figure 11b) [34].

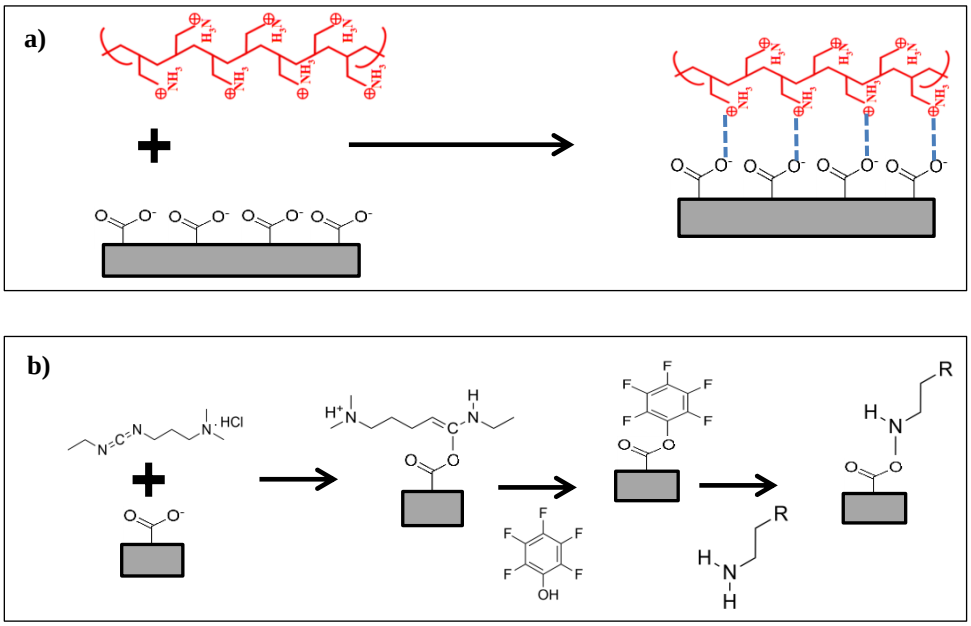

Figure 11: (a) Electrostatic self-assembly functionalisation of PAH on a surface having carboxylic acid groups (b) Carbodiimide functionalisation on a surface possessing carboxylic acid groups [34,55].

1.9 Pressure retarded osmosis

Pressure retarded osmosis (PRO) is a method of generating electricity using a salinity gradient [57,58]. The PRO set-up consists of two compartments: a high concentrated salt solution compartment and a low concentrated salt solution compartment, with a semipermeable membrane separating the compartments, as illustrated in Figure 12 [59]. The fluids are continuously pumped into their respective chambers [59]. The net osmotic pressure in the system is greater than the net hydrostatic pressure, allowing osmosis through the semipermeable membrane, resulting in an increased flow level within the high concentrated salt chamber [59]. Consequently, the increased volumetric flow in the concentrated chamber is used to drive a turbine that generates electricity, and some of water is diverted to the pressure exchange chamber [59]. The system offers several benefits: firstly, the energy demand of the reverse osmosis (RO) process is minimised when integrated with the PRO set-up, and secondly, the process lowers the concentration of the salt solution discharged by the RO process before disposing into a sea [59]. The downsides of the PRO process are energy efficiency and the integration of components, e.g., turbine, and pressure chamber [59].

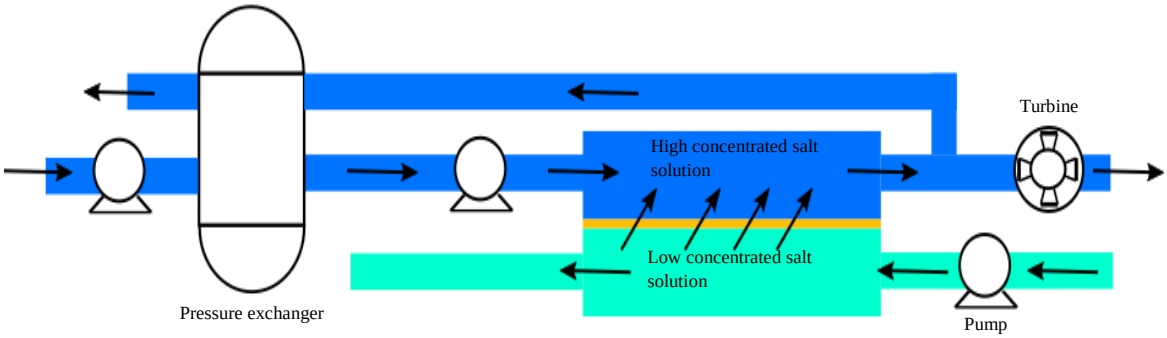

Figure 12: The scheme illustrates the set-up of pressure retarded osmosis. The set-up consists of turbine, pump, pressure exchange and membrane (indicated with yellow colour) [59].

1.10 Reverse electrodialysis

Reverse electrodialysis (RED) is a process for the generation of electric power using a salt concentration gradient [60]. The RED process set-up, illustrated in Figure 13, consists of several compartments filled with salt solution of varying concentrations [60]. The compartments are separated by porous ion-selective membranes. The membrane exclusively transports counterion due to the surface is charged and the average pore size is in the nanoscale [60].

The efficiency of the RED set-up is substantially influenced by the efficiency of the membrane. The performance of the membrane is evaluated by two parameters: counterion selectivity and ionic transmembrane resistance. Counterion selectivity is defined as the degree to which membrane allow the preferential transport of counterions over total flow of ions across the membrane, and is determined in the case of cations using equation 6 [61]. The value of counter ion selectivity is determined by temperature, pore size, concentration gradient, and charge density of the membrane. A small average pore diameter and a high surface charge density increase the reversal potential and counterion selectivity. Moreover, low ionic transmembrane resistance is desired to obtain high performance. The ionic transmembrane resistance is governed by the average pore size, fluence, exposed area of the membrane and concentration gradient. Previous literature suggests that high pore density, large exposed area and a high concentration gradient result in a low power density due to a phenomenon called concentration polarization (CP) [57, 61]. In the CP phenomenon, counterions accumulate near the one side of a membrane and deplete

on the other side, resulting in a high transmembrane flux resistance [57]. Maximum power (P_{max}) and maximum efficiency (η_{max}) were calculated using equation 7 and 8, respectively [61].

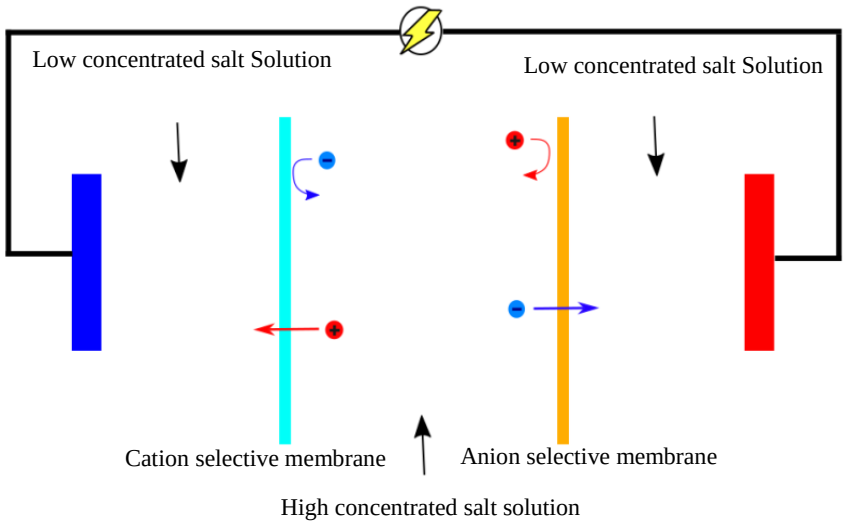

Figure 13: The schematic illustrate RED set-up. The set-up comprises of low concentrated salt solution compartment, high salt solution compartment, cation selective membrane, anion selective membrane and electrodes.

$$t_+ = \frac{1}{2}\left[1 + \frac{nF}{RT}\frac{E_{diff}}{\ln(\frac{a_H}{a_L})}\right] \quad (6)$$

$$P_{max} = \frac{E_{diff} * I_o}{4} \quad (7)$$

$$\eta_{max} = \frac{(2t_+ - 1)^2}{2}100 \quad (8)$$

t_+: Cation transport number (counter ion transport number)
E_{diff}: Differential potential or reversal potential
F: Faraday constant
R: Boltzmann constant
T: Temperature
a_H : Activity of high concentrated salt solution
a_L : Activity of low concentrated salt solution
P_{max}: Maximum power output
η_{max}: Maximum efficiency
n: Valency of cation

1.11 Electrodialysis

Electrodialysis (ED) operates oppositely to the RED [62]. ED is the energy powered process used for desalination of water [62]. The set-up consists of anion and cation selective membranes that separate compartments. The compartments are continuously fed with low and high molarity salt solutions (Figure 14) [62]. Electrodes are immersed in the salt solutions, and a potential difference (P.D) is applied. The P.D is maintained above a critical value to allow the transport of counterion against the concentration gradient to overcome the diffusion.

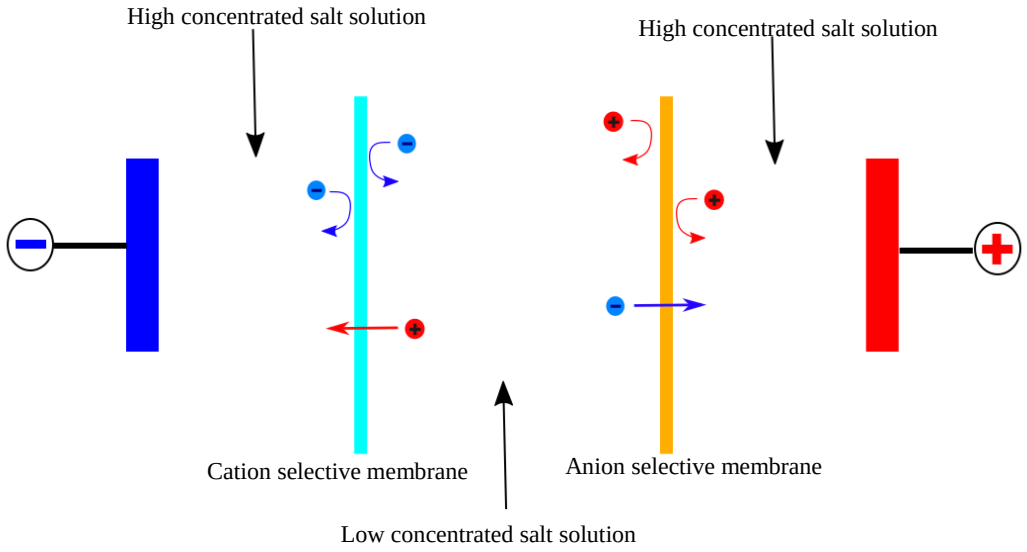

Figure 14: Schematic illustration of ED set-up. The set-up comprises of low concentrated salt solution compartment, high concentrated salt solution compartments, cation and anion selective membrane. The cations and anions migrate towards high concentrated salt solution compartments.

1.12 Hydrogels

Hydrogels are extensively crosslinked polymeric structures with hydrophilic properties (Figure 15) [63,64,65]. The hydrophilicity of the structures is attributed to the polar functional groups attached to the polymeric chains, which enable them to retain water [63,64,65]. When the hydrogel is immersed inside the water, it swells and retains more water than its dry mass [65]. Hydrophilic hydrogels can be used in various applications such as biomedical, optical, sensor, energy harvesting, agriculture, and drug delivery [63,64]. Functional groups within a hydrogel can be tuned to make it responsive to a specific external stimulus [65]. A normal conventional hydrogel has low toughness, however, the incorporation of nanoparticles and plasticisers can

improve the toughness [63]. Several different methods can be utilised for the fabrication of hydrogel, i.e., bulk, solution and suspension polymerisation [65].

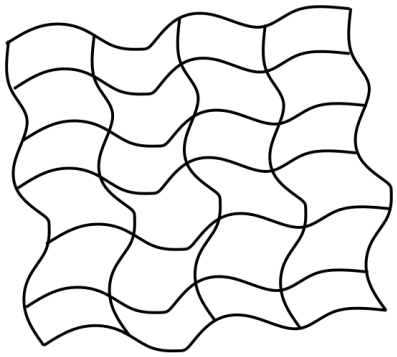

Figure 15: The scheme illustrates a cross networked polymeric hydrogel structure.

The monomer solution is the key component in bulk solution polymerisation. The solution is supplemented with some additional chemicals, namely cross-linking agent and polymerisation-reaction-initiator [65]. The crosslinking agent increases the crosslinking between polymeric chains within a hydrogel, consequently increasing the mechanical properties of a hydrogel [65]. Conversely, a high content of crosslinker reduces water retention capacity of a hydrogel. The polymerisation reaction is initiated by the polymerisation-reaction-initiator, which is triggered by external stimuli such as heat or light [65]. In the solution polymerisation method, an additional solvent, e.g, water is added to the reaction mixture (monomer, crosslinking agent, and initiator) [65]. In suspension polymerisation method, the reaction mixture is suspended in an organic phase using a stirrer [65]. After the reaction, small hydrogel beads are formed [65]. The morphology and size of the beads are influenced by various factors such as the stirrer's speed, the type of monomer used and the organic dispersant [65].

In the current research work, the hydrogels were synthesised by the solution polymerisation method. The polymerisation chain reaction was activated by a photoinitiator that absorbs a certain wavelength of light and transforms into the radical and consequently starts a chemical initiation reaction involving the radicalisation of a monomer molecule. This is followed by chain propagation, in which monomer molecules join to form a polymeric chain. The final stage is the termination step which marks the end of the reaction. The experimental set-up for the photo-

initiating reaction is straightforward compared to the set-up of a thermal-initiating reaction. A small quantity of photoinitiator reaction is added to the reaction mixture. Adding a large quantity of the initiator to the reaction mixture might result in a shorter chain length.

Chapter 2. Experimental

2.1 Swift heavy ion irradiation

PET and PI membranes were used extensively in the current research. The average thickness of the PET and PI membranes used in the study was 12 µm and 13 µm respectively. The aim was to fabricate nanochannels within the polymer foil. Prior to the SHI process, the pristine polymer foils were cut into circular shapes with an average diameter of 30 mm. Later, 6 to10 circular polymer foils were placed stacked on each other and placed in a sample holder and subsequently, the sample holder was placed in a magazine as shown in Figure 16 [34].

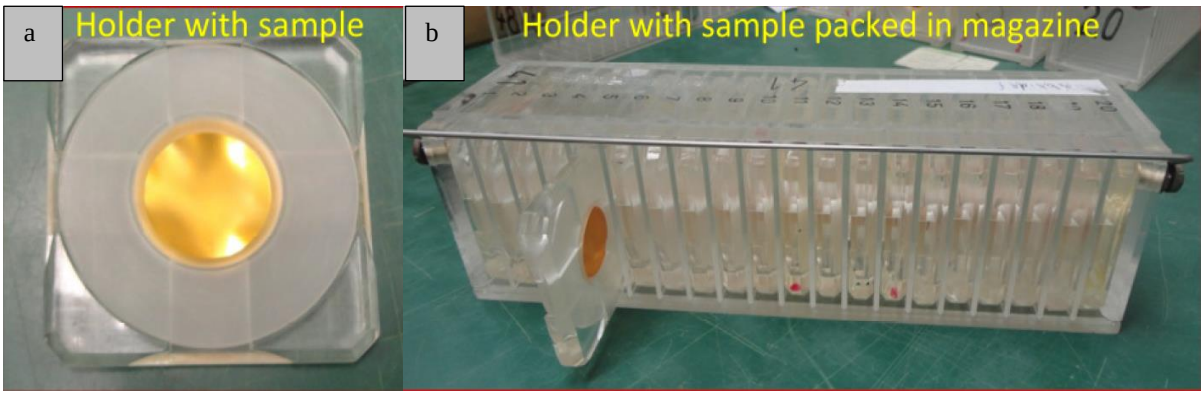

Figure 16: (a) Polymer sample holder (b) The placement of sample holders within a magazine [34]. Courtesy of Dr. Saima Nasir.

The SHI process was used to fabricating latent tracks within polymer foils in UNILAC set-up, located at GSI facility, Darmstadt [34]. The magazine containing the polymer samples was placed inside the UNILAC and heavy ions were bombarded onto the polymer samples. Gold (Au), Uranium (U), and Krypton (Kr) heavy ions were used for the irradiation purpose [34]. The beam with the energy of 11.4MeV/n was bombarded perpendicular to the surface of the polymer foils to fabricate parallel latent tracks [34]. In some cases, the beam angle was changed to 45^{o} with respect to the polymer surface to fabricate networked latent tracks.

Swift heavy ions irradiation was performed by Prof. Dr. Christina Trautman and Prof. Dr. Maria Eugenia Toimil Molares at GSI Darmstadt facility.

Some of the sentences, paragraphs and diagrams in this chapter of the thesis were already published in the following journal articles
"**Osmotic energy harvesting with soft-etched nanoporous polyimide membranes** || ***M.H.A. Haider***, *S. Nasir, M. Ali, P. Ramirez, J. Cervera, S. Mafe, W. Ensinger* || https://doi.org/10.1016/j.mtener.2021.100909

"**Anions effect on ion transport properties of polyelectrolyte modified single conical nanopores**" || ***M.H.A. Haider***, *M. Ali, W. Ensinger* || https://doi.org/10.1016/j.cplett.2021.138349

A single latent track was fabricated within a polymer sample by placing a sheet metal having a slit opening of 0.2 mm diameter. All of the samples subjected to the irradiation process were consequently stored in the open air for a limited period.

2.2 UV sensitisation

After the SHI process, each side of the polymer samples was sensitised for at least 1 hour with UV rays (VILBER UV instrument) having a wavelength of 312 nm (Figure 17). Due to the UV irradiation, the polymer samples undergo a photochemical reaction; therefore, the chemical reactivity of the polymer samples increase many times [34].

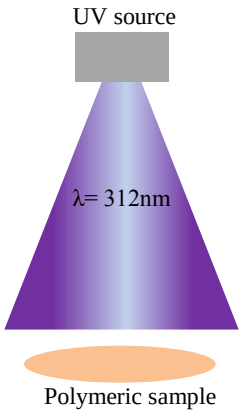

Figure 17: The scheme shows a polymer sample is being irradiated by UV rays having wavelength of 312 nm.

2.3 Chemical etching

The fabrication of nanochannel within a polymer foil was achieved by the use of chemical etching. The foil was exposed to a chemical etchant. Nanochannels of different shapes and sizes can be fabricated using the technique. In this study, cylindrical and conical shaped pores were fabricated within a polymer foil.

2.3.1 Symmetrical etching

Cylindrical nanochannels were fabricated technique inside a PET sample with a fluence of 1.0×10^{8} ions/cm^{2} using the symmetrical etching technique. The experimental set-up for the fabricating of cylindrical nanochannel within a PET foil is shown in Figure 18. Prior to the etching, the polymer sample was fixed inside a sample holder. Sodium hydroxide with a molarity

of 2M was used as the etchant. The etchant was heated up to 50 ^{o}C and then the polymer sample was immersed in the etchant for approximately 1 hour. Later, the sample was removed from the etching solution, washed and stored in distilled water for approximately 24 hours.

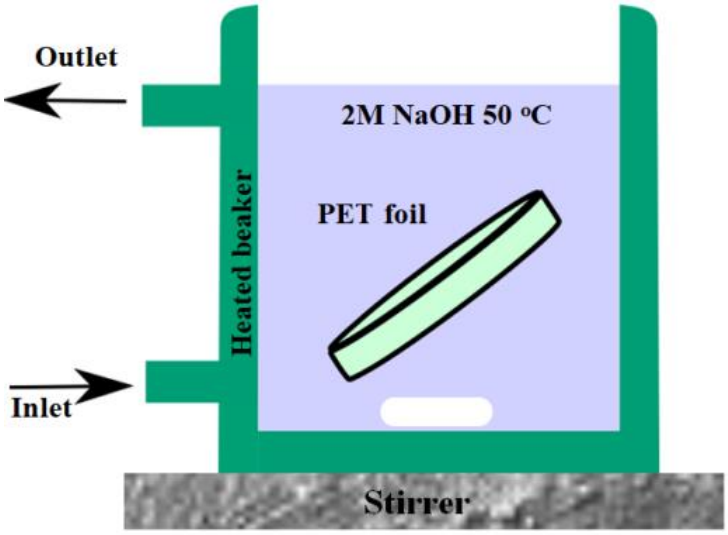

Figure 18: The scheme shows the symmetrical etching set-up of a PET foil.

2.3.2 Soft Etching

The soft etching technique uses a mild type of etchant. The technique falls under the category of symmetrical etching. The method is used to fabricate channels within polyimide (PI) foils with an average opening diameter in the sub-nanometre range, as shown in Figure 19. Dimethyl formamide (DMF) was used as the etchant, the PI foils were submerged inside the etchant for at least 24 hours. The etchant dissolves the polymeric traces present inside the tracks [33]. On the other hand, the bulk material was slightly consumed by the etchant [33]. Later, the PI foil was taken out of the in-organic etchant and cleaned with ethanol and subsequently with water. Sub-nanometer channels are quite difficult to fabricate within a PI foil using the conventional etching technique. The conventional etching technique uses sodium hypochlorite as the etchant. The inorganic etchant is quite aggressive, making it difficult to fabricate sub-nanometer channels. The study utilised PI foils with fluence ranging from 4.0×10^{8} pores/cm^{2} to 4.0×10^{10} pores/cm^{2}.

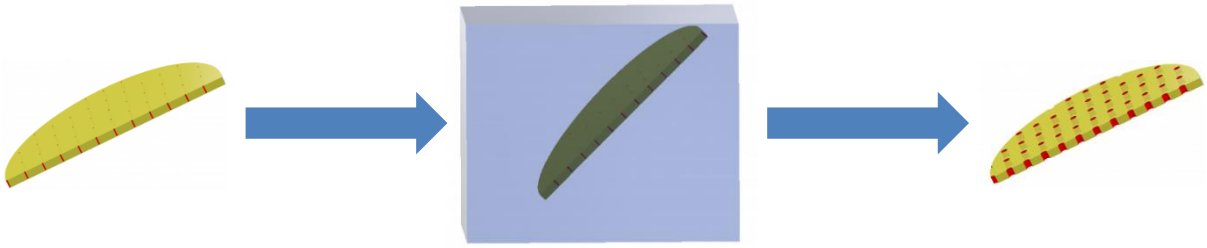

Figure 19: Soft etching of the heavy ion irradiated polyimide membrane.

Following the soft etching of the PI foils, remnants within the channels were removed using the *I-V* process technique. The PI membrane was fixed between the two cells. The volume capacity of the individual cell was approximately 4.5 ml, and the opening diameter was approximately equal to 11 mm. The cells were filled with NaCl solution having a molarity of 100 mM. Homemade Ag/AgCl electrodes were immersed inside the solution, and a triangular voltage signal was applied. The signal has an amplitude of 2V, a period of 30 and a step size of 0.1V. Over time, the current value starts to increase, as depicted in Figure 20, indicating the removal of residues from the channels. Eventually, the current values became stable indicating the complete removal of residues from the pores.

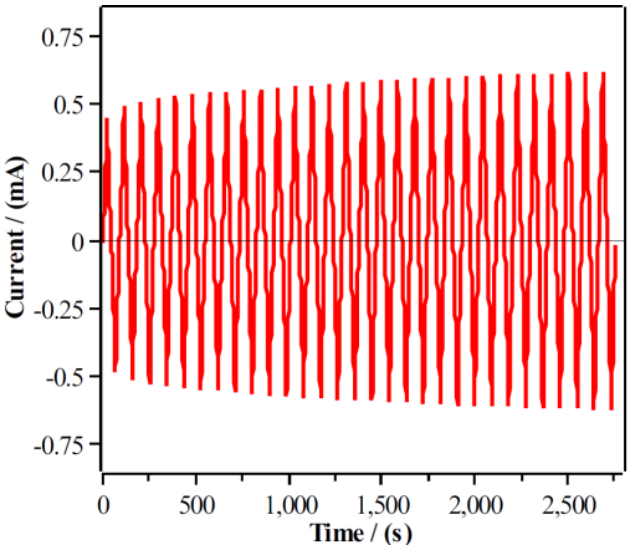

Figure 20: *I-V* process was applied in order to remove the remnants inside the PI membrane after the soft-etching procedure.

2.3.3 Asymmetrical etching

Conical nanopores were fabricated within PET foil through the asymmetrical etching technique. Figure 21a depicts the experimental set-up with two polymer foils with single fluence and multiple fluence of 10^7 ions/cm^2, that were fixed between the cells. One side of the polymer foils was introduced to 9M NaOH whereas the other side was introduced to the stopping solution, i.e., the mixture of 1M Formic acid and 1M KCl solution. The middle cell had two openings, while the side cells had one. Prior to the etching process, the etchant and the stopping solution were heated to 30 ^{o}C. The middle cell and side cells were filled with the etchant and the stopping solution, respectively. Later on, the cells were covered with a Faraday cage as shown in Figure 21b, which provides thermal and electric shielding to the experimental set-up. The experimental set-up was placed over a heating plate and the temperature was set at 30 ^{o}C.

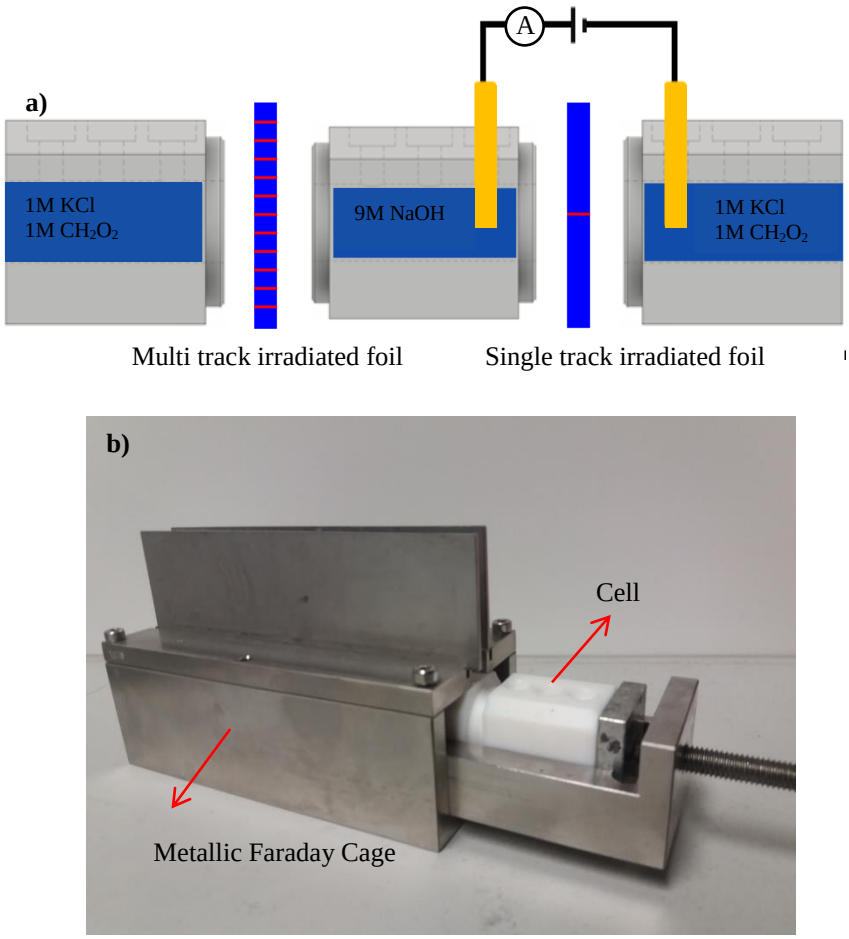

Figure 21: (a) Schematic illustration of asymmetric etching set-up (b) Shows how the etching set-up was placed inside a Faraday cage.

Gold electrodes were immersed inside both solutions and a voltage bias of -1V was applied across the single track PET foil to observe the etching process, shown in Figure 22 (current vs time graph). The current value remained zero for a period of time, indicating that the pore was in a closed state. The opening of the pore is indicated by a large fluctuation in the current value. The etching process was continued until the current was in the range of -2.5 to -3 nA. The etching process was stopped immediately once the desired current range was achieved and the etchant was removed from the middle cell. Later, the PET foil was rinsed with the stopping solution and subsequently with distilled water. The foil was stored in the water for a minimum for a day to completely remove any residual chemicals.

The voltage bias plays a vital role in the etching process. The negative bias was applied to force the hydroxyl ion to electromigrate toward the tip of the cone. Conversely, a positive voltage bias would impede the electromigration of the anion, resulting in inefficient etching [66].

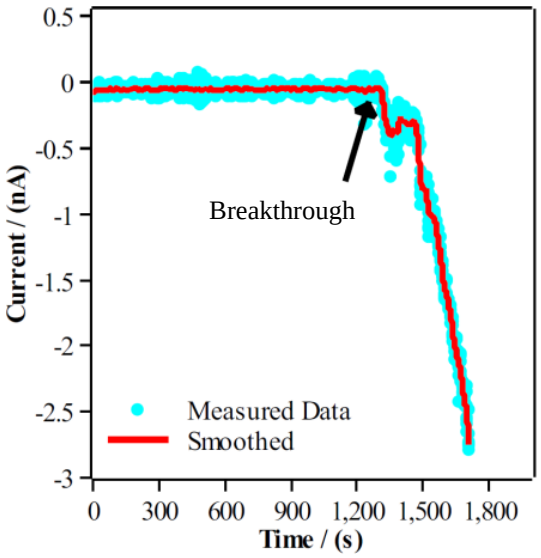

Figure 22: Current vs time graph shows the progress of the asymmetric etching process. The breakthrough point indicates the opening of the pore. The increase in current value indicates the enlargement of the pore size.

2.4 Electrostatic self-assembly of Poly(allylamine Hydrochloride)

The conical nanopore within PET was functionalised with PAH. The negative charge on the surface can be tuned to positive by the functionalisation with PAH. The PET foil was firstly

washed and immersed in a trizma buffer solution. Later, the foil was left in the PAH solution was atleast 24 hours.

2.5 Fabrication of hydrogel-PET composite membrane

The hydrogel solution was prepared by mixing Acrylic acid (AA), N,N methylene bis acrylamide (BIS), Irgacure 2959 (Irga) and water in respective weight percentages. AA served as the monomer while BIS was used as the crosslinking agent, and the percentage weight of BIS, i.e., 3wt% remained constant throughout the study. Irga functioned as the photoinitiator, and its quantity in the solutions was 0.3wt%. Water was used as the solvent; it was also noted that a critical percentage weight of water in the reaction mixture was necessary for hydrogel synthesis.

Figure 23 shows the process for synthesising a hydrogel PET (HP) membrane. Firstly, all of the chemical ingredients were mixed in the desired proportion. The resulting solution was degassed with nitrogen for at least 5-7 minutes to eliminate dissolved oxygen. Next, a PET foil with a fluence of 1.0×10^{8} pores/cm^{2} and an average pore size ranging between 180 and 260nm was placed in a filter holder. Later, the degassed hydrogel solution was passed through the PET foil. Afterward, the PET foil was placed in a ceramic cup, followed by pouring of the entire hydrogel solution into the cup. The hydrogel solution was again degassed for 2-3 minutes and exposed to UV rays (TATTU UV torch) (365 nm) for a maximum of 10 minutes. The distance between the UV torch and the bottom of the ceramic cup was approximately 2.5 cm. After approximately 2 minutes of UV irradiation, the solution's temperature rose up to 65 ^{o}C to 75 ^{o}C due to the exothermic polymerisation reaction. The hydrogel solution was cured completely approximately after 4-6 minutes. The solution in the ceramic container solidified into the hydrogel block, which also included the PET membrane. The PET foil was then carefully removed from the hydrogel block. The channels inside the PET foil incorporated hydrogel rods, and a hydrogel layer also adhered to the surface of the PET foil. The weakly adhered layer was removed by rubbing the membrane against coarse tissue paper, but a thin hydrogel layer remained adhered despite after the rubbing process. Later, the membrane was immersed in water for 24 hours in order to get rid of the unreacted chemicals. The membranes were taken out of water, soaked and weighed. Afterward, the membrane was pressed against a fine tissue and dried in the open air for at least 120 minutes and weighed. Finally, the membrane was immersed in the water for 2-3 hours to prepare it for *I-V* measurements.

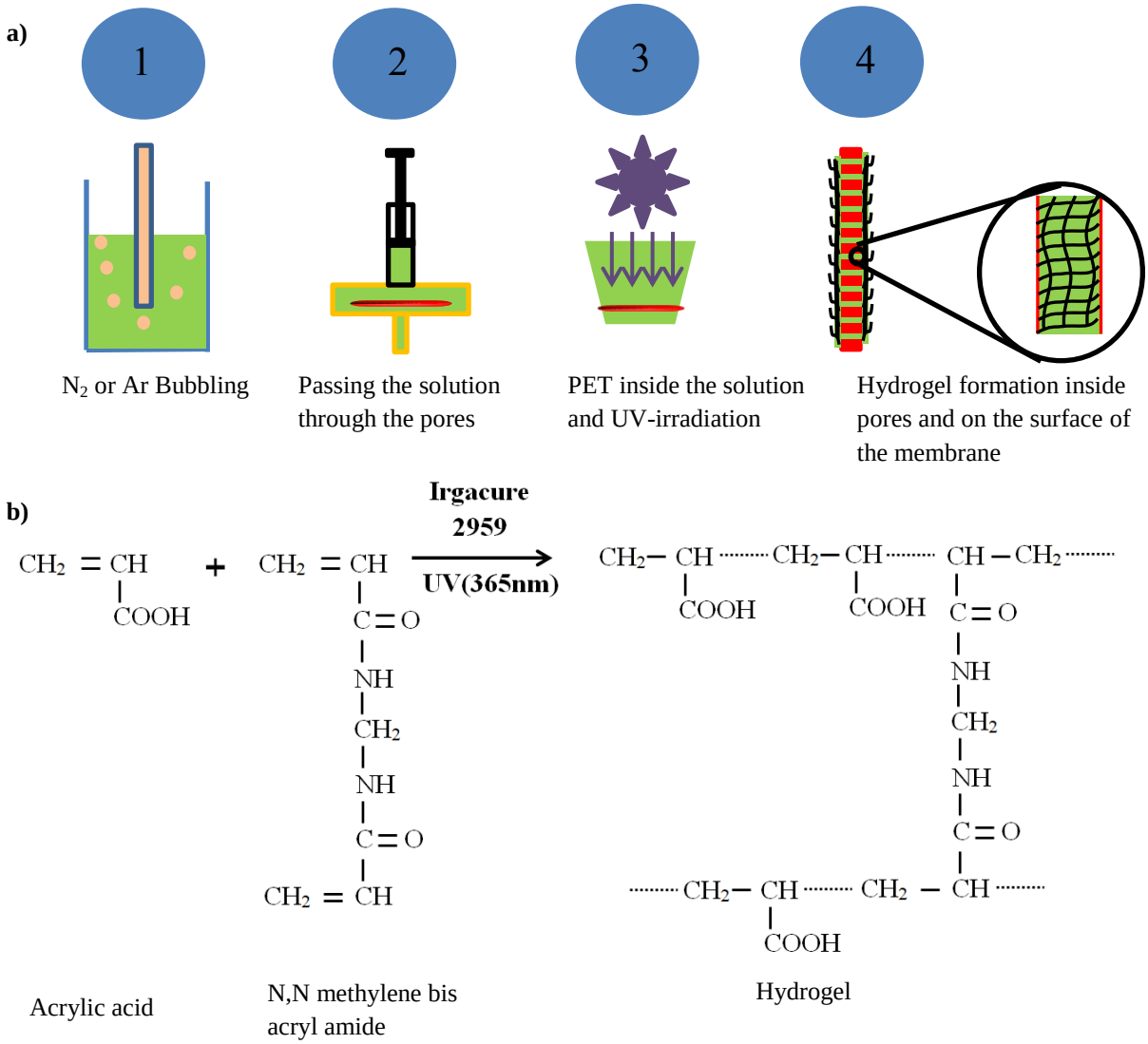

Figure 23: (a) The scheme shows the procedure for the fabrication of the HP membrane (b) Polymerisation reaction of the monomer with the cross-linker, the reaction was activated by irgacure during the UV-irradiation [67].

2.6 *I-V* characterisation of conical nanopores

The *I-V* technique was used to monitor the ion transport behaviour inside negatively charged and positively charged conical nanopores (Figure 24). The PET foil was fixed between two cells containing electrolyte solution. Homemade Ag/AgCl electrodes were immersed inside the cells and a triangular voltage signal was applied using the Keithley picoammeter 6487 and the corresponding current was measured. The signal had an amplitude of 2V, a period of 3 and a step size of 0.1V. The picoammeter was integrated with the computer using the LabVIEW program.

Before carrying out the *I-V* experiment, the experimental set-up was shielded in the Faraday cage. *I-V* experiments were carried out at room temperature and pressure.

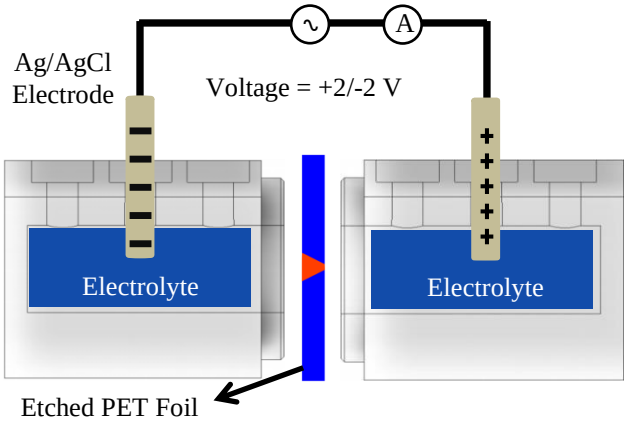

Figure 24: *I-V* experimental set-up for monitoring the ion transport behaviour.

2.7 *I-V* measurement of energy harvesting experiments

The polyimide or the HP membrane was fixed between the cells. The cells were filled with asymmetric electrolyte solutions, as shown in Figure 25. Electrodes used for the study comprised of Ag/AgCl wire that was dipped inside 3M KCl solution. The special electrodes were used instead of homemade Ag/AgCl electrodes to avoid the potential generated due to the redox reaction [61]. All of the experiments were performed at room temperature and pressure.

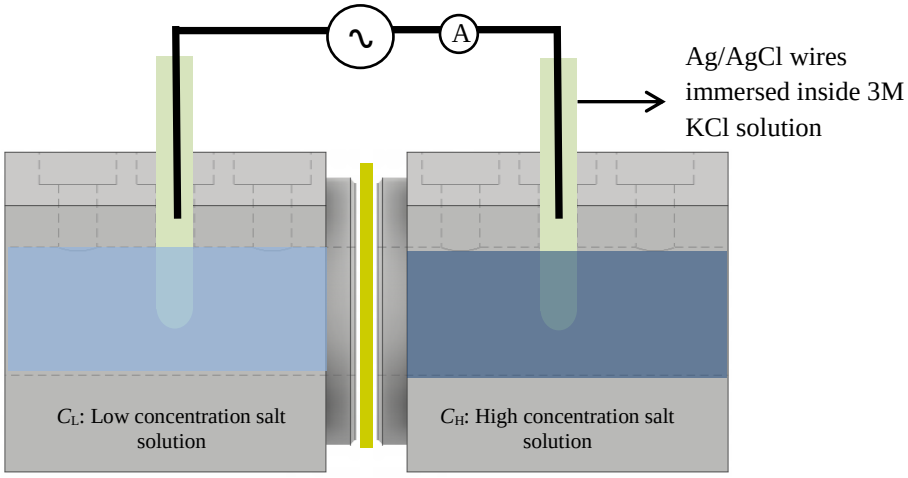

Figure 25: *I-V* set-up for conducting out energy harvesting experiments.

2.8 Scanning electron microscopy

Scanning electron microscopy (SEM) (Philips XL30) was used to determine the base diameter of conical nanopores and to visualise hydrogel rods within cylindrical nanochannels. The polymer membranes used in the current study were non-conductive, thus a thin gold layer was sputtered on the membranes using a sputter coater.

The conical tip (the circular opening at the apex of a conical nanopore) had a diameter less than 50 nm. Due to distortion in the obtained SEM images at high magnification, it was difficult to observe the conical tips under the SEM. The diameter of tips was measured with the help of a two-step process: SEM imaging and *I-V* experimentation.

The diameter of the base of the conical nanopores was in the sub-micron range, making it easily observable under the SEM. The use of the single pore foil for the SEM imaging was not possible due to cutting of the samples during preparation. Moreover, it is difficult to locate a single pore under the SEM. Instead, a multiple fluence foil (10^7 pores/cm^2) was used for viewing under the SEM. The multiple fluence PET foil was etched simultaneously along with the single pore PET foil (please refer to Chapter 2, section 2.3.3). The multiple fluence foil was cut, attached with sticky carbon tab and placed onto a metallic stub. Finally, the bases of the cones were viewed under SEM and their diameters were measured (Figure 26a). The average diameter of the bases was in the range of 500 nm to 820 nm.

The second step was the *I-V* measurement of the single pore foil. The electrolyte used in the experiment was 1M KCl having a pH value of 3. The linear *I-V* curve was obtained (Figure 26b), indicating that the conductivity of the pore was independent of surface charges and solely dependent on the pore size. To calculate the tip size, the slope of the *I-V* curve, the average base diameter and the thickness of the etched PET foil were inserted into equation 9 [34]. The tip diameter was in the range from 27 nm to 33 nm.

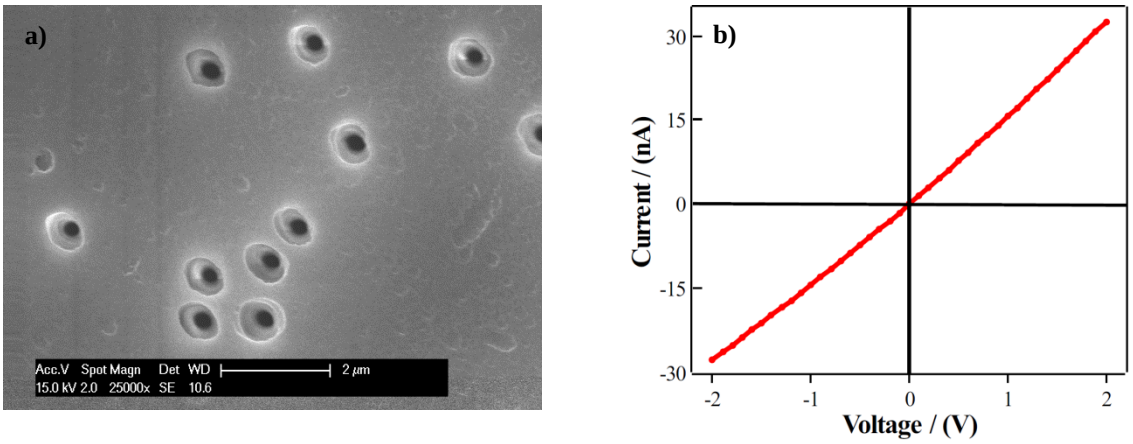

Figure 26: (a) SEM image shows the base of the conical nanopores fabricated within PET membrane having fluence of 10^7 pores/cm^2 (b) *I-V* curve of a single conical nanopore in KCl salt solution having molarity of 1M and pH value of 3.

$$d = \frac{4LI}{\kappa \pi V D} \tag{9}$$

d: diameter of the tip
D: Base diameter
L: Thickness of the PET foil (12 µm)
I: Current
V: Voltage
K: conductance of 1M KCl (11.37 S m^{-1} at 26°C)

The hydrogel rods within the HP membrane and the average diameter of the pore within the PET support were observed under SEM. To determine the diameter of the pores within the PET support material, the sample was cut in the desired dimension and attached to a metallic stub using sticky carbon tab. Later, the sample was coated with gold to view it under SEM. The average pore diameter of PET support was in the range of 180 nm to 260 nm, as shown in Figure 27a.

To view the hydrogel rods inside the HP membrane, the membrane was immersed in liquid nitrogen for approximately 5 minutes before being cut into half while still immersed in the liquid. This was performed to prevent tearing of the membrane. The membrane was adhered using carbon glue with the face of a small 3D-printed cube, as illustrated in Figure 27b. The sample was later sputtered with a thin gold layer and observed under the SEM.

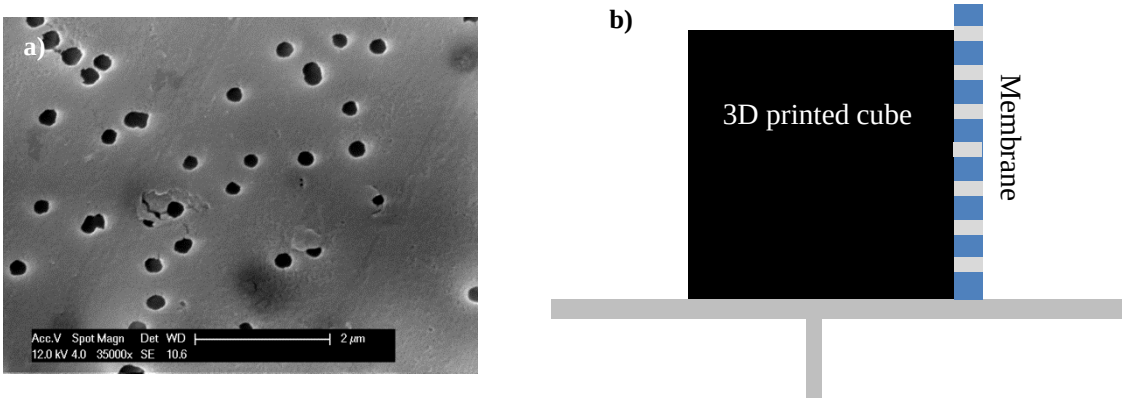

Figure 27: (a) Top view of PET support membrane (b) The cross section of HP membrane that was glued with 3D printed cube with the help of carbon glue. The cross section of the HP membrane was viewed under the SEM.

2.9 FTIR analysis

Fourier transform infrared (FTIR) analysis was performed to detect carboxylic acid groups within the HP membrane. The membrane was fabricated using acrylic acid, therefore the presence of the peaks of carboxylic acid groups in the FTIR analysis would confirm the incorporation of acrylic acid hydrogels within the PET membrane. During the analysis, the scan rate was fixed at 50 scans per measurement, and the wavenumber range was between 650 cm^{-1} to 4000 cm^{-1}.

Chapter 3. Ion Effect on Transport Properties of Conical Nanopore

3.1 Introduction

In recent years, synthetic nanochannels and nanopores have gained significant importance in applications such as energy harvesting, molecular separation and bio-sensing [68-72]. Nanofluidic is defined as the movement of fluid in a channel or structure having dimensions less than 100 nm [73]. Normally, an overlapping double layer in a nanochannel emerges due to the presence of surface charges [74,75]. A charged pore permits the flow of counterions, and provides resistance to the flow of coions [40,76]. The ion transport translates into diode behaviour which is a characteristic of asymmetric channels and can be visualised from the non-linear current-voltage (*I-V)* curves. The asymmetric *I-V* curve is normally absent in micro and macro channels.

In a human body, transportation of ions occurs through protein channels across the cell membrane, e.g, chloride, iodide, sodium ion transportation occurs through chloride channels, sodium/iodide symporter and sodium ion channels, respectively [77-80]. The ion transports across the cell membrane helps in maintaining pH, enzyme activity and osmotic pressure of a cell [80]. Malfunctioning of the transportation in protein channels results in various diseases, e.g., malfunctioning in CLC-5 (a chloride channel) and voltage gated sodium channels may cause Dent's disease and Brugada syndrome [81,82]. Therefore, it is highly important to understand the mechanics of ionic through the channels. The biological ion channels selectively transport ions to an applied stimulus which induces the current [83]. The current normally changes due to the interactions between ions and functional groups on the channel surface [83]. Nevertheless, the functioning of protein ion channels can be mimicked with artificial nanochannels having comparable fluidic characteristics [75]. Biological channels in contrary to solid-state nanochannels demonstrate high ion selectivity [35]. On the other hand, solid-state nanochannels present various advantages over biological ion channels such as robustness, control over pore size and geometry and ease of surface modification [53,84]. To date, various techniques have been introduced to fabricate artificial nanochannels such as focused ion beam, lithography and track etching technique [73,74,76,85].

Some of the sentences, paragraphs, diagrams and the introduction part of this chapter of the thesis were published in following journal article
"**Anions effect on ion transport properties of polyelectrolyte modified single conical nanopores**" || ***M. H.A. Haider***, *M. Ali, W. Ensinger* ||
https://doi.org/10.1016/j.cplett.2021.138349

The track etching technique is a quite versatile and simple method to fabricate nanochannels in polymer membranes (e.g., polycarbonate (PC), polyethylene terephthalate (PET), polyimide (PI) and others) having variable thickness [86]. Following the etching, carboxylic acid groups are formed at the surface of the nanopore, giving a net negative surface charge in the neutral or basic medium due to the deprotonation of the groups [34,84,87].

The surface of the channel can be tuned positive by functionalising surface carboxylic acid moieties with suitable cationic species either electrostatically or covalently [40,76]. Poly(allylamine hydrochloride) (PAH) is one of the cationic polymers that can be attached to the surface via electrostatic self-assembly [88]. Amine groups are fixed to the chain of PAH, which are in a protonated state below the pH value of 9.67 [89]. Protonated amine groups have a tendency to bind with various anions in a specific pH window.

The transport of an anion within a positively charged nanopore is influenced by the diffusion coefficient and the interaction between protonated amine groups [40]. Strong interactions between the anions and amine groups result in charge neutralisation or charge inversion [40]. A nanopore having no net surface charge is non-selective to both cations and anions whereas the negatively charged nanopore favours the transport of cations over anions. The above behaviour can easily be interpreted from the *I-V* curves and rectification factor (*RF*) value, which is calculated using equations 4 and 5 (please refer to Chapter 1, section 1.7) [55].

The primary objective of the study is to investigate the ion transport behaviour within the charged nanopore. An etched PET foil was fixed between two cells, a salt solution was poured inside the cells and two home-made Ag/AgCl electrodes were immersed in the solution. A triangular shaped voltage having an amplitude of 2V was applied and the current was measured. Ions part of the study were Li^+, Na^+, K^+, Ca^{2+}, La^{3+}, NO_3^-, BrO_3^-, HCO_3^-, $H_2PO_4^-$, SO_4^{2-}, HPO_4^{2-}, and $C_6H_5O_7^{3-}$. Additionally, the effect of pH on the transport behaviour of ions was also part of the study. The pH value of all of the salt solutions was set at 7, unless otherwise specified.

3.2 Results and discussion

3.2.1 A comparison between unmodified and PAH-modified conical nanopore

According to the previous literature, the surface charge density of PET nanopores is typically around 1e/nm^2 of PET nanopores [87]. The conical nanopore allows the transport of counterions

from the tip to the base, while hindering the flow of coions resulting in an asymmetric *I-V* curve, as shown in Figure 28. The PAH-modified conical nanopore was obtained after the PAH surface functionalisation of an unmodified conical nanopore.

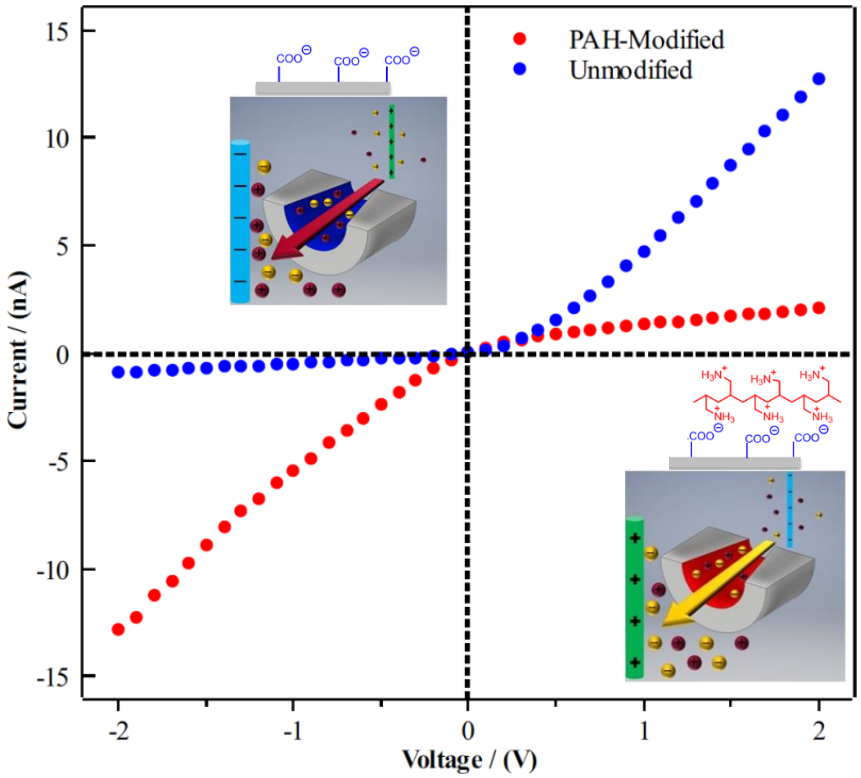

Figure 28: *I-V* curve of the PAH-modified nanopore and the unmodified nanopore. The nanopores were exposed to 100mM KCl salt solution [55].

The negatively charged nanopore (unmodified nanopore) allows the preferential transport of cations, resulting in positive rectification (blue coloured *I-V* curve), as shown in Figure 28. The negatively charged surface of the nanopore can be inverted to positive by chemical functionalisation with PAH. PAH molecule has amine groups that protonated under acidic or neutral conditions. The protonated amine groups bind electrostatically to carboxylate ions present on the surface of the pore. The excess of positively charged chemical moieties inverts the fixed surface charge from negative to positive. The PAH-modified positively charged conical nanopore, transports the anion selectively, resulting in the negative rectification indicated by the red coloured asymmetric *I-V* curve, as shown in Figure 28. The PAH-modified nanopore consistently showed a stable reading, indicating that the adsorption of PAH on the surface was quite strong.

3.2.2 Impact of electrolyte concentration on the rectification behaviour

Positive rectification behaviour was exhibited by the unmodified negatively charged conical pore when introduced to 100 mM KCl solution (Figure 29). A linear, black coloured straight *I-V* curve with a rectification factor of 1.20 was obtained with 1000 mM or 1M KCl. The rectification factor obtained at a concentration of 100 mM KCl was 4.76.

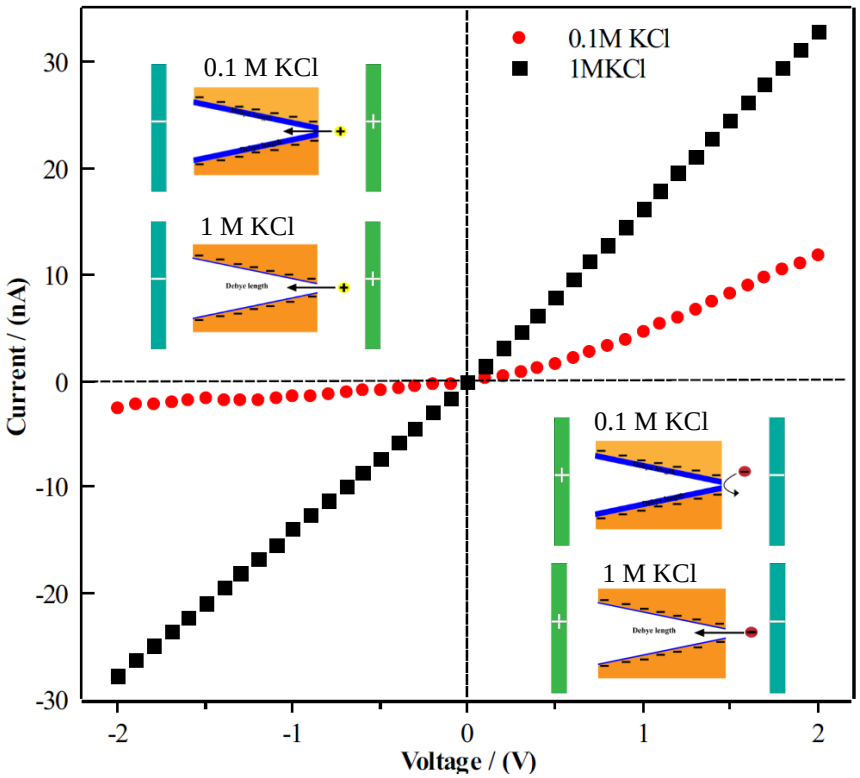

Figure 29: The unmodified conical nanopore was exposed to 0.1M KCl and 1M KCl solution. A diodic behaviour is observed with 0.1M KCl whereas a straight line is observed with 1M KCl.

The low value of the rectification factor obtained with the concentrated salt solution indicates a decrease in the Debye length to pore size ratio (For a detailed explanation, refer to Chapter 1, section 1.6).

3.2.3 Ion current Rectification behaviour in various pH mediums

The study investigated the effect of pH on the cation transport behaviour within an unmodified conical nanopore (negatively charged). Four different 100 mM KCl salt solutions with different pH values (pH values: 1.5, 3, 7 and 9.5) were prepared. pH values of 7 and 9.5 exhibited a positive rectification whereas a negative rectification was observed in the case of pH 1.5. At pH

3, a linear straight line was observed, indicating the absence of rectification. Linear and negative rectification behaviour were obtained at pH values of 3 and 1.5, respectively (Figure 30a). The *I-V* curve for pH 3 displays a current value of 5.09 nA at +2V and -5.73 at -2V. Figure 30b shows that the *I-V* curve obtained at pH 1.5 had larger current values at negative voltages compared to the *I-V* curve obtained at pH 3. Both of the pH values, i.e., 1.5 and 3 exhibited approximately identical current values at positive voltages.

Figure 30c displays the normalised rectification factor (NRF or RF/RF_o) at different pH values. Positive NRF values were obtained at the pH values of 9.5 and 7, while negative NRF values were obtained at pH values of 3 and 1.5 (-0.13 and -0.26 respectively). NRF value of a positive and negative rectified *I-V* curve is positive and negative, respectively, therefore a charge inversion line was drawn at NRF value of 0 (Figure 30c) for better understanding of the results.

The surface of the unmodified pore carries a net negative charge in the neutral and basic media due to the presence of carboxylate ions. At the pH values of 7 and 9.5, the NRF and current values were approximately similar, indicating that an approximately equal number of carboxylate ions were present at both of the pH values. At pH 3.0, the unmodified nanopore exhibited a linear *I-V* curve and a NRF value close to zero, indicating that no preferential transport of cation was taking place. The non-preferential behaviour towards cations and anions was due to the surface charge neutralisation. It can be concluded that carboxylate ions (COO^-) present within the unmodified nanopore had become protonated (COOH) at the pH value of 3. The observation of negative rectification behaviour at pH 1.5 suggests that the pore preferentially transports anions. The reason for the negative rectification behaviour is attributed to surface charge inversion from negative to positive, which could be caused by the double protonation of carboxylate ions.

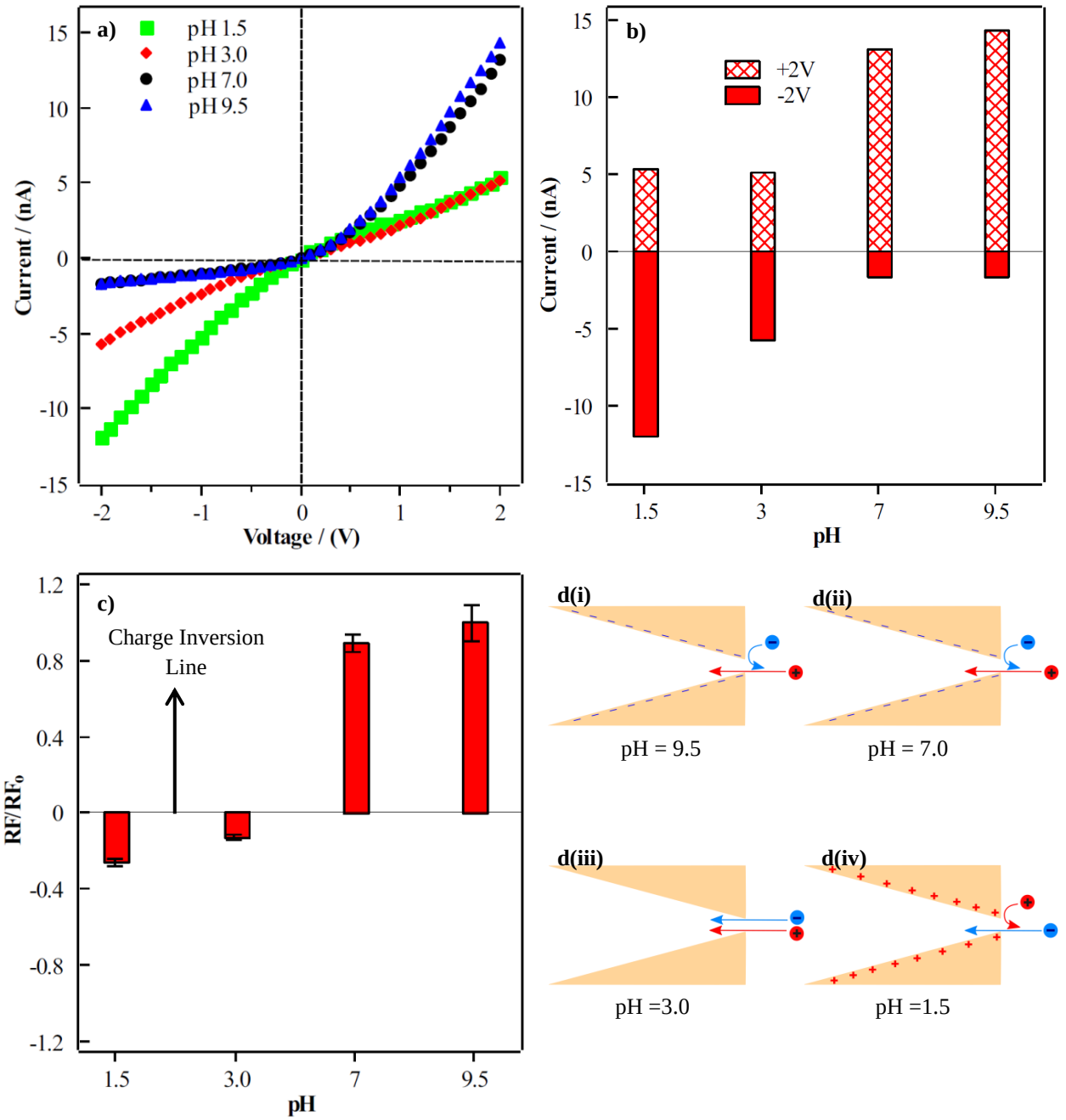

Figure 30: (a) The unmodified nanopore was exposed to different pH media having a molarity of 100mM KCl (b) Current values obtained at +2V and -2V in different pH media (c) Normalised rectification factor obtained at different pH media. The schematic illustration of ion transport inside the unmodified nanopore at pH value of d(i) 9.5 d(ii)7 d(iii)3 d(iv) 1.5.

3.2.4 Transport behaviour of cations and anions inside unmodified conical nanopore

Figure 31a compares the *I-V* curves obtained with different monovalent salt solutions. The molarity of all of the electrolyte solutions was adjusted to 100 mM.

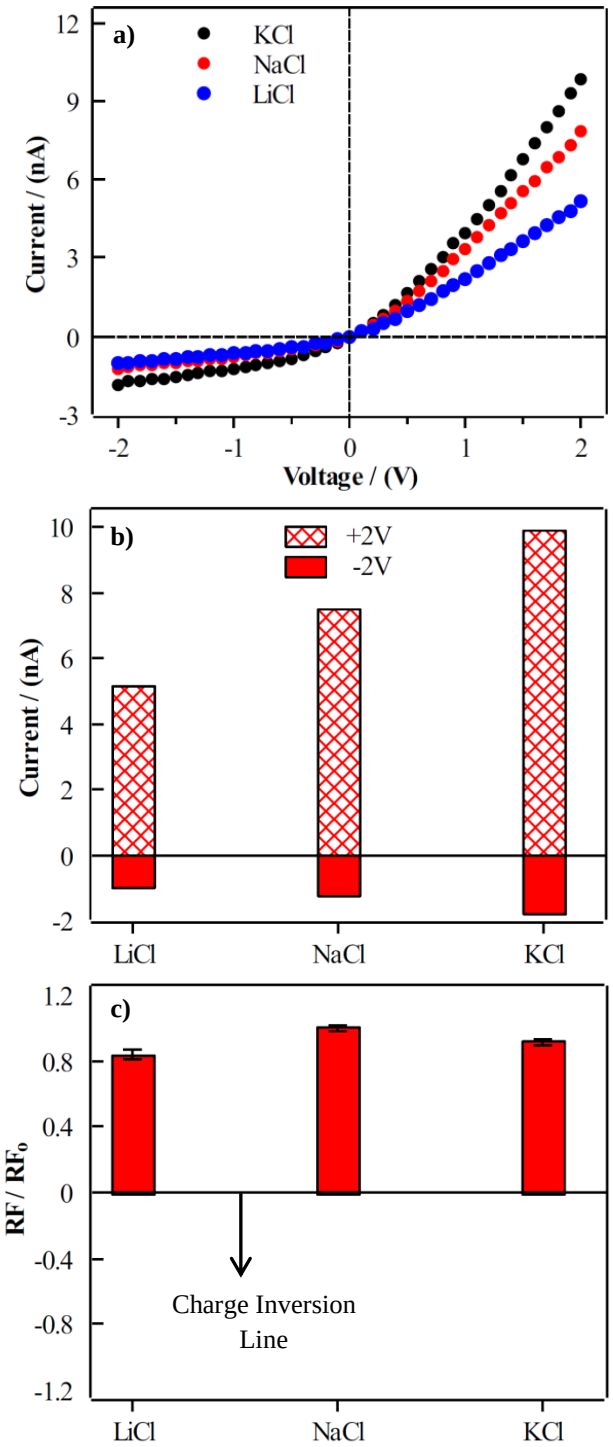

Figure 31: Investigation of transportation behaviour of monovalent cation inside the unmodified nanopore. The concentration of the salt solutions was maintained at 100mM (a) *I-V* curve of LiCl, KCl and NaCl (b) Current values obtained at +2V and -2V with different monovalent salt solutions (c) Normalised rectification factor obtained with LiCl, KCl and NaCl.

The *I-V* curves for all of the monovalent cations under study exhibited positive rectification behaviour. The highest NRF value was exhibited by Na^+ (+1), followed by K^+ (+0.91) and Li^+ (+0.84) (Figure 31c). The maximum current at +2V was recorded for K^+ (+9.86 nA), followed by Na^+ (+7.87 nA) and Li^+ (+5.14 nA), as shown in Figure 31b.

The monovalent cations can be arranged according to the current values obtained at +2V in the following order: $K^+ > Na^+ > Li^+$. Table S1 shows the trend of the electrical conductivity for the cations in the order: $K^+ > Na^+ > Li^+$ [90]. The trend derived from the table and Figure 31b are similar, indicating that the difference in the current values exhibited by the monovalent cations was due to the individual ion electrical conductivity.

The trend in Figure 31b can also be attributed to the electrostatic interactions between monovalent cations and carboxylate ions. The strength of the interactions depends on the valency and charge density of the cations. All of the monovalent cations (K^+, Na^+, Li^+) have similar valency but different ionic sizes. Li^+ has the highest charge density among the investigated monovalent cations whereas K^+ has the lowest. Therefore it is quite possible that Li^+ can interact relatively better with the carboxylate ions compared to the K^+ and Na^+, resulting in a decrease of the overall net surface charge, which subsequently results in the decline of the current values at the positive voltages Figure 31b.

The transport behaviour of multivalent cations was investigated within an unmodified PET conical nanopore. The concentration and pH value of all of the electrolytes included in the investigation were adjusted at 100 mM and 7, respectively. The data of K^+ ions used in previous Figure 31 was reused in Figure 32a for comparison. Figure 32b shows that the current values exhibited by KCl at +2V and -2V were 9.86nA and -1.83 nA, respectively. The current value obtained at +2V and -2V were 5.73 nA and -3.6 nA respectively when the nanopore was exposed to 100 mM $CaCl_2$ solution. The current values obtained with $LaCl_3$ were lower at +2V and higher at -2V compared to the current values obtained with $CaCl_2$. La^{3+} exhibited a negative NRF value of -1 whereas Ca^{2+} exhibited the NRF value of +0.25, as shown in Figure 32c. A positive rectification was observed in the case of K^+ which suggested that the nanopore was selectively transporting the cation and was unable to neutralise or switch the surface charges of the pore. Conversely, Ca^{2+} exhibited an almost linear *I-V* curve and a low NRF value, indicating that the pore was non-selective due to surface charge neutralisation.

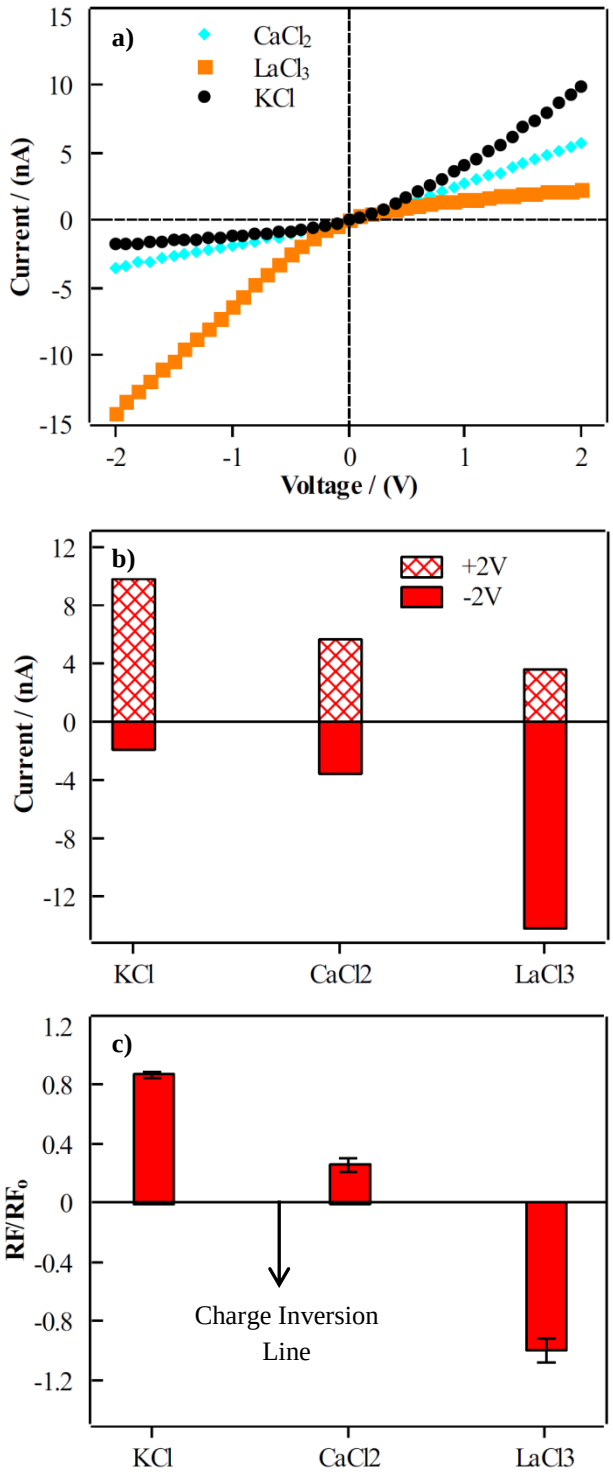

Figure 32: Investigation of transportation behaviour of the multivalent cations inside the unmodified nanopore. The concentration of the salt solutions was maintained at 100mM (a) *I-V* curve of KCl, $CaCl_2$ and $LaCl_3$ (b) Current values obtained at +2V and -2V with different salt solution (c) Normalised rectification factor obtained with KCl, $CaCl_2$ and $LaCl_3$.

The interaction between Ca^{2+} and carboxylate ions was strong enough leading to net zero surface charge. The *I-V* curve and NRF values of La^{3+} demonstrate that the nanopore exclusively transported anions indicating charge inversion to positive. Therefore, it can be said that exposing the unmodified PET membrane to the multivalent cations can lead to the either charge inversion or neutralisation.

Figure 33 shows the schematic of the potential mechanism of the cation transport within the unmodified nanopore. The interaction between the carboxylate ions and the cations depends on the valency and charge density. Cations having high valency and charge density establish stronger interactions with the carboxylate ions. La^{3+} has greater valency compared to K^{+} or Ca^{2+}, therefore La^{3+} was able to switch the surface charges successfully whereas the divalent cation and the monovalent cations failed to invert the surface charges.

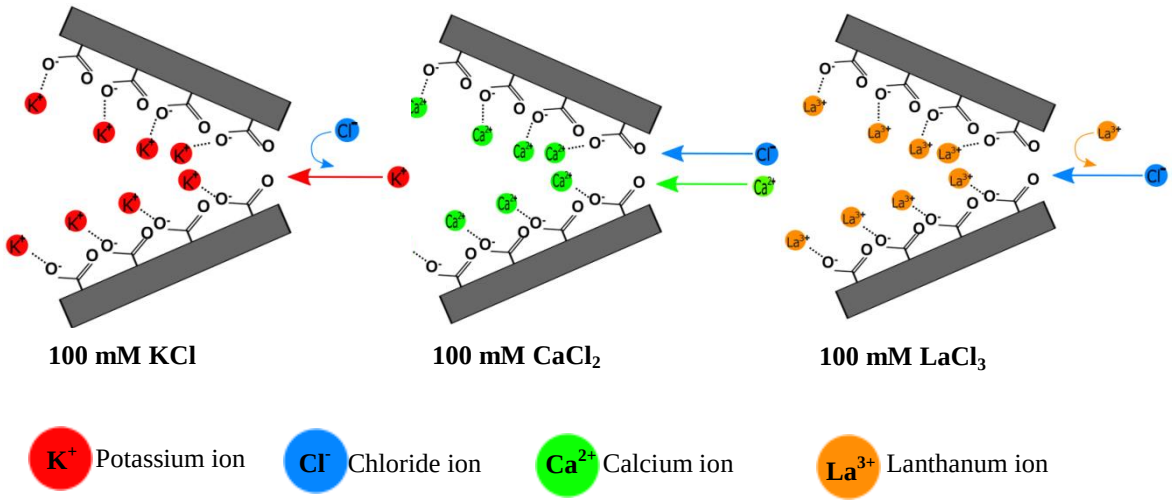

Figure 33: Schematic representation of ion transport behaviour inside the unmodified nanopore when exposed to 100 mM KCl, 100mM $CaCl_2$ and 100mM $LaCl_3$ salt solutions.

The transport behaviour of different anions within an unmodified nanopore was investigated. Figure 34 shows *I-V* curves of the anions under investigation, *I-V* curves with positive rectification behaviour were exhibited by the anions. The salts under investigation were NaCl, $NaNO_3$, $NaBrO_3$, $NaHCO_3$, NaH_2PO_4 and Na_2SO_4. The molar concentration and pH of each salt solution were 100 mM and 7, respectively. All of the anions exhibited different current values at the positive voltages, which can be attributed to individual salt conductivity.

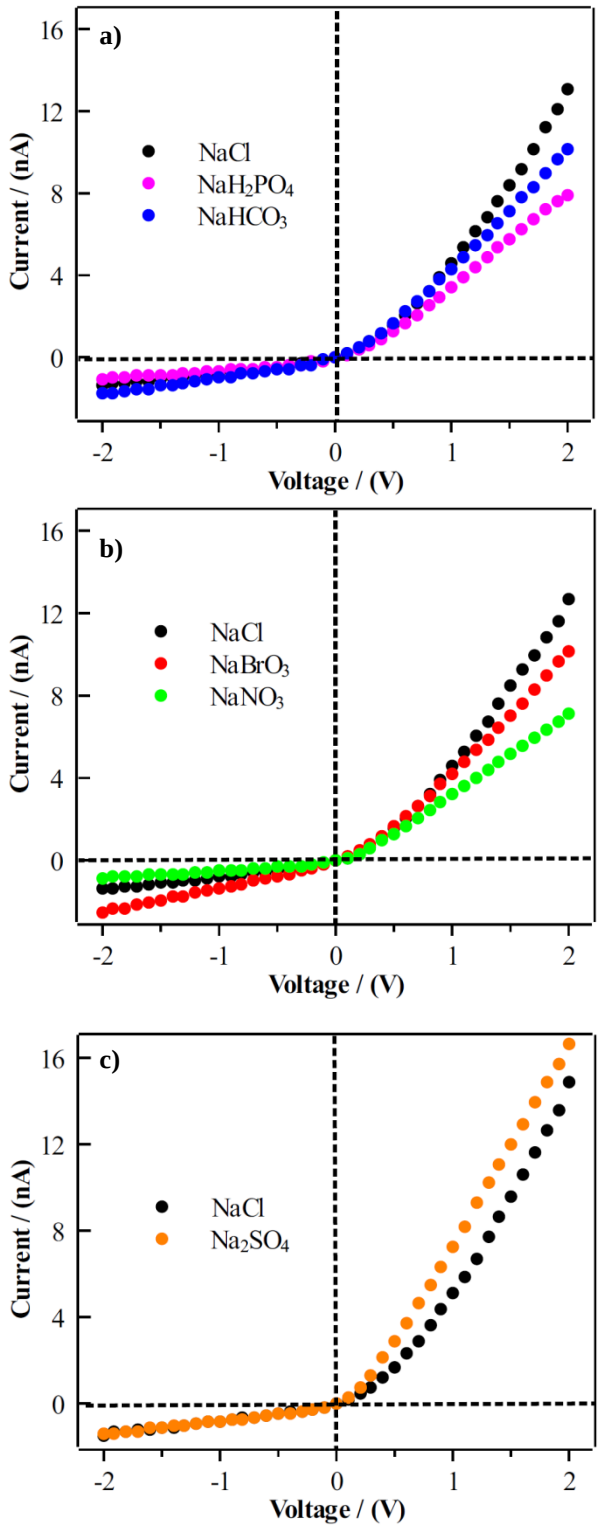

Figure 34: Investigation of transportation behaviour of the anions inside an unmodified nanopore. The concentration of the salt solutions was maintained at 100mM (a) *I-V* curves of 100 mM NaCl, 100 mM NaH_2PO_4 and 100 mM $NaHCO_3$ (b) *I-V* curves of 100 mM NaCl, 100 mM $NaBrO_3$ and 100 mM $NaNO_3$ (c) *I-V* curves of 100 mM NaCl and 100 mM Na_2SO_4.

3.2.5 Transport behaviour of anions inside PAH-modified nanopore

The transport behaviour of various anions was investigated within the PAH-modified conical nanopore. The salts under investigation were NaCl, $NaNO_3$, $NaBrO_3$, $NaHCO_3$, NaH_2PO_4, Na_2HPO_4, Na_2SO_4, K_2CrO_4 and $Na_3C_6H_5O_7$. Electrolyte solutions were prepared by mixing a portion of 100 mM NaCl or 100 mM KCl solution and respective 100 mM NaX or 100 mM KX solution, where the X term refers to the anions under investigation. The total concentration of anions present in the electrolyte solution remained at 100 mM. Prior to the *I-V* experiments, the pH values of all of the electrolyte solutions were adjusted to 7. Figure 35 shows the *I-V* curves of $NaNO_3$ and $NaBrO_3$. All of the *I-V* curves obtained with different concentrations of NO_3^- and BrO_3^- were negatively rectified, as shown in Figure 35a and b. Increasing the concentration of anions led to a decrease in the current values at negative voltages (Figure 35a and b). A positive rectification or linear *I-V* curve was not obtained with 100 mM NO_3^- or 100 mM BrO_3^- solutions.

Figure 35c shows the normalised current (NC or I/I_o) values obtained at different concentrations of NO_3^- and BrO_3^- at +2V and -2V. The NC values are useful to make a comparison between the anions under investigation. A slight decline in NC values was observed at -2V as the concentration of anions increased, whereas insignificant changes were observed at +2V.

Figure 35d shows the NRF values obtained at the different concentrations of NO_3^- and BrO_3^-. Increasing the concentration of NO_3^- caused a decrease in the NRF values, indicated in Figure 35d. However, increasing the concentration of BrO_3^- had an insignificant effect on the NRF values. It can be observed in Figure 35 that an increment in the concentration of the anions (NO_3^- and BrO_3^-) did not significantly change the NC or NRF values. The increase in the concentration of the anions did not result in positive rectification. The negative rectification and NRF values indicate that the pore was selectively transporting anions due to the net positive charge on the surface. The anions (NO_3^- and BrO_3^-) did not form strong electrostatic interactions with the protonated amine groups necessary to invert or neutralise the surface charges. A small change in current values particularly at negative voltages was observed with the increase in concentration of the anions.

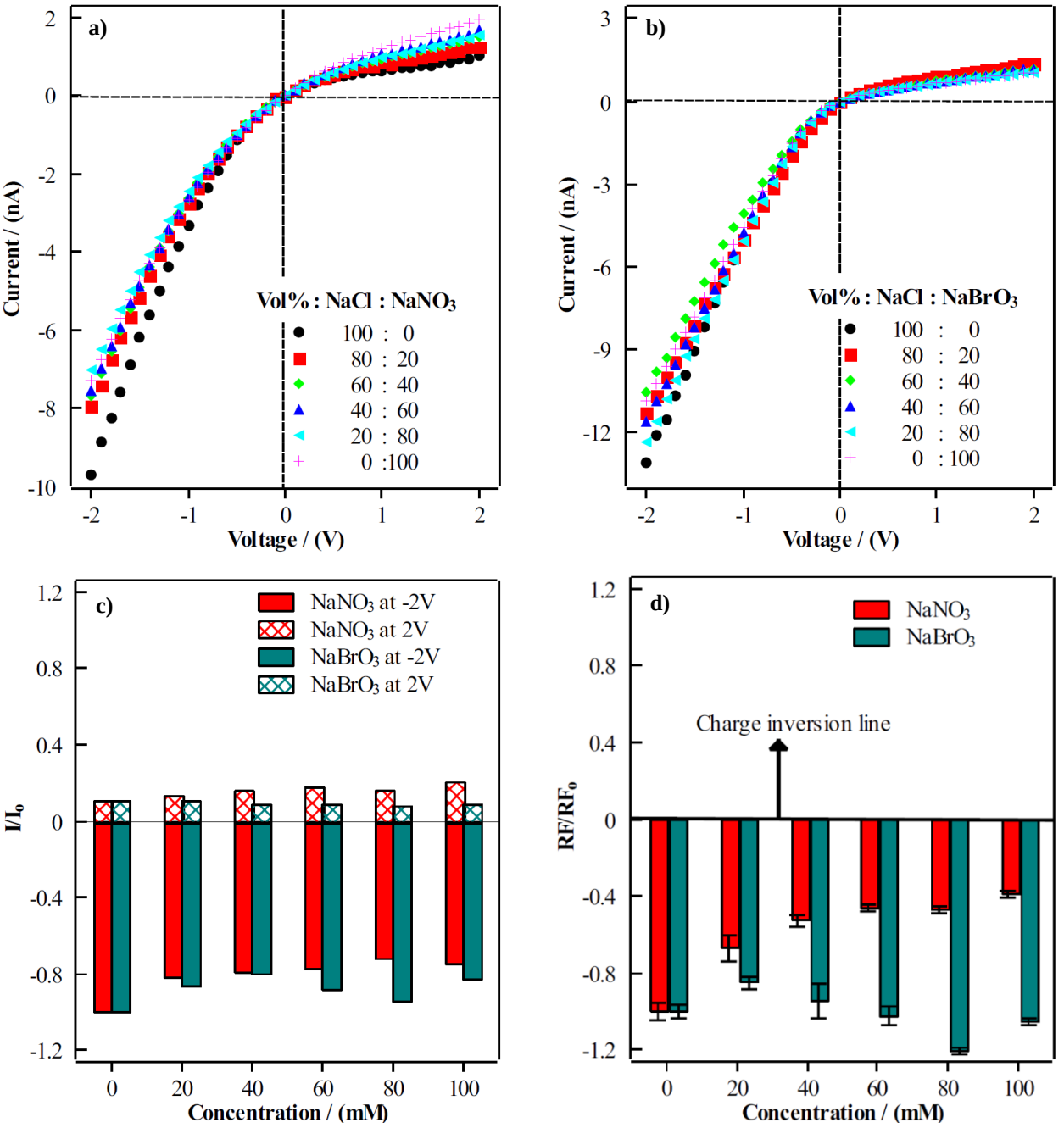

Figure 35: Investigation of transportation behaviour of the various anions inside the PAH-modified nanopore. The total concentration of anions in each salt solution was maintained at 100mM. *I-V* curves were obtained for different concentrations of (a) $NaNO_3$ (b) $NaBrO_3$ (c) Normalised current values were obtained for different concentrations of $NaNO_3$ and $NaBrO_3$ (d) Normalised rectification factors were obtained for different concentrations of $NaNO_3$ and $NaBrO_3$.

In the next set of monovalent category, the transport behaviour of HCO_3^- and $H_2PO_4^-$ within the PAH-modified nanopore was investigated. According to Figure 36a, the electrolyte with a molarity of 100 mM NaCl showed a current value of -8.5 nA at -2V. A low concentration of HCO_3^- (20 mM) resulted in a decrease of the current value to -2.0 nA at -2V. Figure 36a and b

show the transition of the *I-V* curves from negative rectification to slightly positive rectification as the concentration of the anions (HCO_3^- and $H_2PO_4^-$) in the electrolyte solutions increased. The *I-V* curves transitioned at a lower concentration for $H_2PO_4^-$ compared to HCO_3^-.

Figure 36c shows the NC for the cases of HCO_3^- and $H_2PO_4^-$. Raising the concentration of the anions in the electrolyte solution led to an insignificant surge of NC values at +2V. However, a gradual decrease in NC values was also observed at -2V. The NC values were similar at +2V and -2V for a concentration of 60 mM of HCO_3^-. Likewise, the electrolyte solution having a concentration of 40 mM of $H_2PO_4^-$ exhibited approximately similar values of NC at +2V and -2V.

Figure 36d shows that the NRF value increased with the increasing anion concentration. For $H_2PO_4^-$, the NRF value transitioned from negative to positive at a concentration of 40 mM, while for HCO_3^-, the transition occurred at 60 mM. The NRF value obtained with a 100 mM $H_2PO_4^-$ solution was larger than that obtained with a 100 mM HCO_3^- solution.

The anions (HCO_3^- and $H_2PO_4^-$) were able to slightly invert the *I-V* curves towards the positive rectification. However, the current values at positive voltages exhibited by 100 mM HCO_3^- and 100 mM $H_2PO_4^-$ solutions were low. Therefore, it can be concluded that HCO_3^- and $H_2PO_4^-$ slightly switched the surface charges at a concentration value of 100 mM. The anions (HCO_3^- and $H_2PO_4^-$) under investigation were monovalent therefore the electrostatic interaction between protonated amine groups and the anions were not strong enough to completely invert the surface charges. $H_2PO_4^-$ demonstrated higher NRF values and a higher current at +2V compared to HCO_3^- (Figure 36d). The findings indicate that $H_2PO_4^-$ forms a stronger electrostatic interaction with protonated amine groups compared to HCO_3^-. Stronger interaction may occur due to the partial dissociation of $H_2PO_4^-$ ions to the divalent form HPO_4^{2-}, leading to stronger interactions with the protonated amine groups [88].

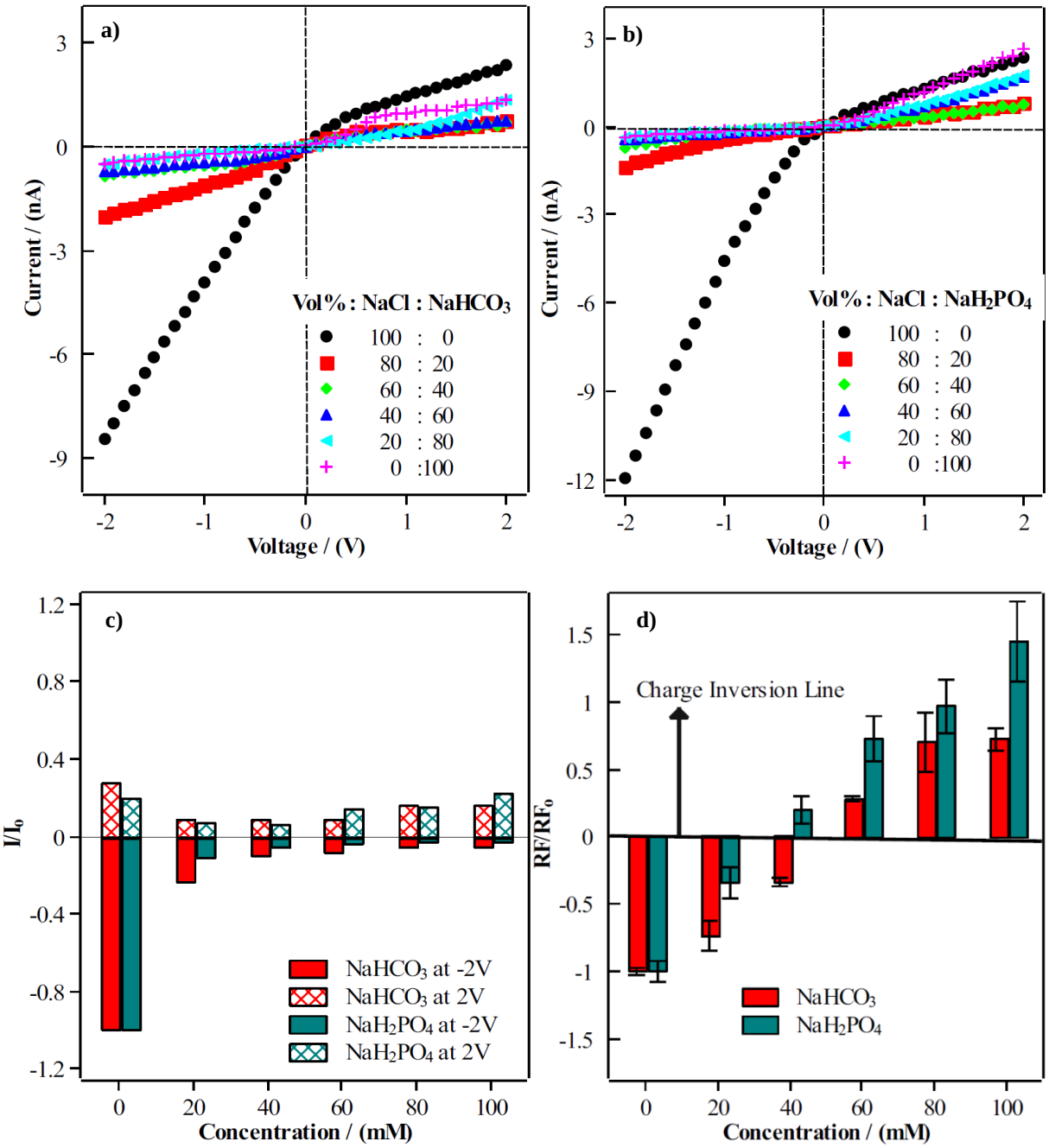

Figure 36: Investigation of transportation behaviour of $NaHCO_3$ and NaH_2PO_4 within the PAH-modified nanopore. The total concentration of anions in each salt solution was maintained at 100mM. *I-V* curves were obtained for different concentration of (a) $NaHCO_3$ (b) NaH_2PO_4 (c) Normalised current values were obtained for different concentration of $NaHCO_3$ and NaH_2PO_4 (d) Normalised rectification factors were obtained for different concentration of $NaHCO_3$ and NaH_2PO_4.

Qualitative analysis for the electrostatic interactions can be done using NRF values. The NRF values can also indicate the strength of electrostatic interactions present between protonated

amine groups and the investigated anions. The anions exhibiting larger positive NRF had stronger interaction with protonated amines groups, therefore based on NRF values, the monovalent anions can be arranged in the following order: $H_2PO_4^-$> HCO_3^- > NO_3^- > BrO_3^- ∽ Cl^-. The Hofmeister series is in the order of $H_2PO_4^-$> HCO_3^- > BrO_3^- ∽ Cl^-> NO_3^- [91,92]. The NRF based trend almost fits the Hofmeister series except for NO_3^- anion. The reason can be attributed to the fluctuations in the current values at both +2V and -2V which might have resulted in an error in the NRF value.

The study investigated the ion transport behaviour of divalent anions (SO_4^{2-}, HPO_4^{2-} and CrO_4^{2-}) within the PAH-modified nanopore. The transport behaviour of SO_4^{2-} within the nanopore was analysed first. The results showed that the increase in the anion (SO_4^{2-}) concentration led to a decrease in current values at the negative voltages, while an increase in current values was noted at the positive voltages, as shown in Figure 37a. The *I-V* curves demonstrated negative rectification at all SO_4^{2-} concentrations.

The *I-V* curve obtained with the electrolyte solution with a concentration of 20mM HPO_4^{2-} exhibited a positive rectification, as shown in Figure 37b. Increasing the concentration of the anion led to an increase in current at the positive voltages. Figure 37c shows the *I-V* curves obtained at various concentrations of K_2CrO_4. A sharp decrease in the current value at negative voltage was observed with the electrolyte solution having a concentration of 20 mM K_2CrO_4. Figure 38a shows an insignificant change in the NC values at +2V and -2V with additional increase in the concentration of K_2CrO_4. However, increasing the concentration of HPO_4^{2-} led to a significant change in the NC values at both +2V and -2V.

Increasing the concentration of HPO_4^{2-} led of surge in NRF values (Figure 38b). NRF values of +0.44 and +1.7 were obtained with concentrations of 20 mM and 100 mM HPO_4^{2-} electrolyte solution, respectively. A dip in the NRF values in Figure 38b was observed at the concentration values of 60 mM and 80 mM in the case of HPO_4^{2}. Ideally, the NRF values should increase at the aforementioned concentration values of HPO_4^{2-}. It can be due to a small fluctuation in the current values at +2V and -2V resulting in a considerable change in the NRF values. Overall, the *I-V* curve with positive rectification was obtained with an electrolyte solution with a concentration of 100 mM HPO_4^{2-}. For CrO_4^{2-}, the NRF values approaches 0 (approximately) at the concentration values ranging from 60 mM to 100 mM.

In the category of monovalent anions, $H_2PO_4^-$ and HCO_3^- were able to neutralise or slightly invert the surface charge, while NO_3^- and BrO_3^- were unsuccessful. For SO_4^{2-}, *I-V* curves with negative rectification behaviour and negative NRF values were observed at every concentration value. It can be inferred that despite SO_4^{2-} being a divalent cation, it failed to neutralise the surface charges. Therefore it can be deduced that the interactions between SO_4^{2-} and the protonated amines groups were not strong enough. This may be due to the high affinity of SO_4^{2-} with water molecules, leading to excessive hydration, consequently resulting in a weaker interaction with the protonated amines groups [93]. Positive NRF values were obtained with HPO_4^{2-}, indicating a strong interaction between HPO_4^{2-} and protonated amine groups, resulting in a significant inversion of surface charges, i.e., positive to negative. HPO_4^{2-} was the only divalent anion able to induce significant inversion of surface charges, i.e, from positive to negative. *I-V* curves with negative rectification were observed in the case of CrO_4^{2-}. However, 100 mM CrO_4^{2-} demonstrated approximately similar current values at +2V and-2V and a NRF value close to 0. Therefore, it can be inferred that CrO_4^{2-} was able to neutralise the surface charges.

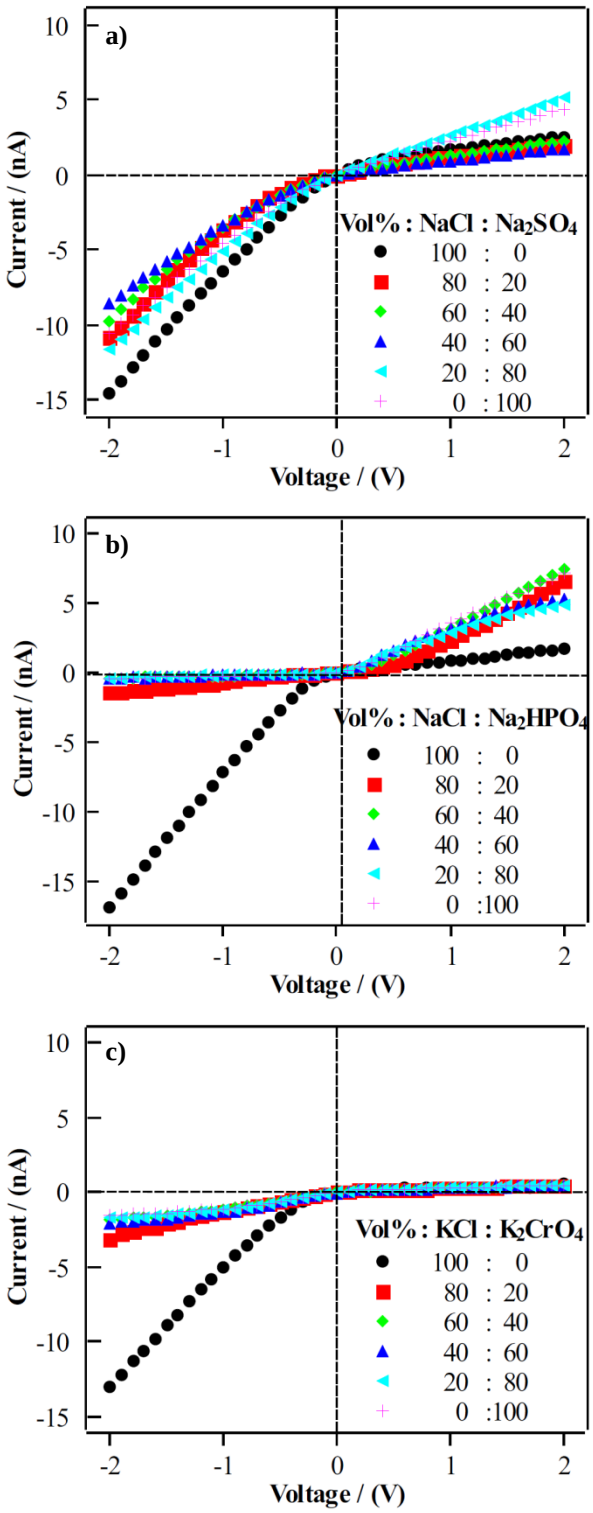

Figure 37: Investigation of transportation behaviour of Na_2SO_4, Na_2HPO_4 and K_2CrO_4 inside the PAH-modified nanopore. The total concentration of anions in each salt solution was maintained at 100mM. *I-V* curves were obtained for different concentration of (a) Na_2HPO_4 (b) Na_2SO_4 (c) K_2CrO_4.

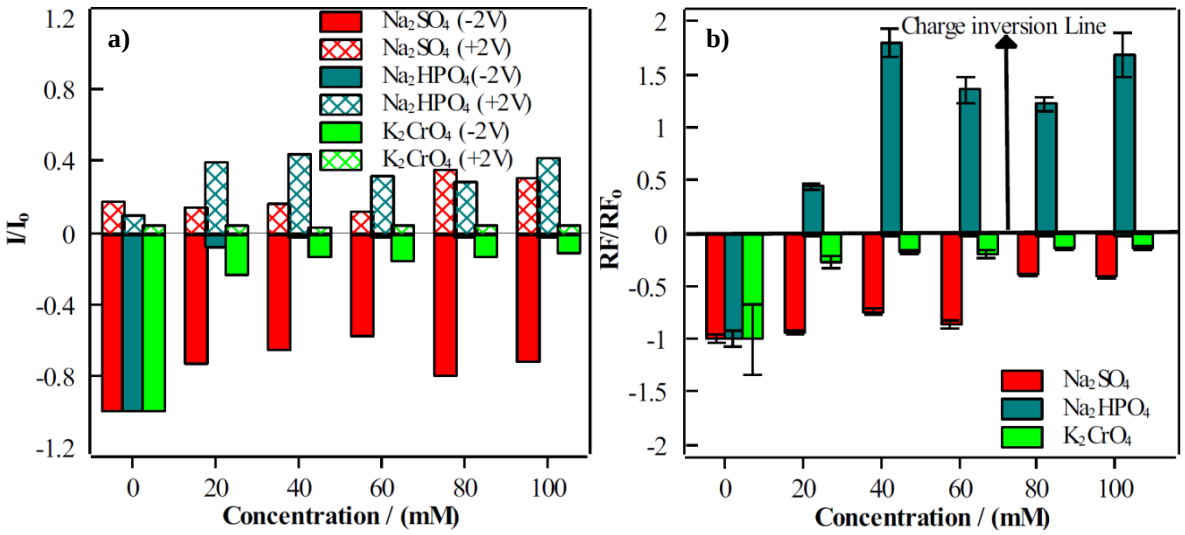

Figure 38: Normalised current values (a) Normalised rectification factors (b) of Na_2SO_4, Na_2HPO_4 and K_2CrO_4.

The study investigated the transport behaviour of citrate within the PAH-modified nanopore. Citrate ($C_6H_5O_7^{3-}$) was the only trivalent anion under investigation. At a concentration of 20 mM, the current values of 0.63 nA and -1.01 nA were obtained at +2V and -2V, respectively (Figure 39a). Similarly, at the concentration of 100 mM, the current values of 2.52 nA and -0.75 nA were obtained at +2V and -2V, respectively. The NRF values at concentrations of 20 mM and 100 mM were -0.20 and +0.42, respectively (Figure 39c).

At a concentration of 20 mM $C_6H_5O_7^{3-}$, an almost linear *I-V* curve was obtained at a concentration of 20 mM, indicating the ohmic behaviour. At a concentration of 100 mM, a slightly positive rectified *I-V* curve was obtained, with low current values at the positive voltages. This suggests that the anion was able to slightly invert surface charges from negative to positive. Despite $C_6H_5O_7^{3-}$ being a trivalent anion, it exhibited a lower NRF value compared to HPO_4^{2-}. This indicates that the electrostatic interactions between HPO_4^{2-} and protonated amine are stronger than those between $C_6H_5O_7^{3-}$ and protonated amine. $C_6H_5O_7^{3-}$ has higher valency, but due to the large size, it has low charge density. This may explain the reason for weaker electrostatic interactions with the protonated amine groups compared to the interaction between HPO_4^{2-} and protonated amine.

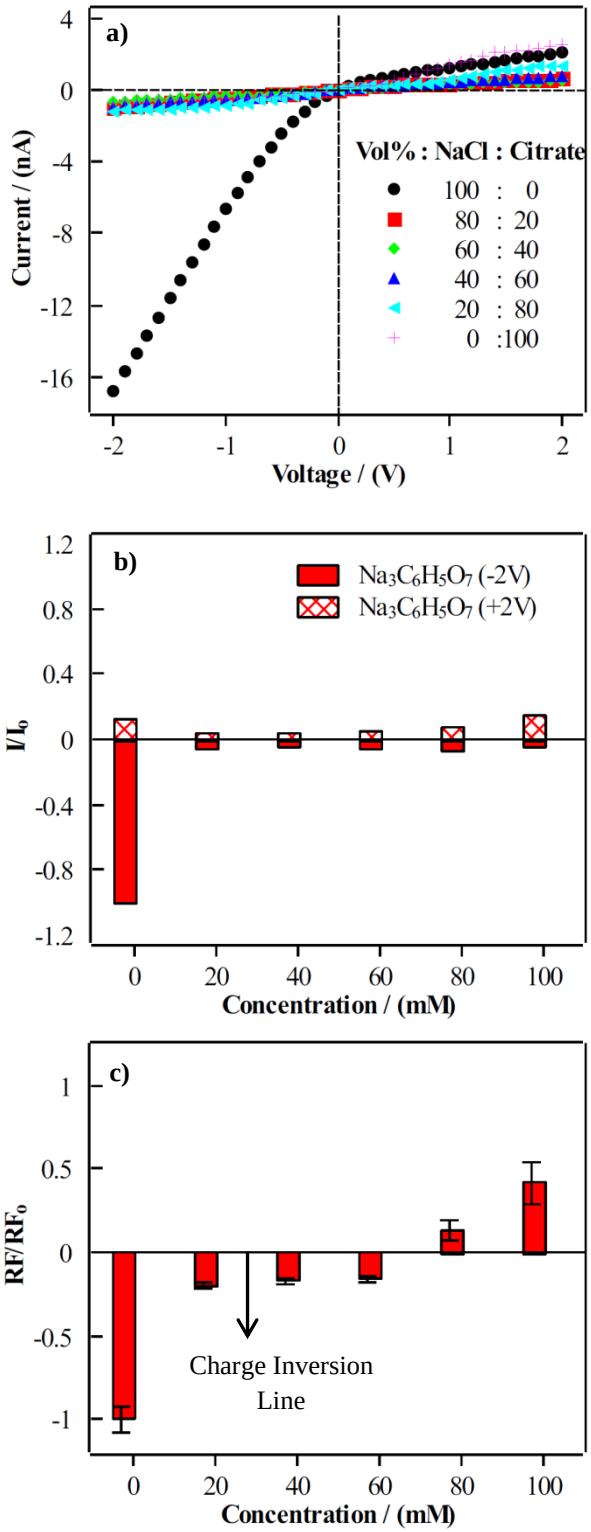

Figure 39: Investigation of transportation behaviour of $Na_3C_6H_5O_7$ inside the PAH-modified nanopore. The total concentration of anions in each salt solution was fixed at 100mM. *I-V* curves were obtained for different concentration of (a) $Na_3C_6H_5O_7$ (b) Normalised current values were obtained for different concentration of $Na_3C_6H_5O_7$ (c) Normalised rectification factors were obtained for different concentration of $Na_3C_6H_5O_7$.

3.3 Conclusion

The unmodified negatively charged conical nanopore exhibited positive rectification behaviour when exposed to 100 mM NaCl or KCl solutions. PAH modified conical nanopore showed negative rectification behaviour when exposed to the aforementioned solutions. The unmodified and PAH-modified nanopores preferentially transport cations and anions, respectively. The unmodified nanopores exhibited negative rectification behaviour when exposed to a 100 mM NaCl solution with a pH of 1.5. The reason can be attributed to the double protonation of carboxylate ions. The exposure of an unmodified nanopore to a multivalent cation leads to the surface charge neutralisation or inversion. The reason for the charge inversion or neutralisation can be attributed to the strong electrostatic interaction between the cations and the carboxylate ions. Anions did not affect the surface charges of an unmodified nanopore. Monovalent anions such as $H_2PO_4^-$ and HCO_3^- partially invert the surface charges of PAH-modified nanopores. On the other hand, SO_4^{2-} being a divalent anion was unable to neutralise or invert the surface charges. Only HPO_4^{2-} was able to invert the surface charges from positive to negative to a large extent.

Chapter 4. Osmotic Energy Harvesting Using Cation Selective Membranes

4.1 Introduction

The problems created due to intense usage of fossil fuels have prompted various organisations to launch worldwide campaigns pertaining to climate change [94-98]. Many developed countries have started to invest in alternative energy, while some oil-rich countries have started to diversify their economies due to dwindling oil reserves. Nuclear power plants can produce cheap and clean electricity. However, the safety of nuclear power plants remains questionable after the Fukushima and Chernobyl incidents [99]. In addition, the disposal of nuclear waste is a challenging and laborious task. Cheap and clean electricity can be obtained from other sources such as solar, tidal, wind and hydal [100-103]. These sources are renewable, safe and environmentally friendly. Nowadays, scientists are working to obtain electrical energy from other alternative sources such as temperature, pressure and salinity gradients [104-106].

The osmotic energy set-up uses a membrane separating two compartments containing salt solutions of different molarity [107,108]. A charged and porous membrane with an average diameter in the nanoscale is used in the set-up. The presence of charged species at the surface of the pore results in the formation of an overlapping double layer [74,75]. Introducing the membrane to a concentration gradient prompts the preferential diffusion of counterions and consequently resulting in generation of a diffusional or transmembrane potential between two electrodes [109,110].

The porous polyimide (PI) membrane is a chemically and mechanically stable membrane [111]. Conventionally, the pores inside PI membranes are fabricated by a two-step process: first, PI membrane is irradiated with heavy ions followed by etching with sodium hypochlorite solution [112,113]. In the conventional etching technique, the bulk material and the damage trail present inside the tracks are etched by breaking the imide linkage [35]. The sub-nanometer pore within PI membrane cannot be fabricated using the conventional etching technique. In the previous studies, the sub-nanometre pores were fabricated within PET by UV irradiation for a prolonged period [114].

Some of the sentences, paragraphs and diagrams of this chapter of the thesis were published in following journal article
"**Osmotic energy harvesting with soft-etched nanoporous polyimide membranes** || ***M.H.A. Haider***, *S. Nasir, M. Ali, P. Ramirez, J. Cervera, S. Mafe, W. Ensinger* || https://doi.org/10.1016/j.mtener.2021.100909

Hydrogels are used in a variety of applications such as heavy metal ion filtration, energy harvesting, biomedical applications and bioseparation [115-119]. Charged hydrogels with high charge density and small mesh size can be used in ion selective membranes [117]. The hydrogels gain their net charge through the presence of polar functional groups such as carboxylate group, sulfonate group or phosphonate groups. Hydrogels are often brittle and break when subjected to compression loads [120].

Several studies have been conducted in the field of osmotic energy harvesting using charged polymer membranes. Lauciric *et al.* have synthesised a bullet-shaped nanopore in a PET membrane for the energy harvesting application [61]. Chen et al. have achieved a power density of 11.72 W/m^2 (membrane test area was 3.0 × 10^4 μm^2) using hydrogel-hybrid membrane that was synthesised by incorporation of acrylic acid-co-acrylamide-co-methyl methacrylate hydrogels into a track etched polycarbonate membrane [117]. Similarly, Blame et al. have synthesised hydrogel based membrane by incorporating negatively and positively charged hydrogel inside the conical and cylindrical pores [107].

In this chapter, performance analyses of two different membranes, namely PI and HP membranes, were carried out. The pores inside the PI membranes were fabricated using the soft etching technique. In the case of the HP membranes, the acrylic acid hydrogel was incorporated inside the pores of the PET support. The support membrane has a fluence of 10^8 pores/cm^2 and an average pore diameter in the range of 180-260 nm.

An electric current is generated when the aforementioned membranes are exposed to an asymmetric salt gradient. The membranes are fixed between two cells: one was filled with a high salt concentrated solution (C_H) and the other cell was filled with a low salt concentrated solution (C_L). The performance of the membranes was evaluated by testing under various parameters and conditions such as changes in the value of concentration gradient, fluence, acrylic acid concentration, stability test and pH. The use of Ag/AgCl electrodes (3M KCl) prevents generation of the redox potential, allowing the diffusional potential (E_{diff}) or transmembrane potential to be equivalent to the reversal potential (V_{rev}) [61]. pH values of all of the solutions used in the section were between 5.8-6.3, unless otherwise specified. Potassium chloride salt solutions were used in the study.

4.2 Analysis of *I-V* curve

Figure 40a shows an *I-V* curve that was obtained by exposing the HP membrane to a concentration gradient. Several different regimes are shown in Figure 40b,c,d,e: Electrodialysis (ED) regime, V_{rev} point (electrical force overcomes diffusion), Reverse Electrodialysis (RED) regime, I_o (zero-voltage current) and Voltage Assisted Reverse Electrodialysis regime (VARED) [121]. The orange coloured dot (I_o) on the y-axis represents the net movement of cations down the concentration gradient in the absence of a voltage bias.

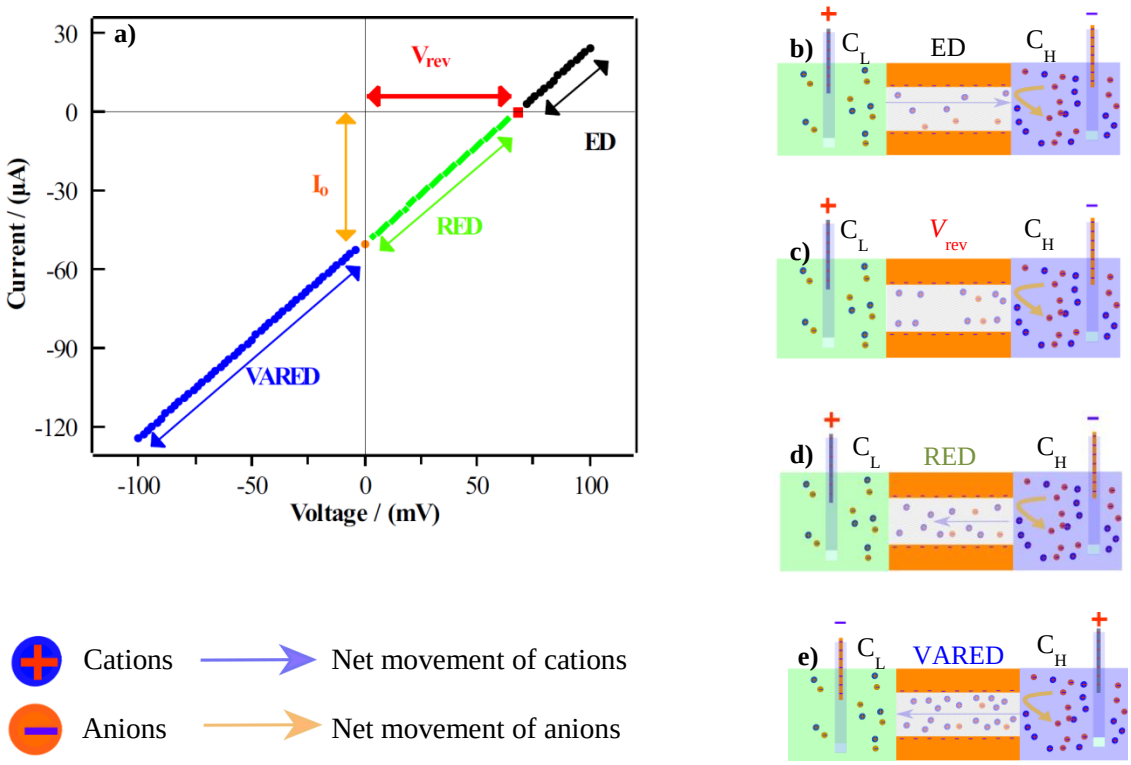

Figure 40: (a) *I-V* graph of the HP membrane exposed to a concentration gradient. Schematic illustration of different regimes (b) Electrodialysis (ED) (c) V_{rev} (Reversal Potential) point (d) Reverse Electrodialysis (RED) (e) Voltage assisted Reverse Electrodialysis (VARED).

The current in *I-V* curves represents the net cation flux which is determined by two individual fluxes: the diffusional flux and the migration flux [50]. The diffusional flux is driven by the concentration gradient, while the migration flux is driven by an externally applied voltage [121]. In the RED regime, the direction of the electric force (due to voltage) is opposite to that of the diffusion flux [121]. In addition, the magnitude of the migration flux is smaller compared to the diffusion flux [121]. Therefore, the movement of the net cation flux is down the concentration gradient in the RED regime [121]. It can be noticed in the RED regime (Figure 40a) that the

current decreases immediately when a variable voltage signal is applied. The decrease in the current values indicates a reduction in the transmembrane cation flux [121]. At the x-intercept, the electric force is strong enough to overcome the diffusion resulting in a net zero cationic flux across the membrane [121]. The ED regime is indicated by black colour in Figure 40a, wherein the direction of the net cation flux is against the concentration gradient, i.e., opposite to the RED regime [121]. The VARED regime is shown in blue colour in Figure 40a, where the diffusive flux and the migration flux have a similar direction, i.e., down the concentration gradient [121]. The increase in the voltage results in an increase in net transmembrane cation flux [121].

4.3. Result and discussion: Porous polyimide cation selective membrane

4.3.1 Effect of concentration gradients variation

The study investigated the influence of the variation in concentration gradient or concentration fold on the performance of the PI membrane. For this purpose, the sub-nanometer PI membrane with a fluence of 8.0×10^{8} pores/cm^2 was tested in various concentration folds, represented by the ratio C_H/C_L. C_H denotes the concentration of concentrated salt solution in the high-concentration-salt-solution cell, whereas C_L denotes the concentration of dilute salt solution in the low-concentration-salt-solution cell (Figure 25). Throughout the investigation, C_H was kept constant while C_L was systematically increased in an ascending order. Potassium Chloride (KCl) was used as the salt in the investigation. Figure 41 shows the results of three different experimental sets: A, B and C.

In experiment set A, the molarity of C_H was fixed at 100 mM while the molarity of C_L was incrementally increased from 1 mM to 50 mM. The results in Figure 41a(i) indicate a progressive increase in the magnitude of V_{rev} with the increase in the C_H/C_L ratio. The highest value of V_{rev} was 100 mV, which was obtained at a C_H/C_L ratio of 100, while the lowest value of V_{rev} was 12 mV obtained at a C_H/C_L ratio of 2. An irregular trend of the I_o was observed with the increment in the C_H/C_L ratio (Figure 41a(i)). The I_o values obtained at C_H/C_L ratios of 100, 10 and 2 were -5.9 µA, -8.5 µA and -2.9 µA, respectively. The term cation transport number (t_+) represents the cation selectivity of a membrane and was calculated using equation 6 (please refer to Chapter 1, section 1.10) [61,70]. An ideal cation selective membrane has a t_+ value of 1, while a non-selective membrane has a t_+ value of 0.5. Figure 41a(ii) shows that the t_+ value of the PI membrane increased with increasing C_H/C_L ratio. At the C_H/C_L ratio of 100, 10 and 2, the values

of t_+ were 0.945, 0.927 and 0.869, respectively. The values of maximum power (P_{max}) and maximum efficiency (η_{max}) values increased with increasing C_H/C_L ratio (Figure 41a(iii)). P_{max} and η_{max} were calculated using mathematical equations 7 and 8, respectively (please refer to Chapter 1, section 1.10). The maximum values of P_{max} (0.152 µW) and η_{max} (39.6%) were obtained at a C_H/C_L ratio of 100 in the experimental set A.

The *I-V* curves of the experimental set B are shown in Figure 41b(i). In set B, the C_H was fixed at 500 mM while the C_L was incrementally increased from 1 mM to 100 mM. The increase in the C_H/C_L ratio resulted in a gradual increase in the V_{rev}. The highest V_{rev} value of 111 mV was obtained at a C_H/C_L ratio of 500. Conversely, the highest I_o value of -11.4 µA was obtained at a C_H/C_L ratio of 50. The maximum t_+ value of 0.87 was obtained at a C_H/C_L ratio of 500 (Figure 41b(ii)). The maximum values of P_{max} and η_{max} were 0.181 µW and 27.6% were obtained at C_H/C_L ratios of 50 and 500, respectively, as shown in Figure 41b(iii).

For the experimental set C, the C_H was fixed at 1000 mM while the C_L was increased from 1 mM to 500 mM. Figure 41c(i) shows the maximum values of V_{rev} (123 mV) and I_o (-13.4 µA) were obtained at C_H/C_L ratios of 1000 and 100, respectively. Figure 41c(ii) demonstrates an increase in the t_+ values with increasing C_H/C_L ratio, with the highest t_+ value achieved at a C_H/C_L ratio of 1000. In set C, the highest P_{max} value of 0.244 µW was achieved at a C_H/C_L ratio of 100, which was the highest of all the experimental sets (Figure 41c(ii)).

An increase in the C_H/C_L ratio results in a higher net driving force of diffusion, consequently resulting in an augment of V_{rev} [122,123]. The aforementioned relationship has been documented in the previous literature where an increase in the ratio resulted in an increase of V_{rev} in the surface charge density controlled conditions [122].

It might be expected that an increase in the C_H/C_L ratio would lead to a surge in the I_o values. However, Figure 41c(i) (experimental set C) shows that the I_o value obtained at the C_H/C_L ratio of 1000 was lower than the I_o values obtained at the other C_H/C_L ratios. Moreover, a similar anomaly can also be noticed in Figure 41b(i) (experimental set B) and Figure 41a(i) (experimental set A). The anomaly can be due to a phenomenon called concentration polarisation (CP). The CP causes an increase in the transmembrane ion flow resistance consequently resulting in a reduction in the transmembrane flux, which subsequently leads to a decrease in the current values [57].

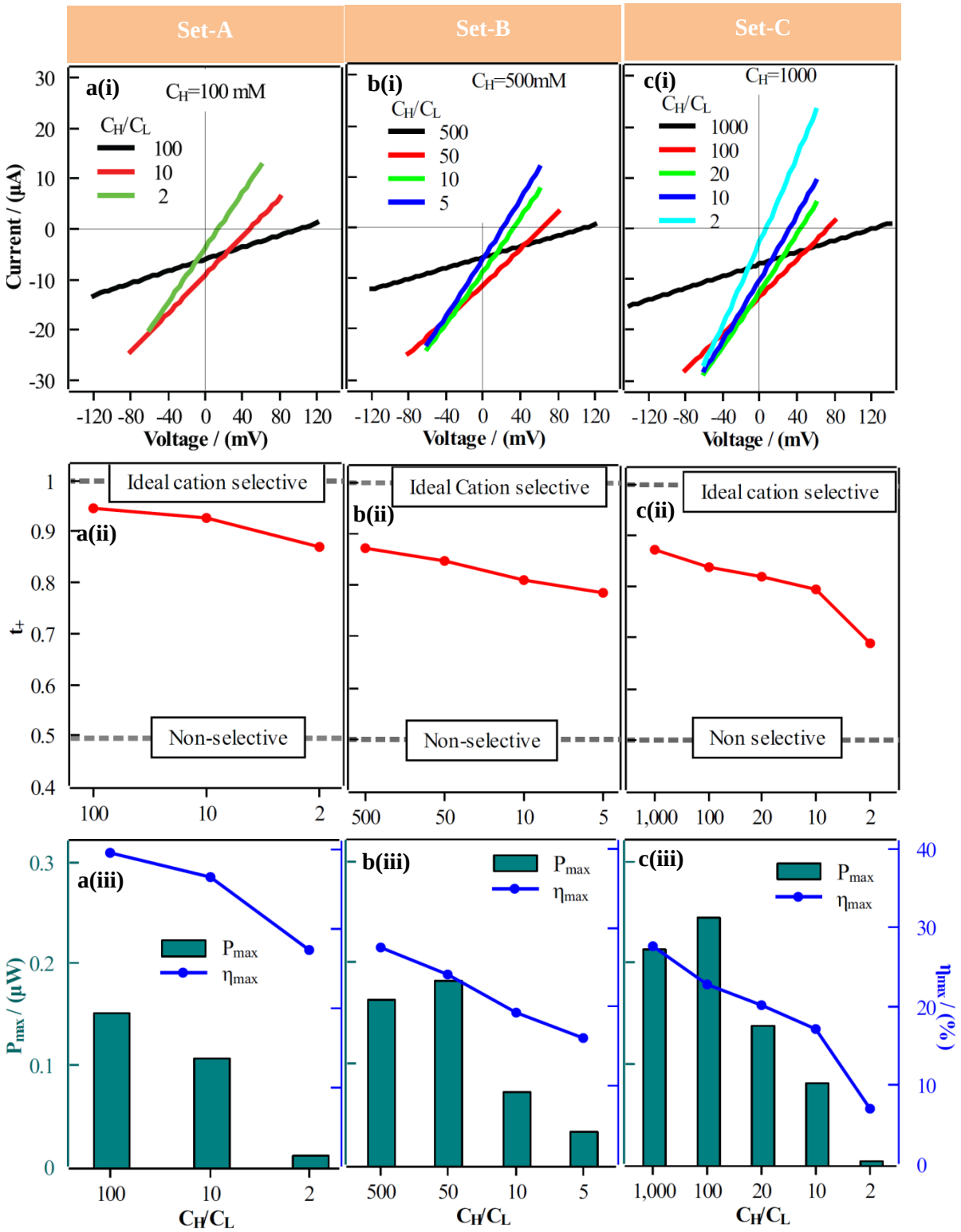

Figure 41: PI membrane having a fluence of 8.0×10^{8} pores/cm^2 exposed to different concentration gradients a(i) *I-V* graphs of experimental set-A a(ii) cation selectivity vs C_H/C_L ratio of experimental set-A a(iii) P_{max} and η_{max} vs C_H/C_L ratio of experimental set-A b(i) *I-V* graphs of experimental set-B b(ii) cation selectivity vs C_H/C_L ratio of experimental set-B b(iii) P_{max} and η_{max} vs C_H/C_L ratio of experimental set-B c(i) *I-V* graphs of experimental set-C c(ii) cation selectivity vs C_H/C_L ratio of experimental set-C c(iii) P_{max} and η_{max} vs C_H/C_L ratio of experimental set-C.

4.3.2 Impact of ion fluence on membrane performance

The study investigated the impact of fluence on the performance of the PI membrane. Membranes with fluence ranging from 4.0×10^{8} pores/cm^2 to 4.0×10^{10} pores/cm^2 were introduced to different concentration folds (C_H/C_L =100, 20 and 10). Previous studies have demonstrated that the power density of an ion-selective membrane shows an inverted V-shaped trend with increasing fluence [122,123]. Therefore, it is evident that the fluence of the membrane has a substantial effect on the performance.

Initially, the PI membranes were exposed to a C_H/C_L ratio of 100. An increasing trend in the I_o value was observed up to a fluence value of 4.0×10^{9} pores/cm^2. Subsequently, the I_o values decreased with further increase in fluence (Figure 42a(i)). The PI membrane with a fluence of 4.0×10^{10} pores/cm^2 exhibited the lowest current value of -13.1 μA. The V_{rev} values (77 mV) remained approximately constant up to the fluence of 4.0×10^{9} pores/cm^2, followed by a decrement in the value as the fluence increased further (Figure 42a(i)). The PI membrane with a fluence of 4.0×10^{10} pores/cm^2 exhibited the lowest V_{rev} value of 38mV, which was half of the value, which the other membranes exhibited.

The trend of t_+ as a function of fluence is shown in Figure 42a(ii). The values of t_+ were approximately constant (0.84) for the fluences ranging from 4.0×10^{8} pores/cm^2 to 4.0×10^{9} pores/cm^2, followed by a decreasing trend in t_+ with further increase in fluence. The PI membrane with a fluence of 4.0×10^{10} pores/cm^2 exhibited the lowest t_+ value (0.68). The trend of P_{max} and η_{max} in relation to fluence is shown in Figure 42a(iii). The PI membrane with a fluence of 4.0×10^{9} pores/cm^2 exhibited the highest P_{max} (0.45 μW) and η_{max} (25.5%) values (Figure 42a(iii)). Conversely, the lowest P_{max} (0.13 μW) and η_{max} (6.2%) values were exhibited by the PI membrane with a fluence of 4.0×10^{10} pores/cm^2.

Additionally, the PI membranes were also exposed to other concentration folds of 20 and 10. Figure 42b(i) and c(i) show that V_{rev} remained approximately constant up to a critical value of fluence. A further increase in fluence led to the decline in V_{rev} values. Notably, the I_o values increased up to a fluence of 8.0×10^{9} pores/cm^2 but subsequently deceased with further increase in fluence. The data presented in Figure 42b(ii) and b(iii) and Figure 42c(ii) and c(iii) show that the t_+ and η_{max} values also remained approximately constant for fluences up to 4.0×10^{9} pores/cm^2.

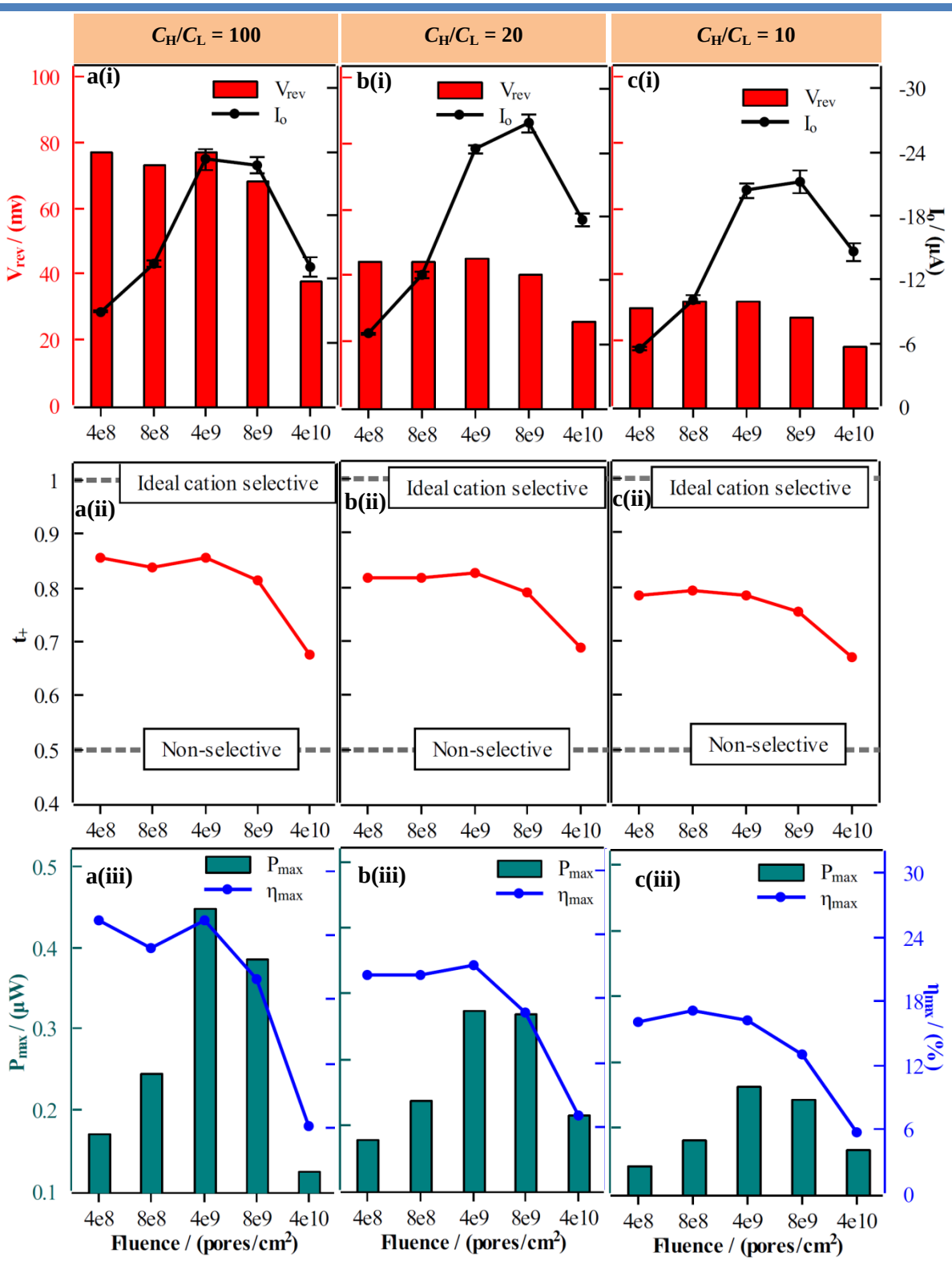

Figure 42: The effect of fluence on the performance of PI membranes. The membranes were exposed to different C_H/C_L ratios, i.e., 100, 20 and 10 a(i) V_{rev} and I_o vs fluence (C_H/C_L=100) a(ii) cation selectivity vs fluence (C_H/C_L=100) a(iii) P_{max} and η_{max} vs fluence (C_H/C_L=100) b(i) V_{rev} and I_o vs fluence (C_H/C_L=20) b(ii) cation selectivity vs fluence (C_H/C_L=20) b(iii) P_{max} and η_{max} vs fluence (C_H/C_L=20) c(i) V_{rev} and I_o vs fluence (C_H/C_L=10) c(ii) cation selectivity vs fluence (C_H/C_L=10) c(iii) P_{max} and η_{max} vs fluence (C_H/C_L=10).

Increasing the fluence beyond a certain value enhances the probability of pores overlapping, resulting in enlarged pores and consequently leading to a decrease in V_{rev} and I_o values. The overlapping of the pores resulted due to the random bombardment of the ions during the SHI process. Figure 43 shows the gradual darkening progression of the SHI-irradiated PI membrane with increasing fluence. The colour change indicates the overlapping of the tracks with increasing fluence. The increase in the mean pore diameter led to a decline in cation selectivity, and subsequently a decrease in the V_{rev} and I_o values.

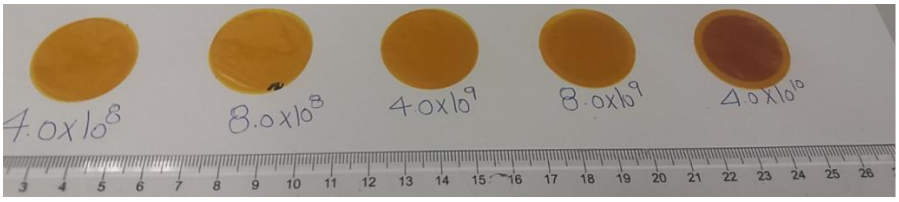

Figure 43: The figure shows the snapshot of four PI membrane having different fluences, the colour of PI membrane grew darker with the increase in the fluence.

4.3.3 Performance of PI membrane in acidic medium

The performance of a PI membrane was investigated in an acidic medium (pH=3.0) and compared with a light-acidic or a near-neutral solution with a pH ranging between 5.8-6.3. KCl salt solutions with pH values of 3 and 5.8-6.3 were used in the investigation. The PI membrane with a fluence of 4.0×10^9 pores/cm^2 was exposed to various concentration gradients ranging from 1000 to 10. Figure 44a and b show the results of the experiments carried out in the near-neutral and acidic media, respectively. A comparison of Figure 44a(i) and b(i) shows that the values of V_{rev} and I_o were lower in the acidic medium. In the acidic medium, the peak values of V_{rev} (23 mV) and I_o (-6.2 μA) were achieved at a C_H/C_L ratio of 1000 and 20, respectively. However, in the near-neutral condition, the values of V_{rev} (112 mV) and I_o (-23.2 μA) were significantly higher compared to the acidic medium at the above mentioned C_H/C_L ratios (1000 and 20).

Figure 44a(ii) and b(ii) reveal that the t_+ values were lower in the acidic medium, which were close to 0.5 at any given C_H/C_L ratio. Additionally, the power output was also comparatively lower in the acidic medium compared to the near-neutral medium (Figure 44a(iii) and b(iii)). At a C_H/C_L ratio of 100 in the acidic medium, the highest values of t_+ and P_{max} were 0.59 and 0.031 μW, respectively.

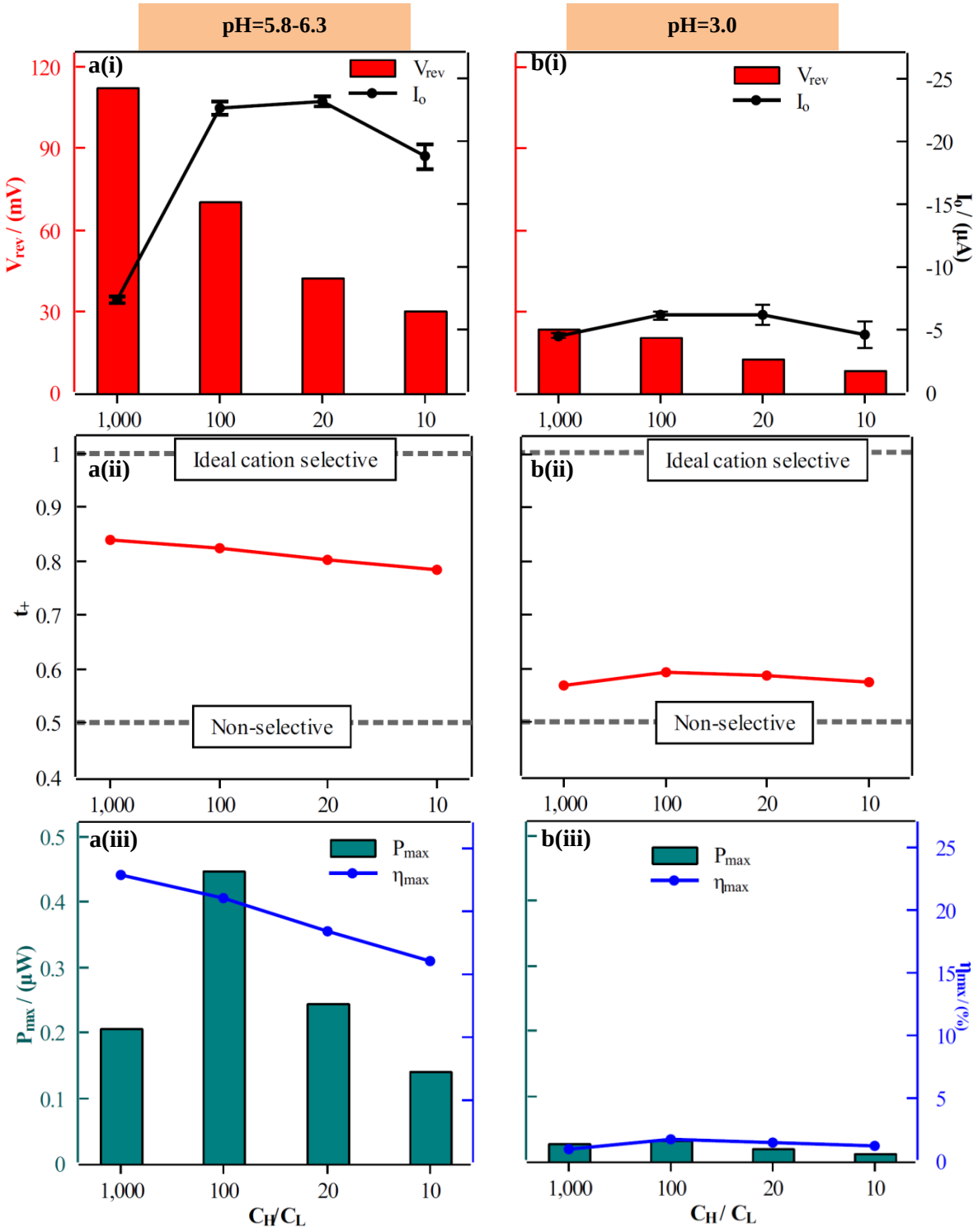

Figure 44: The effect of pH on the performance of the PI membrane having fluence of 4.0×10^9 pores/cm^2. a(i) V_{rev} and I_o vs C_H/C_L (pH = 5.8-6.3) a(ii) cation selectivity vs C_H/C_L (pH = 5.8-6.3) a(iii) P_{max} and η_{max} vs C_H/C_L (pH = 5.8-6.3) b(i) V_{rev} and I_o vs C_H/C_L (pH = 3) b(ii) cation selectivity vs C_H/C_L (pH = 3) b(iii) P_{max} and η_{max} vs C_H/C_L (pH = 3).

A net negative charge on the surface of the PI membrane was due to the presence of carboxylate ions. The concentration of H^+ ions is higher in the acidic medium compared to the near-neutral medium. In the acidic medium, carboxylate ions (COO^-) present on the surface walls become protonated (COOH), which reduces the surface charge density. The decrease in the charge density had a negative impact on cation selectivity, which ultimately resulted in inferior membrane performance.

4.3.4 Comparison between parallel porous structure and networked structure

A comparative analysis was carried out between the PI membranes with parallel porous structures (PPS) and network porous structures (NPS). The pores in the PPS membrane were parallel to each other and perpendicular to the membrane's surface. In contrast, the pores in the NPS membrane cross each other. The NPS and PPS membranes with fluences ranging from 4.0×10^8 to 8.0×10^9 pores/cm^2 were exposed to a concentration gradient (C_H/C_L =100). KCl solution was used as the solution in the current investigation. The V_{rev} values obtained with the PPS membranes and NPS membranes were approximately equal, as shown in Figure 45a(i) and b(i). The PPS membranes with fluences of 4.0×10^8 pores/cm^2, 8.0×10^8 pores/cm^2, 4.0×10^9 pores/cm^2 and 8.0×10^9 pores/cm^2 exhibited V_{rev} values of 77 mV, 73 mV, 77 mV and 68 mV, respectively.

Theoretically, it could be expected that the I_o values obtained with the PPS membranes should be approximately similar to the I_o values obtained with the NPS membranes. However, it was observed that lower I_o values were obtained with the NPS membranes with fluences of 4.0×10^8 pores/cm^2 and 8.0×10^8 pores/cm^2, compared to the PPS membranes. It can be said that the NPS membrane with fluences of 4.0×10^8 pores/cm^2 and 8.0×10^8 pores/cm^2 were not properly soft-etched, resulting in low I_o values.

The t_+ values obtained with the PPS and NPS membranes were quite identical (Figure 45a(ii) and b(ii)). The P_{max} values obtained with the PPS membranes were relatively higher compared to the NPS membranes at the fluences of 4.0×10^8 pores/cm^2 and 8.0×10^8 pores/cm^2, which was due to the higher I_o values obtained in the case of the PPS membranes. However, the NPS structured membrane with a fluence of 4.0×10^9 pores/cm^2 demonstrated slightly higher P_{max} compared to its counterpart (Figure 45a(iii) and b(iii)). Both types of membranes exhibited roughly similar η_{max}.

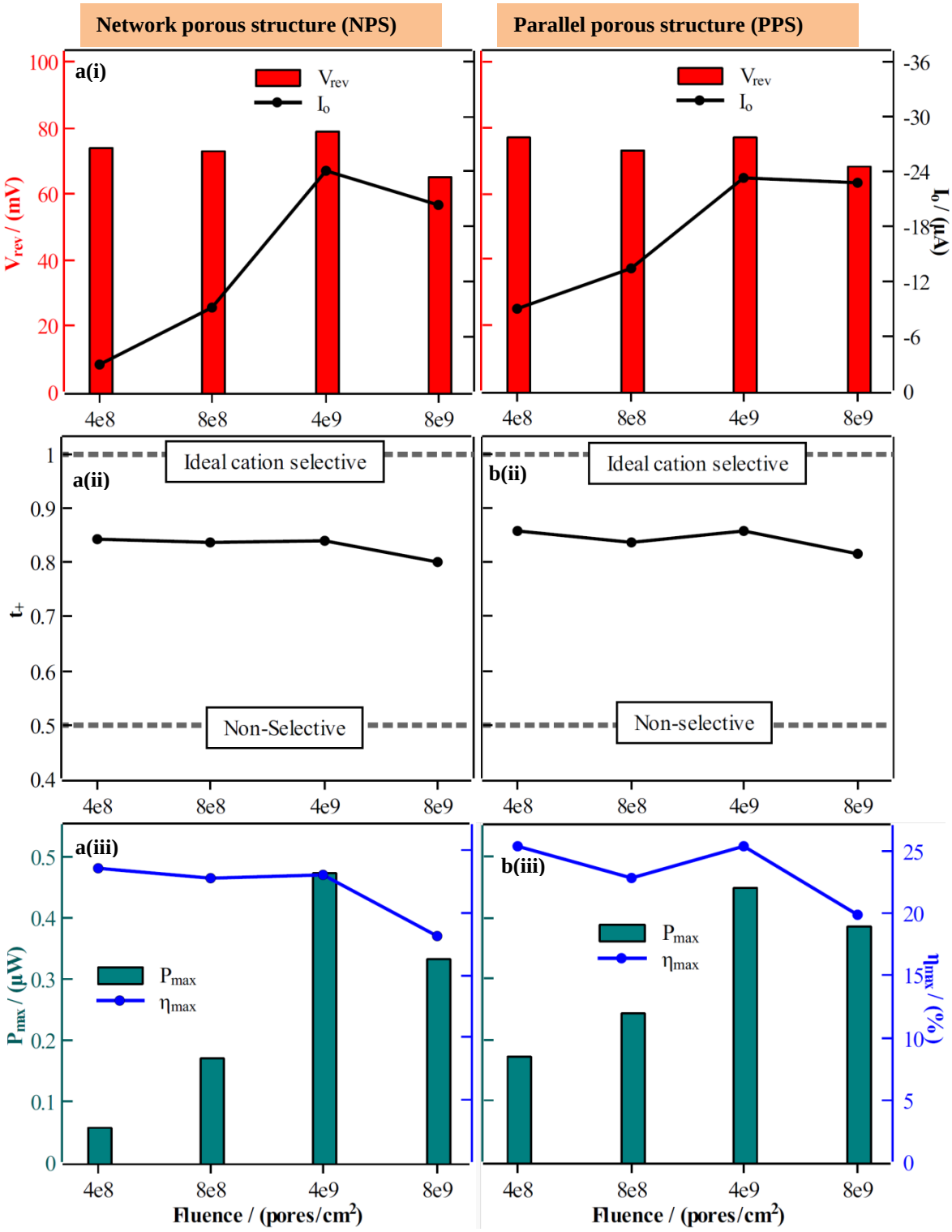

Figure 45: A comparison analysis between the Networked porous structure membrane (NPS) and Parallel porous structure (PPS). The membranes were exposed to C_H/C_L = 100. a(i) V_{rev} and I_o vs fluence (NPS) a(ii) cation selectivity vs fluence (NPS) a(iii) P_{max} and η_{max} vs fluence (NPS) b(i) V_{rev} and I_o vs fluence (PPS) b(ii) cation selectivity vs fluence (PPS) b(iii) P_{max} and η_{max} vs fluence (PPS).

4.3.5 Effect of multivalent cations on the performance of PI membrane

The effect of a multivalent cation (Ca^{2+}) on the performance of the PI membrane was investigated and compared with K^{+}. A PI membrane with a fluence of 8.0×10^{8} pores/cm^{2} was fixed between two cells. In the first case, one of the cells was filled with 1 mM KCl solution (C_L), while the other cell (C_H) was filled with 1000 mM KCl. V_{rev} and I_o values of 122 mV and -7.0 µA, respectively (Figure 46a), were obtained in the first case.

In the second case, one of the cells was filled with 1 mM $CaCl_2$ (C_L) and the other cell was filled with 1000 mM KCl. The result of the second case shows that the values of I_o and V_{rev} were -8.35 µA and 33 mV, respectively. Compared to the first case, the value of P_{max} (0.07 µW) obtained in the second case was comparatively lower (Figure 46b and c).

In the third case, the performance of the PI membrane was severely affected when one of the cells was filled with 1 mM KCl and the other with 1000 mM $CaCl_2$. In the third case, the values of V_{rev} and I_o were 9 mV and -0.4 µA, respectively. Furthermore, negligible value of P_{max} was generated, which can be approximated as zero (0) watts (Figure 46c).

Ca^{2+} has a strong electrostatic affinity for carboxylate ions. The strong affinity resulted in an effective surface charge neutralisation, consequently, the pores became non-selective. In the fourth and last case, the cells were filled with 1 mM and 1000 mM $CaCl_2$. In the last case, the values of V_{rev} and I_o were -28 mV and +2.72µA, respectively. In the last case, the signs of V_{rev} and I_o were opposite to those of former cases. Furthermore, the t_+ value of 0.41 and together with the opposite signs of V_{rev} and I_o indicate that the surface polarity of the membrane had been reversed from negative to positive due to electrostatic interaction between Ca^{2+} and carboxylate ions. As a consequence of the surface charge inversion, the membrane preferentially transported anions. Therefore, it can be concluded that multivalent cations have the potential to reverse the net surface charge of the membrane.

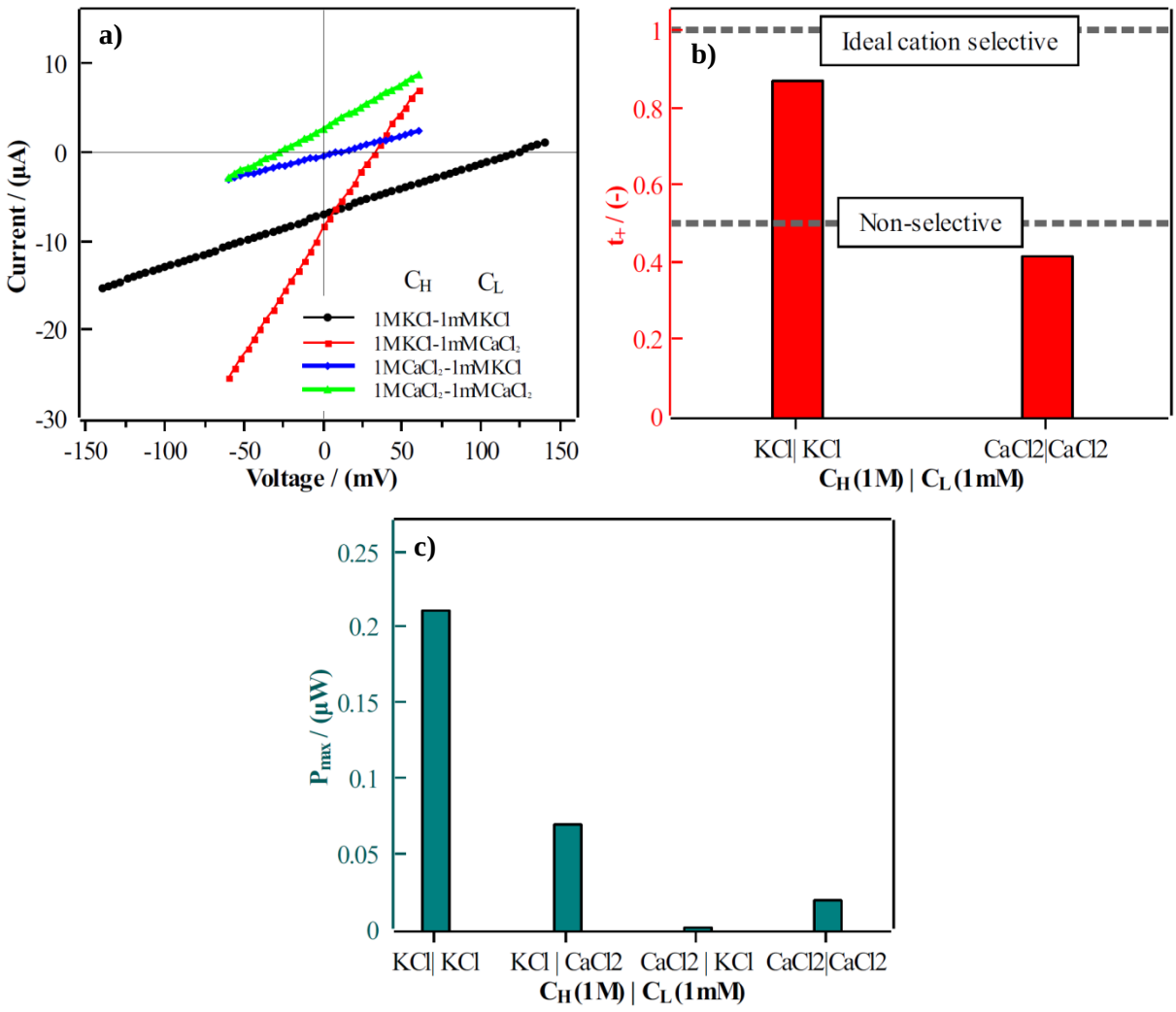

Figure 46: Effect of multivalent cation on the performance of PI membrane having fluence of 8.0×10^8 pores/cm^2. (a) *I-V* curves (b) cation transfer number (c) P_{max} and η_{max}.

4.3.6 Time dependent investigation

The time dependent performance of the PI membrane was investigated. The PI membrane with a fluence of 8.0×10^8 pores/cm^2 was exposed to a concentration gradient of 100 (C_H/C_L = 100). The solutions were left in the cells for 15 days. The value of V_{rev} decreased with each passing day, as shown in Figure 47a. The value V_{rev} obtained on first day was 94 mV, which reduced to 62 mV at the end of the 15th day. The values of I_o increased until the 10th day, following a gradual decline of I_o with time. P_{max} remained approximately constant for ten days, and thereafter it began to decline (Figure 47b).

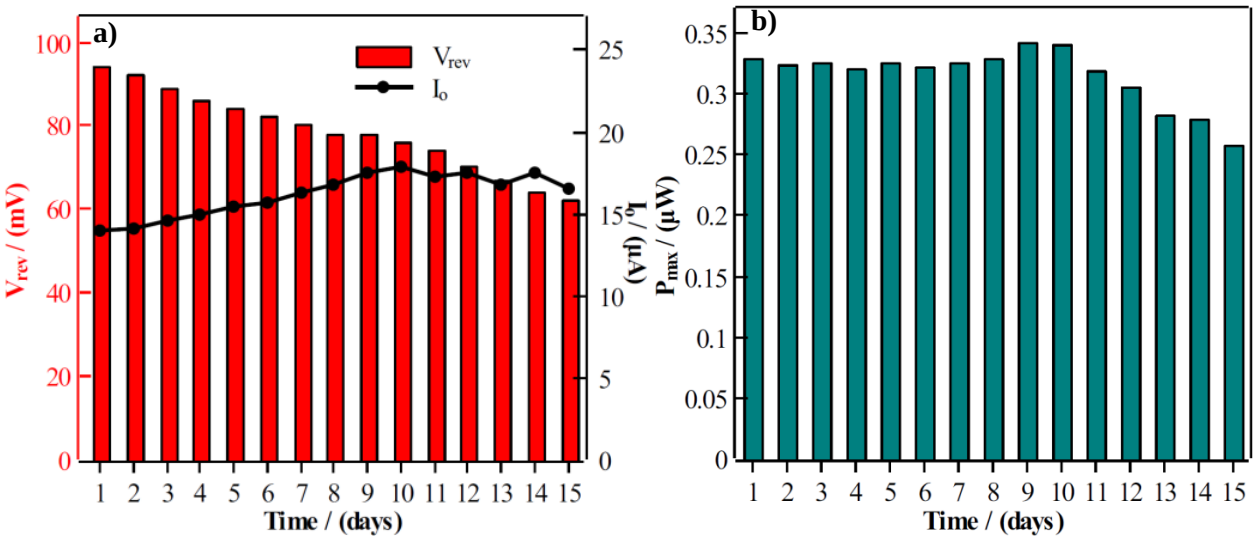

Figure 47: Time dependent investigation (a) V_{rev} and I_o vs time (b) P_{max} vs time.

4.4 Result and discussion: Acrylic acid hydrogel-PET cation selective membrane

The acrylic acid hydrogel was incorporated into the PET support foil. The fluence and thickness of the PET foil were 1.0×10^8 pores/cm^2 and 12 µm, respectively. The hydrogel-PET membrane (HP) was negatively charged and preferentially transported cations. Therefore, the membrane generated an electric current when exposed to a concentration gradient. Note that the pH values of all KCl solutions used in the *I-V* experiments in this section were in the range of 5.5-6, unless otherwise stated.

The red arrows in Figure 48(a-f) point towards the acrylic acid hydrogel rods within the PET support. It can be seen in Figure 48 that certain channels lack hydrogel rods. This can be due to two reasons: either the hydrogel nanorods were not formed inside the channels or the hydrogel rods were destroyed during incision of the membrane. It was quite possible that the hydrogel-solution did not properly penetrate into the nanochannels with small opening diameter, and therefore the hydrogel rods were not formed inside the channels upon curing. The HP membranes were immersed in liquid nitrogen to prevent tearing. During immersion, it was noticed that the HP membranes did not become fully brittle, which led to the tearing during the incision and resulted in the destruction and disfigurement of nanochannels and hydrogel rods.

For further analysis, the hydrogel was also incorporated into a porous polycarbonate membrane. The PC membrane had networked porous structure and a thickness of 20 µm, with marginally

larger pores than PET. Hydrogel rods can be viewed within the PC membrane, as shown in Figure S2. The crosslinked porous structure facilitated the interconnectivity of the hydrogel rods inside the pore, resulting in higher structural stability. Moreover, due to proper embrittlement of PC foils, the tearing of the pores was comparatively less than the PET foil.

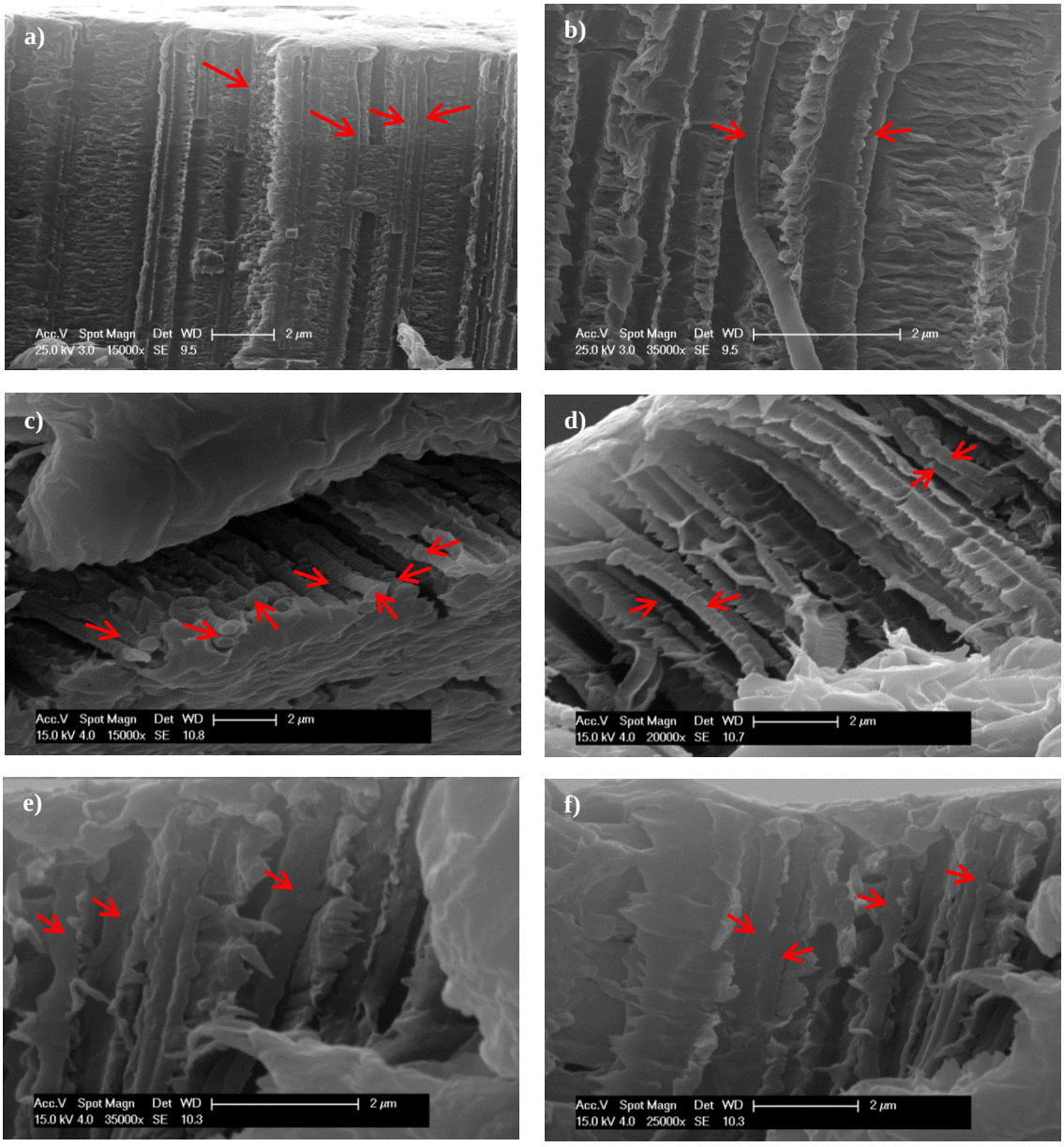

Figure 48: (a-f) SEM images of cross section of HP membranes. The red coloured arrows are pointing towards the hydrogel rods present inside the pores of PET support membrane.

4.4.1 FTIR analysis

Figure 49 shows the FTIR curves of the plain PET foil, the freeze-dried acrylic acid hydrogel and the HP membrane. The FTIR analysis was performed to confirm the presence of carboxylic acid groups within the HP membrane. A large peak around 1720 cm^{1-} is detected in all of the three curves, which is due to the presence of carbonyl groups (C=O) in ester groups or carboxylic acid groups. Another peak around 3000 cm^{1-} is detected in the HP membrane and acrylic acid hydrogel peak. The peak appears due to the presence of hydroxyl groups in carboxylic acid groups. However, the peak at 3000 cm^{1-} was not detected in the plain PET foil. The results obtained from FTIR and SEM analysis confirms successful incorporation of acrylic acid hydrogel inside the plain etched PET foil.

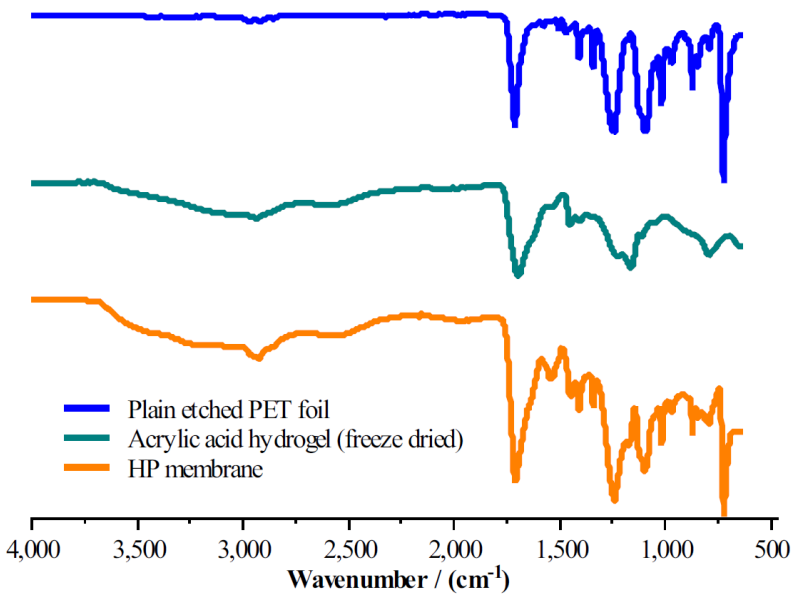

Figure 49: FTIR analysis of the plain etched PET foil, acrylic acid hydrogel (freeze dried) and the HP membrane.

4.4.2 Comparison between plain PET and HP membrane

Figure 50 shows the *I-V* curves of a plain porous PET foil and the HP membrane. Both the membranes were exposed to a concentration gradient of 20 (C_H/C_L =20). Carboxylate ions were present in both membranes and therefore the membranes carried a net negative charged surface. However, the charge density of the HP membrane was higher compared to the plain PET foil. It

can be hypothesised that the HP membrane has higher Debye length to pore diameter ratio in contrast to the plain PET foil. Therefore, the HP membrane favoured the transport of cations down the concentration gradient and provided a barrier to the flow of anions. However, the plain PET membrane did not selectively transport cations or anions. Consequently, an electrical current was generated when the HP membrane was exposed to the concentration gradient, while the plain PET foil was unsuccessful in generating electrical current.

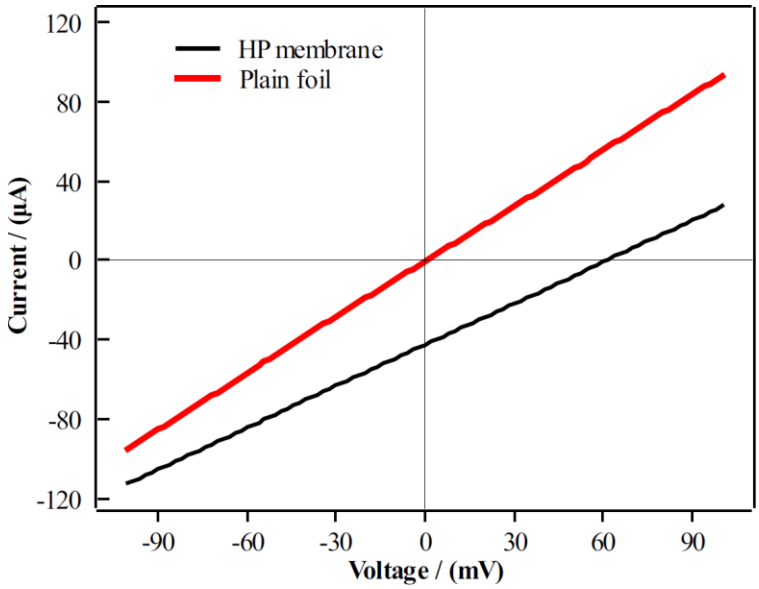

Figure 50: *I-V* curves of the HP membrane and the plain etched PET foil.

4.4.3 Effect of concentration gradients

The study evaluated the performance of the HP membrane in various concentration gradients. The HP membrane prepared with 50 wt% acrylic acid was used in the investigation. KCl solution was used as the electrolyte in the investigation. The molarity of saline solution (C_H) in the high-concentration-compartment cell was fixed, whereas the molarity of saline solution (C_L) in the low-concentration-compartment cell was increased incrementally. Three different experimental sets (A, B and C) were investigated in the study.

Figure 51a(i-iii) presents the outcomes of the experimental set A, where the C_H was fixed at 100 mM KCl solution and the C_L (KCl solution) was incrementally increased from 10 mM to 75 mM. Increasing trends of V_{rev} and I_o were noted with increasing C_H/C_L ratio (Figure 51a(i)). At a C_H/C_L ratio of 10, the membrane displayed the highest V_{rev} and I_o values (50.6 mV and -17.2 µA),

while the lowest V_{rev} and I_o values (4.6 mV and 2.5 µA) were observed at a C_H/C_L ratio of 1.33. Figure 51a(ii) shows that the increase in the C_H/C_L ratio increased t_+ values. The maximum t_+ value of 0.96 was observed at a C_H/C_L ratio of 10 and the minimum t_+ value was observed at a ratio of 1.33 (Figure 51a(ii)). Figure 51a(iii) demonstrates that the values of P_{max} and η_{max} escalated as the C_H/C_L ratio increased. The maximum P_{max} and η_{max} values of 0.217 µW and 42.4%, respectively, were achieved at a C_H/C_L ratio of 10 (experiment set A).

In the other experimental sets (B and C), an increasing trend of V_{rev} was observed with increasing C_H/C_L ratio, as depicted in Figure 51b(i) and c(i). A gradual increase in the values of t_+ was observed as the C_H/C_L ratio increased, as shown in Figure 51b(ii) and c(ii). The increase of t_+ values was noted up to a certain ratio, beyond which further increase of the ratio resulted in a reduction of the t_+ value. Figure 51c(iii) shows the irregular trends of P_{max} and η_{max} with respect to the gradient ratio. The experimental set C yielded the highest P_{max} value of 1.10 µW at a C_H/C_L ratio of 40.

The increase in the concentration gradient ultimately leads to a higher V_{rev}. According to the prior literature, an increasing trend of the V_{rev} in relation to the gradient ratio was observed in the surface charged controlled regime [122]. Conversely, in the bulk solution controlled regime, an increase in the gradient ratio led to a decrease in V_{rev} [122]. In the experimental sets B and C, the I_o values decreased beyond a certain C_H/C_L ratio. The decrease in I_o values might be due to the reduction in transmembrane cation flux caused by a phenomenon known as concentration polarisation (CP).

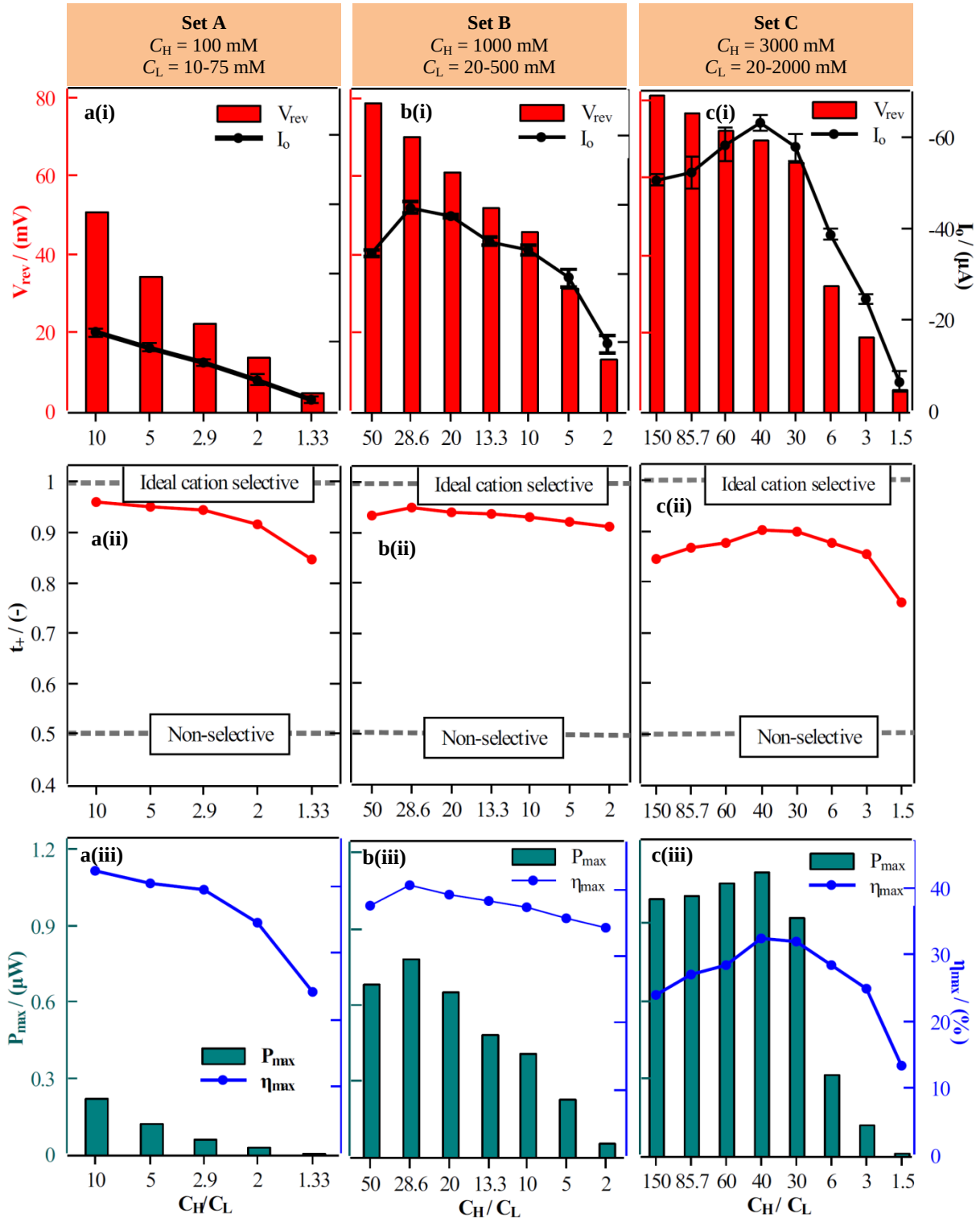

Figure 51: HP membrane exposed to different concentration gradients a(i) V_{rev} and I_o vs C_H/C_L ratio (set-A) a(ii) cation selectivity vs C_H/C_L ratio (set-A) a(iii) P_{max} and η_{max} vs C_H/C_L ratio (set-A) b(i) V_{rev} and I_o vs C_H/C_L ratio (set-B) b(ii) cation selectivity vs C_H/C_L ratio (set-B) b(iii) P_{max} and η_{max} vs C_H/C_L ratio (set-B) c(i) V_{rev} and I_o vs C_H/C_L ratio (set-C) c(ii) cation selectivity vs C_H/C_L ratio of (set-C) c(iii) P_{max} and η_{max} vs C_H/C_L ratio (set-C).

4.4.4 Effect of acrylic acid content in HP membrane

The study analysed the performance of HP membranes prepared with varying acrylic acid content (50%, 45% and 40%), and subjected to different concentration folds (20, 10 and 2). Theoretically, increasing the acrylic acid content inside the membrane should improve the membrane's performance.

Initially, the HP membranes were exposed to the C_H/C_L ratio of 20. Increasing the acrylic acid percentage content within the HP membranes resulted in higher V_{rev} and I_o values, as depicted in Figure 52a(i). Furthermore, the t_+ values also augmented as the acrylic acid content increased (Figure 52a(ii)). The HP membrane prepared with 50 wt% acrylic acid exhibited the highest V_{rev} and I_o values (61.1 mV and -42.5 µA). Likewise, the maximum P_{max} (0.64 µW), t_+ (0.943) and η_{max} (39.1%) were also exhibited by the aforementioned HP membrane (Figure 52a(ii-iii)). The trends of the dependent variables with respect to the acrylic acid content obtained at the concentration folds of 10 and 2, were similar to the trends obtained at the C_H/C_L ratio of 20, as shown in Figure 52b(i-iii), Figure 52c(i-iii).

The experiments led to the conclusion that the performance of the HP membrane decreased as the acrylic acid content inside the membrane was reduced. This was due to a lower fraction of carboxylic acid groups and a lower crosslinking density, which resulted in a decrease in charge density and an increase in mesh size, and consequently led to deterioration in membrane performance.

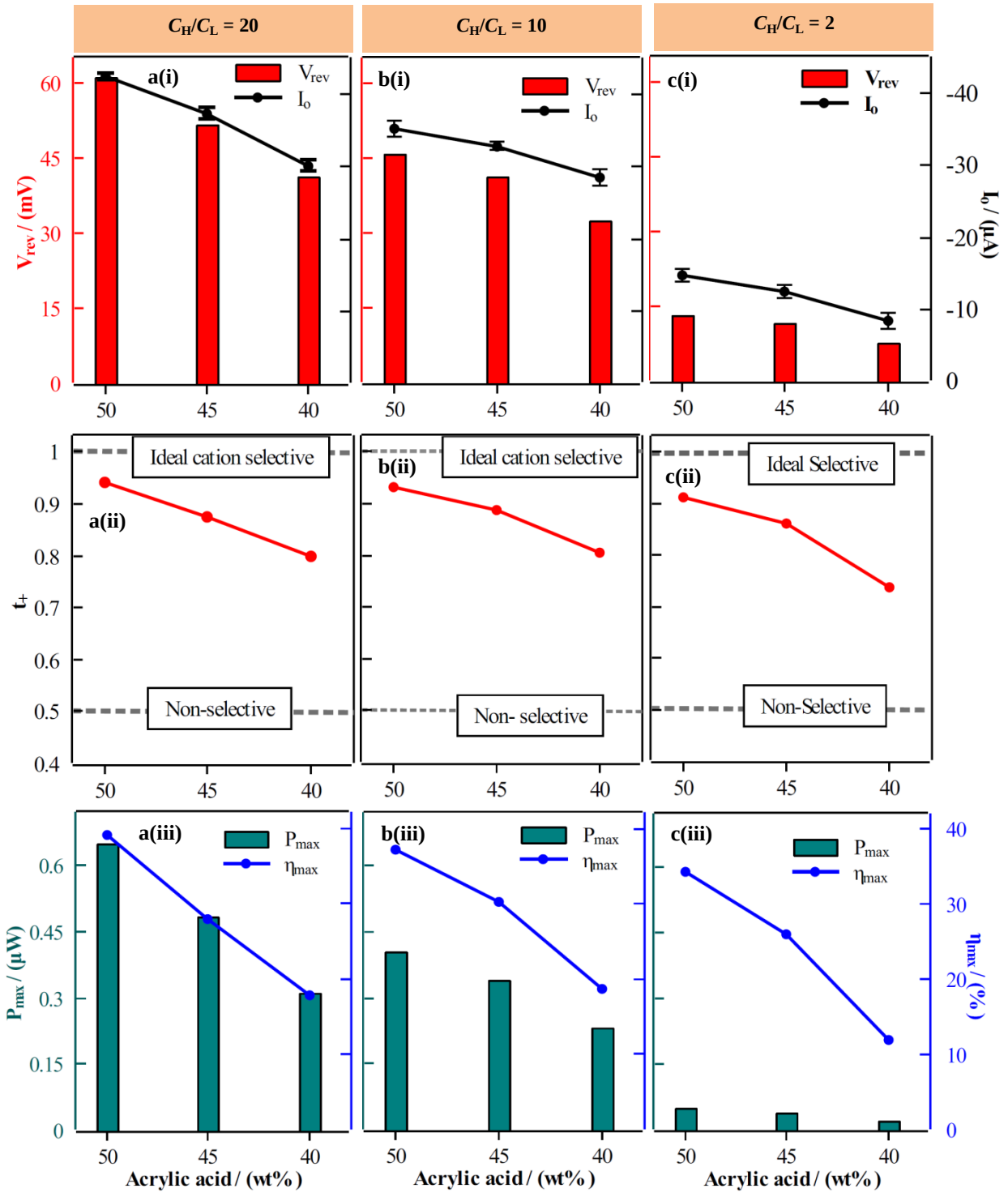

Figure 52: Effect of percentage content of Acrylic acid inside the HP membrane a(i) V_{rev} and I_o vs Arcylic acid wt% (C_H/C_L=20) a(ii) cation selectivity vs Arcylic acid wt% (C_H/C_L=20) a(iii) P_{max} and η_{max} vs Arcylic acid wt% (C_H/C_L=20) b(i) V_{rev} and I_o vs Arcylic acid wt% (C_H/C_L=10) b(ii) cation selectivity vs Arcylic acid wt% (C_H/C_L=10) b(iii) P_{max} and η_{max} vs Arcylic acid wt% (C_H/C_L=10) c(i) V_{rev} and I_o vs Arcylic acid wt% (C_H/C_L=2) c(ii) cation selectivity vs Arcylic acid wt% (C_H/C_L=2) c(iii) P_{max} and η_{max} vs Arcylic acid wt% (C_H/C_L=2).

4.4.5 Effect of pH

The performance of the HP membrane fabricated with 50wt % acrylic acid was tested in various pH mediums. The HP membrane was fixed between the two cells. The HP membrane was exposed to different concentration folds (concentration gradients).

Initially, the HP membrane was exposed to a medium with a pH value of 3. At a C_H/C_L ratio of 20, the V_{rev} and I_o values were 47.4 mV and -32.3 µA, respectively. The V_{rev} and I_o values obtained at pH 3 were moderately lower than those obtained at pH=5.5-6 (Figure 53a and b). Reducing the pH further to 1.5 had a drastic effect on the performance of the HP membrane. The data presented in Figure 53c indicates that the t_+ values obtained at pH 1.5 were close to 0.5, indicating a lack of preferentially cation transport across the membrane, which consequently resulted in a decrease of V_{rev}, I_o, P_{max} and η_{max} values. At pH=1.5, carboxylate ions became protonated, leading to a reduction effective charge of the membrane. The reduction in surface charge density eventually led to decreases in cation selectivity and consequently resulted in poor performance.

Theoretically, it is expected that the performance of the HP membrane should increase with an increase in pH value. However, the data exhibited by the HP membrane at pH 9 was similar to the data obtained at pH=5.5-6. Thus, it can be deduced that at both of the pH values (5.5-6 and pH=9), an approximately equal number of carboxylic acid groups were present in the deprotonated state.

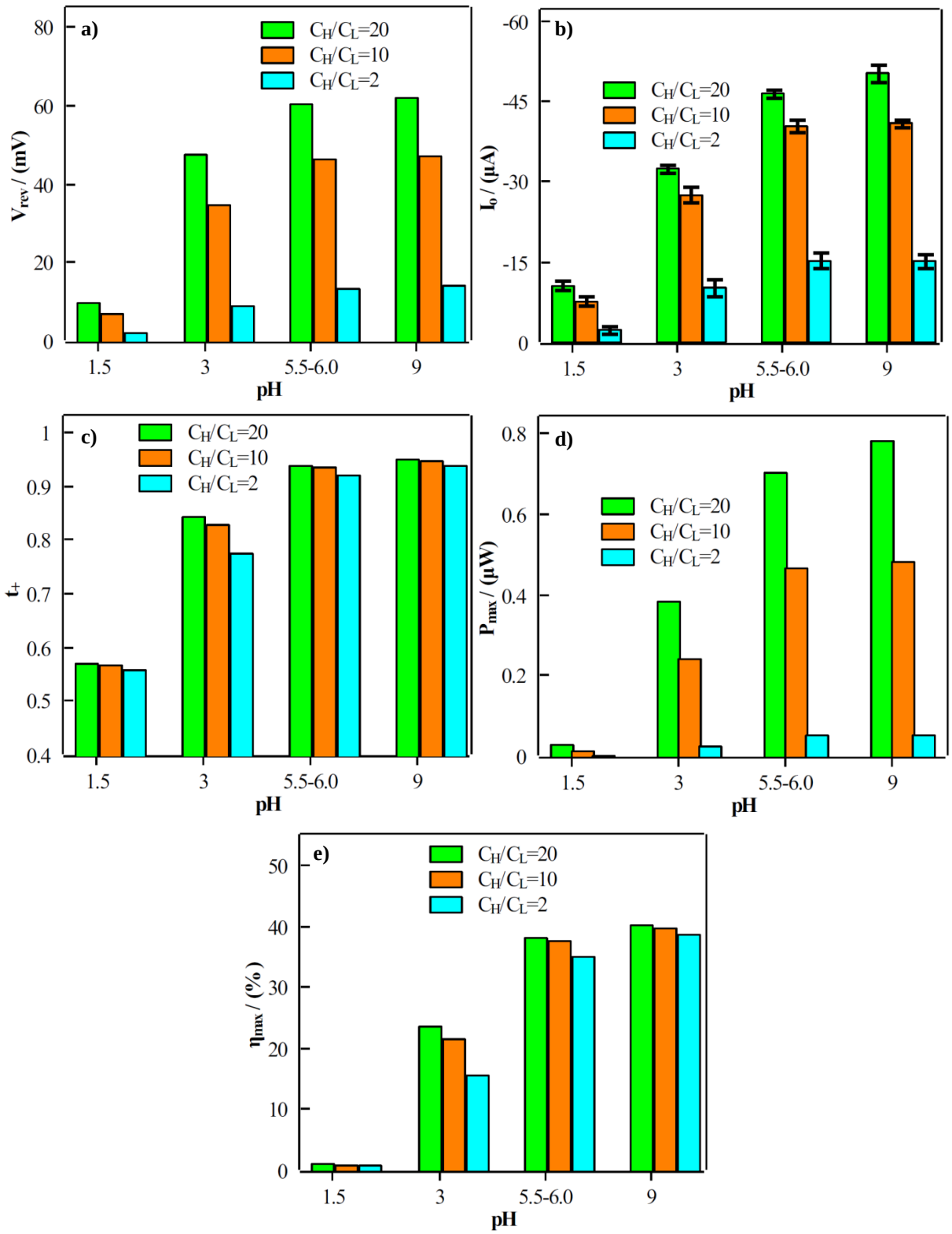

Figure 53: Effect of pH on the performance of the HP membrane (a) V_{rev} vs pH (b) I_o vs pH (c) t_+ vs pH (d) P_{max} vs pH (e) η_{max} vs pH.

4.4.6 Effect of multivalent cations

The study investigated the impact of a divalent cation on the performance of the HP membrane, which was prepared with 50 wt% acrylic acid. The membrane was initially exposed to an asymmetric KCl electrolyte solution with a C_H/C_L ratio of 20 (C_H = 1000 mM KCl | C_L = 50 mM KCl). The resulting values for V_{rev} and I_o were 61.3 mV and -47.40 µA, respectively. In the second case, the salt solution in the C_L compartment was substituted with 50 mM $CaCl_2$, resulting in a moderate impact on the HP membrane's performance. The values of I_o and V_{rev} obtained in the second case were -30.8 µA and 40 mV, respectively (Figure 54a). In the third case, the C_H compartment was filled with 1000 mM $CaCl_2$ while the C_L compartment was filled with 50 mM KCl. It was observed that the performance was negatively affected in the third case with significantly lower I_o and V_{rev} values (-16.9 µA and 24.8 mV) compared to the former cases.

In the final case, the C_L compartment was filled with 50 mM $CaCl_2$ while the C_H compartment was filled with 1000 mM $CaCl_2$. As a result, V_{rev} and I_o further decreased to 7.97 mV and -5.78 µA. Furthermore, a negligible value of P_{max} and a t_+ value of 0.61 were obtained (Figure 54b and c). The t_+ value close to 0.5 indicates that the membrane is non-selective towards cations. Ca^{2+} is the divalent cation with higher charge density compared to K^+, therefore the electrostatic interaction established between Ca^{2+} and carboxylate ions would be stronger compared to the interaction between K^+ and carboxylate ions. The result of the final case suggests that the net surface charges density of the membrane almost approached zero, which led to almost non-selective cation transport behaviour. Therefore, it can be concluded that the performance of the HP membrane deteriorates upon exposure to multivalent cations.

Following the investigation, the HP membrane was again tested with KCl, similar to the first case. The membrane was exposed to a concentrated gradient of 20. The performance of the HP membrane returned to normal, as shown in Figure 54d.

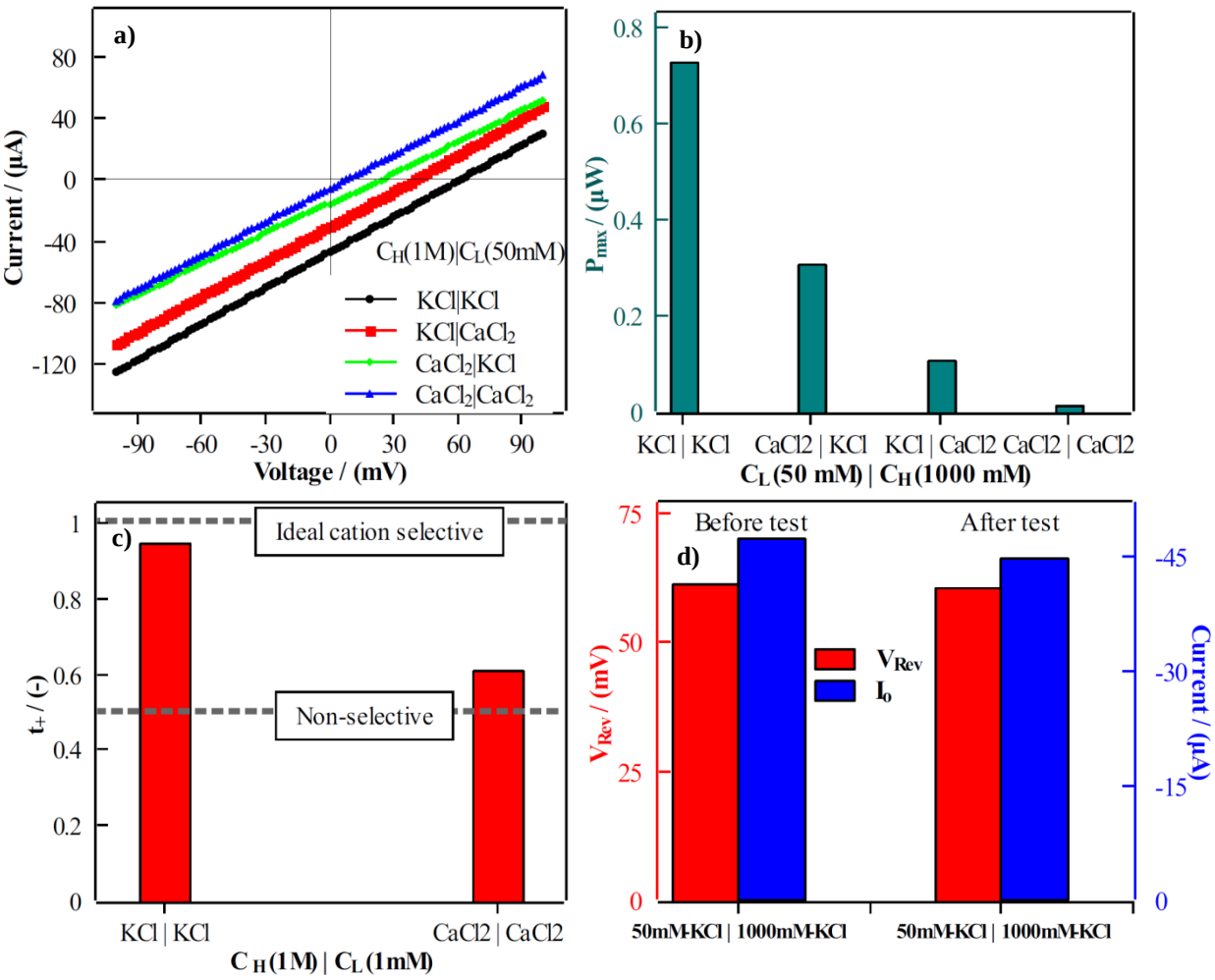

Figure 54: Effect of multivalent cation on the performance of HP membrane (a) *I-V* curves of different salt solution (b) P_{max} and η_{max} (c) t_+ (d) V_{rev} and I_o values before and after the investigation.

4.4.7 Time dependent performance

The study investigated time dependent performance of the HP membrane fabricated with 50 wt% acrylic acid. The HP membrane was exposed to a C_H/C_L ratio of 20 and the electrolyte solution was retained in the cells for five days. The results showed a significant reduction in V_{rev} values from 59.6 mV to 3.5 mV and a reduction in I_o values from -51.6 µA to -4.0 µA after five days (Figure 55a). Furthermore, the P_{max} value dropped down from 0.75 µW to 0.0035 µW, as shown in Figure 55b. It was observed that the water level constantly dropped with an insignificant rate in the C_L compartment and rose in the C_H compartment indicating the movement of water against the concentration gradient. The decrease in the C_H/C_L ratio with time resulted in a low cation flux down the concentration gradient, resulting in curtailment of performance.

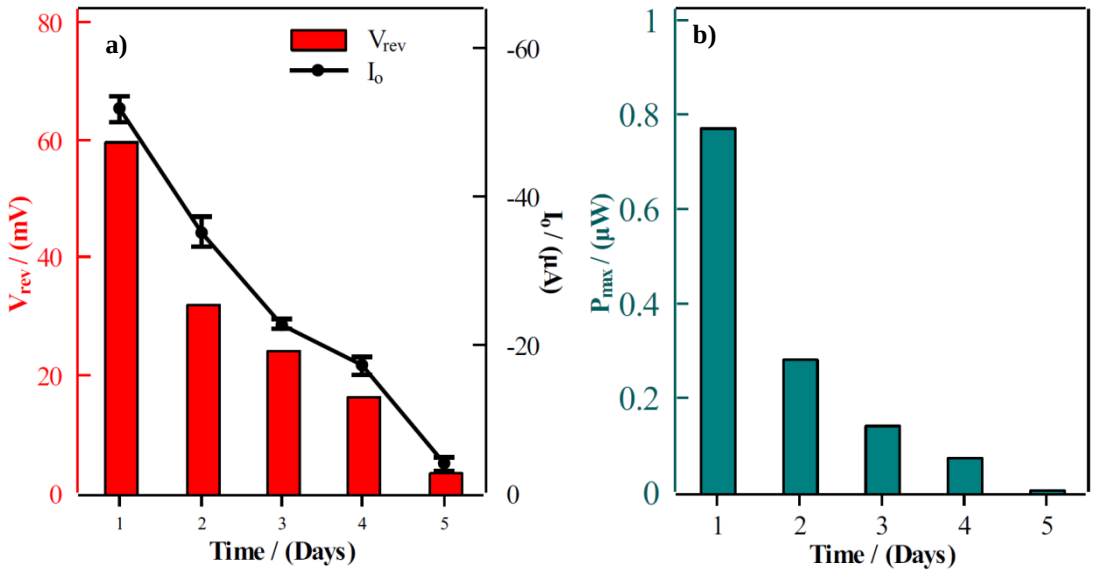

Figure 55: Time dependent investigation of HP membrane (a) V_{rev} and I_o vs time (b) P_{max} vs time.

After five days, the fresh KCl solutions were substituted with the old one and the *I-V* experiment was carried out. The *I-V* curve obtained from the fresh salt solution was compared with the *I-V* curve obtained on the first day (Figure 56). Both of the *I-V* curves had approximately similar V_{rev} and I_o values, indicating that the decrement in the performance over time was solely due to a decrease in the C_H/C_L ratio.

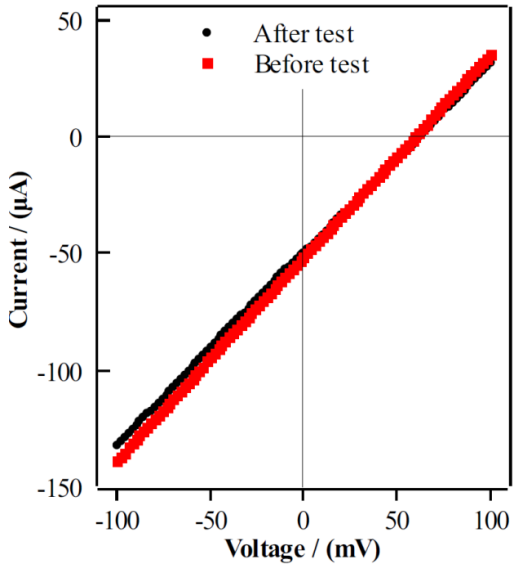

Figure 56: *I-V* graph obtained after and prior to time dependent investigation.

4.5 Conclusion

Subnano-sized pores were fabricated in the polyimide foil using the soft etching technique. The pore's surface has a net negative charge due to the presence of carboxylate ions. The PI membrane with a fluence of 4.0×10^9 pores/cm^2 exhibited the highest V_{rev} (123 mV), P_{max} (0.45 µW) and η_{max} (40%) values. The performance of the PI membrane declined beyond the fluence value of 4.0×10^9 pores/cm^2. At high fluence values, there is increased likelihood of pore overlap which, resulting in enlarged pore size and consequently degradation of the performance. The efficiency of the PI membrane was negatively affected when introduced to the acidic medium (pH=3). Multivalent cations have a strong electrostatic interaction with carboxylate ions, therefore introducing the membrane to multivalent cations led to reduction of the charge density and consequently resulted in a decline in the performance of the membrane. Exposing the PI membrane to asymmetrical $CaCl_2$ solution resulted in charge inversion.

The HP membrane was fabricated by incorporation of acrylic acid hydrogel within the pores of the PET support. The average pore size of the plain PET foil was between 180-260 nm. The HP membrane synthesised with 50 wt% acrylic acid exhibited the best performance in terms of power output (P_{max} = 1.10 µW). Increasing the percentage content of acrylic acid in the HP membrane resulted in higher charge density, leading to higher cation selectivity and superior performance. The performance of the membrane was moderately affected in the solution medium having a pH value of 3.0. Further reducing the pH value to 1.5 had a detrimental effect on the performance of the membrane. The exposure of the membrane to the divalent cation proved to be detrimental. It was due to the strong electrostatic interaction established between Ca^{2+} and carboxylate ions that led to the loss of surface charges and eventually resulted in decline of performance.

The test area of the PI and the HP membranes was approximately 100 mm^2. Table 1 presents a comparison of the different membranes used for osmotic energy harvesting. It can be observed that membranes with a smaller test area have high power density whereas membranes tested with a larger testing area have low power density. It was reported in previous literature, the power output increases non-linearly with an increase in testing area leading to a decrease in power density [123,124]. An increase in the test area leads to a surge of CP (concentration polarisation) resulting in the non-linear increase of current values. On the other hand, an upscaled osmotic energy set-up requires a bigger membrane's test area. Performance data obtained with an

experimental set-up with a small test area cannot be translated into an upscaled model since the interference of CP in the data is bypassed in the set-ups with small test areas.

Table 1: The comparison of power densities obtained with different membranes.

Membrane	**Thickness/μm**	**Test area/mm^2**	**Power density/ Wm^{-2}**	**C_H/C_L (Salt)**	**Reference**
Ionized wood membrane	∽1000	100	0.013	1000 (NaCl)	[125]
Soft etched polyimide membrane	**13**	**100**	**0.0045**	**100 (KCl)**	**This Work**
Track etched polycarbonate foil	20	78.6	0.058	1000 (KCl)	[22]
Hydrogel (acrylic acid-co-acrylamide-co-methacrylate) filled polycarbonate pore	25	0.03	4.08	50 (NaCl)	[126]
PET membrane modified with Cyt-C	23	0.03	0.86	50 (NaCl)	[127]
PET-arcylic acid based hydrogel composite membrane	**17-19**	**100**	**0.011**	**40 (KCl)**	**This Work**

In the chapter, two membranes were investigated: PI and HP membranes. So the big question remains as to which membrane is superior. The power output exhibited by the HP membrane was better compared to the PI. Additionally, the HP membrane outperformed the PI membrane in the acidic medium and when exposed to the multivalent cation. However, the PI membrane was more mechanically robust compared to the HP membrane. The PI membrane was cheap and easier to fabricate whereas the HP membrane was relatively difficult to fabricate. Additionally, the PI membrane was able to maintained P_{max} value over time compared to the HP membranes (Figure 47 and Figure 55). Therefore, superior membrane cannot be identified as both have their distinct advantages.

Chapter 5. Summary and Outlook

The thesis demonstrates the successful fabrication of a conical nanopore with the PET foil that was able to preferentially transport cation. The nanopore was fabricated using the asymmetric etching method. PET foil was introduced to 9M NaOH and the stopping solution, two electrodes were immersed inside the cells filled with the etchant and the stopping solution and the voltage bias of -1V was applied. The conical nanopore's surface acquires a negative charge due to carboxylate ions that originate after the etching process. The conical nanopore exhibited selectively transports cations in the presence of salt solution. The monovalent cation (K^+, Na^+ and Li^+) were not able to neutralise or invert the surface charge of the unmodified pore. However, exposure of the pore to the multivalent cation resulted in either charge inversion or charge neutralisation. The thesis demonstrated that Ca^{2+} led to charge neutralisation and La^{3+} caused the charged inversion. This outcome was due to the strong interactions between the multivalent cations and carboxylate ions leading to surface charge neutralisation or inversion.

In the current research, functionalisation of the nanopore's surface was achieved using electrostatic self-assembly of PAH. The modified PAH conical nanopores selectively transported anions. The surface charges of PAH-modified nanopore slightly inverted to positive when exposed to monovalent anions such as HCO_3^- and $H_2PO_4^-$. HPO_4^{2-} was able to invert the negative surface charges to a large extent.

A nanopore or sub-nanopore having a charged surface has various applications such as osmotic energy harvesting. Sub-nanometer PI membrane was fabricated using the soft etching technique. In the technique, the PI foil was immersed in DMF solution for at least 24 hours. Electrical power was generated when the membrane was exposed to a concentration gradient. The PI membrane exhibited the highest P_{max} (0.45 µW) when exposed to a C_H/C_L ratio of 100. The performance of the PI membrane declined beyond a critical value of fluence (4.0×10^9 pores/cm^2). In the thesis, it was demonstrated that the performance of the PI membrane deteriorated after being exposed to the multivalent cation. The membrane's exposure to the acidic medium also resulted in deterioration of performance. PI membranes with networked porous structure have demonstrated almost similar performance to the PI membranes with parallel porous structure.

The HP membrane was fabricated by incorporating acrylic acid hydrogel within the porous PET support, and the hydrogel was cured by UV irradiation. The HP membrane had negative surface

charges and preferentially transports cation. The membrane's exposure to a concentration gradient led to the generation of electrical current. The P_{max} value increased in proportion to an increase in the C_H/C_L ratio. However, experimental data demonstrated that the P_{max} and I_o values dropped beyond a certain C_H/C_L ratio. The decline in P_{max} and I_o values was mainly attributed to concentration polarisation. Additionally, the HP membrane's performance deteriorated in the acidic medium (pH=1.5) and when exposed to multivalent cations. The maximum value of P_{max} (1.1 μW) was obtained at a C_H/C_L ratio of 40.

The HP membrane demonstrated superior P_{max} performance when compared to the PI membrane and exhibited improved performance in the acidic medium. However, the PI membrane had better mechanical strength and was easy to fabricate. Therefore, it is difficult to declare a winner between the two membranes.

Regarding the future work, both the PI and HP membranes can be tested in the field of heavy metal ion filtration. Moreover, both membranes can be tested as cation selective membrane for the ED process.

In the thesis, the acrylic acid hydrogel was infused within the porous PET membrane. In subsequent research, vinyl phosphonic acid hydrogel can also be incorporated inside the porous PET membrane. The introduction of phosphonic groups can enhance the performance of the membrane. It is because the phosphonic acid group has a charge of -2, whereas carboxylic acid groups have a charge of -1. Therefore, incorporation of vinyl phosphonic hydrogel within a PET support membrane should exhibits superior cation selectivity and power output. The positively charged hydrogel can also be incorporated inside a porous polymer membrane and its performance can be compared with the negatively charged hydrogels.

References

[1] Ul Haque A, Aloke K. *Nanochannels for Nanofluidics: Fabrication Aspects. In: Bhushan, B. (eds) Encyclopedia of Nanotechnology*.; 2012. https://doi.org/10.1007/978-90-481-9751-4_422

[2] Li, M., Cao, Y., Xiong, Y. & Qing, G. Hierarchically engineered nanochannel systems with pore-in / on-pore structures. (2023).https:// doi.org/10.1038/s41427-022-00451-y

[3] William Stillwell. Membrane Transport. in *An Introduction to Biological Membranes* , 2016:423–451. https://doi.org/10.1016/B978-0-444-63772-7.00019-1

[4] Sharova, E. I. Protein transport in plant cells. *Russ. J. Plant Physiol.* **49**, 255–268 (2002). https://doi.org/10.1023/A:1014865910119

[5] Jiang, X., Wang, L., Liu, S., Li, F. & Liu, J. Bioinspired artificial nanochannels: Construction and application. *Mater. Chem. Front.* **5**, 1610–1631 (2021). https://doi.org/10.1039/D0QM00795A

[6] Majumder, P., Mallela, A. K. & Penmatsa, A. Transporters Through the Looking Glass: An Insight into the Mechanisms of Ion-Coupled Transport and Methods That Help Reveal Them. *J. Indian Inst. Sci.* **98**, 283–300 (2018). https://doi.org//10.1007/s41745-018-0081-5

[7] Wolfersberger, M. G. UNIPORTERS, SYMPORTERS AND ANTIPORTERS. **6**, 1–2 (2011). https://doi.org/10.1242/jeb.196.1.5

[8] Yue, S. & Gu, C. Nanopores fabricated by focused ion beam milling technology. *2007 7th IEEE Int. Conf. Nanotechnol. - IEEE-NANO 2007, Proc.* 628–631 (2007) https://doi.org//10.1109/NANO.2007.4601269.

[9] Kwok, H., Briggs, K. & Tabard-Cossa, V. Nanopore fabrication by controlled dielectric breakdown. *PLoS One* **9**, (2014). https://doi.org/10.1371/journal.pone.0092880

[10] Verschueren, D. V., Yang, W. & Dekker, C. Lithography-based fabrication of nanopore arrays in freestanding SiN and graphene membranes. *Nanotechnology* **29**, (2018). https://doi.org/10.1088/1361-6528/aaabce

[11] Siwy, Z. *et al.* Ion transport through asymmetric nanopores prepared by ion track etching. *Nucl. Instruments Methods Phys. Res. Sect. B Beam Interact. with Mater. Atoms* **208**, 143–148 (2003). https://doi.org/10.1016/S0168-583X(03)00884-X

[12] Fürjes, P. Controlled focused ion beam milling of composite solid state nanopore arrays for molecule sensing. *Micromachines* **10**, (2019). https://doi.org/ 10.3390/mi10110774

[13] Lo, C. J., Aref, T. & Bezryadin, A. Fabrication of symmetric sub-5 nm nanopores using focused ion and electron beams. *Nanotechnology* **17**, 3264–3267 (2006). https://doi.org/ 10.1088/0957-4484/17/13/031

[14] Chen, C. H., Chang, X. & Wu, C. S. A novel shaped-controlled fabrication of nanopore and its applications in quantum electronics. *Sci. Rep.* **9**, 1–7 (2019).https://doi.org/10.1038/s41598-019-55190-y

[15] Siwy, Z. & Fuliński, A. Fabrication of a Synthetic Nanopore Ion Pump. *Phys. Rev. Lett.* **89**, 4–7 (2002). https://doi.org/10.1103/PhysRevLett.89.198103

[16] Ali, M., Schiedt, B., Healy, K., Neumann, R. & Ensinger, W. Modifying the surface charge of single track-etched conical nanopores in polyimide. *Nanotechnology* **19**, (2008).https://doi.org/10.1088/0957-4484/19/8/085713

[17] Apel, P. Y., Ramirez, P., Blonskaya, I. V., Orelovitch, O. L. & Sartowska, B. A. Accurate characterization of single track-etched, conical nanopores. *Phys. Chem. Chem. Phys.* **16**, 15214–15223 (2014).https:// doi.org/ 10.1039/c4cp01686f

[18] Kaya, D. & Keçeci, K. Review—Track-Etched Nanoporous Polymer Membranes as Sensors: A Review. *J. Electrochem. Soc.* **167**, 037543 (2020).https:// doi.org/ 10.1149/1945-7111/ab67a7

[19]Shi, W., Friedman, A. K. & Baker, L. A. Nanopore Sensing. *Anal. Chem.* **89**, 157–188 (2017). https://doi.org/10.1021/acs.analchem.6b04260

[20] Sexton, L. T., Horne, L. P. & Martin, C. R. Developing synthetic conical nanopores for biosensing applications. *Mol. Biosyst.* **3**, 667–685 (2007). https:// doi.org:/ 10.1039/b708725j

[21] Guanabara, E., Ltda, K., Guanabara, E. & Ltda, K. Solid-State Nanopore Array: Manufacturing and Applications. *nano micro Small* **19**, (2023). https://doi.org/10.1002/smll.202205680

[22] Kilsung Kwon, Seung Jun Lee, Longnan Li, C. H. and D. K. Energy harvesting system using reverse electrodialysis with nanoporous polycarbonate track-etch membranes. *Arch. Thermodyn.* **33**, 23–40 (2012).https://doi.org/10.1002/er.3111

[23]Nasir, S., Ali, M., Ahmed, I., M. Niemeyer, C. & Ensinger, W. Phosphoprotein Detection with a Single Nanofluidic Diode Decorated with Zinc Chelates. *Chempluschem* **85**, 387–594 (2020). https://doi.org/10.1002/cplu.202000045

[24] Perera, F. Pollution from fossil-fuel combustion is the leading environmental threat to global pediatric health and equity: Solutions exist. *Int. J. Environ. Res. Public Health* **15**, (2018). https://doi.org/10.3390/ijerph15010016

[25] Mirza, M. M. Q. Climate change, flooding in South Asia and implications. *Reg. Environ. Chang.* **11**, 95–107 (2011). https://doi.org/ 10.1007/s10113-010-0184-7

[26] https://www.iea.org/reports/renewable-electricity

[27] Mohtasham, J. Review Article-Renewable Energies. *Energy Procedia* **74**, 1289–1297 (2015).https://doi.org/ 10.1016/j.egypro.2015.07.774

[28] Gielen, D. *et al.* The role of renewable energy in the global energy transformation. *Energy Strateg. Rev.* **24**, 38–50 (2019). https://doi.org/10.1016/j.esr.2019.01.006

[29] Elahi, H., Eugeni, M. & Gaudenzi, P. Energy Harvesting. in *Piezoelectric Aeroelastic Energy Harvesting* 41–59 (2022). https://doi.org/10.1016/B978-0-12-823968-1.00014-3.

[30] Hsu, W. S., Preet, A., Lin, T. Y. & Lin, T. E. Miniaturized salinity gradient energy harvesting devices. *Molecules* **26**, 1–16 (2021). https://doi.org/10.3390/molecules26185469

[31] Sugimoto, Y., Ujike, R., Higa, M., Kakihana, Y. & Higa, M. Power Generation Performance of Reverse Electrodialysis (RED) Using Various Ion Exchange Membranes and Power Output Prediction for a Large RED Stack. *Membranes (Basel).* **12**, (2022). https://doi.org/10.3390/membranes12111141

[32] Matsuyama, K. *et al.* Power generation system based on pressure retarded osmosis with a commercially-available hollow fiber PRO membrane module using seawater and freshwater. *Desalination* **499**, 114805 (2021). https://doi.org/10.3390/membranes12111141

[33] Froehlich, K. *et al.* Fabrication of soft-etched nanoporous polyimide membranes for ionic conduction and discrimination. *J. Memb. Sci.* **617**, 118633(2021). https://doi.org/10.1016/j.memsci.2020.118633

[34] Nasir, S. Stimuli-Triggered Ionic and Molecular Transport through Track-Etched Nanopores. (2014). https://tuprints.ulb.tu-darmstadt.de/id/eprint/4233

[35] Ali, M. Functionalization and Application of Ion Track-Etched Nanochannels in Polymer Membranes. (2009). https://tuprints.ulb.tu-darmstadt.de/id/eprint/1952

[36] Crawford, W. ., Desorbo, W. & JUN, H. S. . Enhancement of Track Etching rates in charged particle-irradiated Plastics by a photo-oxidation effect. *Nature* **220**, 1313–1314 (1968). https://doi.org/10.1038/2201313a0

[37] Wong, C. F. & Hoberg, P. A comparison of the effects of ultraviolet radiation on CR-39 and lexan plastics irradiated by alpha particles. *Nucl. Instruments Methods Phys. Res.* **203**, 443–449 (1982). https://doi.org/10.1016/0167-5087(82)90658-5

[38] Zhu, Z. *et al.* Role of UV light illumination and DMF soaking in production of PET ion track membranes. *Nucl. Instruments Methods Phys. Res. Sect. B Beam Interact. with Mater. Atoms* **217**, 449–456 (2004).https:// doi:10.1016/j.nimb.2003.11.011

[39] Ma, T., Janot, J.-M. & Balme, S. Track-Etched Nanopore/Membrane: From Fundamental to Applications. *Small Methods* **4**, (2020). https://doi.org/10.1002/smtd.202000366

[40] Nasir, S. *et al.* Ionic transport characteristics of negatively and positively charged conical nanopores in 1:1, 2:1, 3:1, 2:2, 1:2, and 1:3 electrolytes. *J. Colloid Interface Sci.* **553**, 639–646 (2019). https://doi.org/10.1016/j.jcis.2019.06.061

[41] Ghanim, E. H., Hussein, A., El-Samman, H. M. & Tretyakova, S. P. Etching Properties of Polyethyleneterephthalate (PET) Melinex-E Nuclear Track Detectors (NTDs). in *IX Radiation Physics & Protection Conference* (2008).

[42] Ali, M., Bayer, V., Schiedt, B., Neumann, R. & Ensinger, W. Fabrication and functionalization of single asymmetric nanochannels for electrostatic/hydrophobic association of protein molecules. *Nanotechnology* **19**, (2008).https:// doi.org/ 10.1088/0957-4484/19/48/485711

[43] Tagliazucchi, M., Azzaroni, O. & Szleifer, I. Responsive polymers end-tethered in solid-state nanochannels: When nanoconfinement really matters. *J. Am. Chem. Soc.* **132**, 12404–12411 (2010). https://doi.org/10.1021/ja104152g

[44] Laucirica, G. *et al.* Amine-Phosphate Specific Interactions within Nanochannels: Binding Behavior and Nanoconfinement Effects. *J. Phys. Chem. C* **123**, 28997–29007 (2019). https://doi.org/10.1021/acs.jpcc.9b07977

[45] Xiao, K. *et al.* A bio-inspired dumbbell-shaped nanochannel with a controllable structure and ionic rectification. *Nanoscale* **10**, 6850–6854 (2018). https://doi.org/10.1039/C8NR01191E

[46] Ali, M. *et al.* Single cigar-shaped nanopores functionalized with amphoteric amino acid chains: Experimental and theoretical characterization. *ACS Nano* **6**, 3631–3640 (2012). https://doi.org/10.1021/nn3010119

[47] Bohinc, K., Kralj-Iglič, V. & Iglič, A. Thickness of electrical double layer. Effect of ion size. *Electrochim. Acta* **46**, 3033–3040 (2001). https://doi.org/10.1016/S0013-4686(01)00525-4

[48] Du, H., Lin, X., Xu, Z. & Chu, D. *Electric double-layer transistors: a review of recent progress*. *Journal of Materials Science* vol. 50 (Springer US, 2015).https://doi.org/10.1007/s10853-015-9121-y

[49] Masurkar, N., Varma, S. & Mohana Reddy Arava, L. Supported and Suspended 2D Material-Based FET Biosensors. *Electrochem* **1**, 260–277 (2020). https://doi.org/10.3390/electrochem1030017

[50] Tagliazucchi, M. & Szleifer, I. *Chemically Modified Nanopores and Nanochannels*. *ELSEVIER* (2016). https://doi.org/10.1016/c2015-0-00413-0.

[51] Zhu, Z. Y., Duan, J. L., Maekawa, Y., Koshikawa, H. & Yoshida, M. Bulk and track etching of PET studied by spectrophotometer. *Radiat. Meas.* **38**, 255–261 (2004). https://doi.org/10.1016/j.radmeas.2003.12.032

[52] Chander, M., Kumar, R., Kumar, S., Kumar, N. & Chakarvarti, S. K. Ionic current rectification through pH-regulated nanopores. *Dig. J. Nanomater. Biostructures* **13**, 13–21 (2018). http://dx.doi.org/10.1016/ j.mattod.2014.10.020

[53] Tagliazucchi, M. & Szleifer, I. Transport mechanisms in nanopores and nanochannels: Can we mimic nature? *Mater. Today* **18**, 131–142 (2015). http://dx.doi.org/10.1016/ j.mattod.2014.10.020

[54] Adar, R. M., Safran, S. A., Diamant, H. & Andelman, D. Screening length for finite-size ions in concentrated electrolytes. *Phys. Rev. E* **100**, 42615 (2019).https://doi.org/10.1103/PhysRevE.100.042615

[55] Haider, M. H. A., Ali, M. & Ensinger, W. Anions effect on ion transport properties of polyelectrolyte modified single conical nanopores. *Chem. Phys. Lett.* **767**, (2021). https://doi.org/10.1016/j.cplett.2021.138349

[56] Siwy & S, Z. Ion-Current Rectification in Nanopores and Nanotubes with Broken Symmetry. *Adv. Fucntional Mater.* **16**, 735–746 (2006). https://doi.org/10.1002/adfm.200500471

[57] Kim, H., Choi, J. S. & Lee, S. Pressure retarded osmosis for energy production: Membrane materials and operating conditions. *Water Sci. Technol.* **65**, 1789–1794 (2012).https://doi.org/10.2166/wst.2012.025

[58] Skilhagen, S. E., Dugstad, J. E. & Aaberg, R. J. Osmotic power - power production based on the osmotic pressure difference between waters with varying salt gradients. *Desalination* **220**, 476–482 (2008).https://doi.org/10.1016/j.desal.2007.02.045

[59] Achilli, A. & Hickenbottom, K. L. Pressure retarded osmosis: Applications. in *Sustainable Energy from Salinity Gradients* 55–75 (Elsevier Ltd., 2016). https://doi.org/10.1016/B978-0-08-100312-1.00003-1.

[60] Othman, N. H., Kabay, N. & Guler, E. Principles of reverse electrodialysis and development of integrated-based system for power generation and water treatment: a review. *Rev. Chem. Eng.* **38**, 921–958 (2022). https://doi.org/10.1515/revce-2020-0070

[61] Laucirica, G. *et al.* Shape matters: Enhanced osmotic energy harvesting in bullet-shaped nanochannels. *Nano Energy* **71**, 1–8 (2020). https://doi.org/10.1016/j.nanoen.2020.104612

[62] Patel, S. K., Qin, M., Walker, W. S. & Elimelech, M. Energy Efficiency of Electro-Driven Brackish Water Desalination: Electrodialysis Significantly Outperforms Membrane Capacitive Deionization. *Environ. Sci. Technol.* **54**, 3663–3677 (2020). https://doi.org/10.1021/acs.est.9b07482

[63] Conte, R. *et al.* Hydrogel Nanocomposite Systems: Characterization and Application in Drug-Delivery Systems. in *Nanocarriers for Drug Delivery: Nanoscience and Nanotechnology in Drug Delivery* 319–349 (Elsevier Inc., 2018).https:// doi.org/10.1016/B978-0-12-814033-8.00010-2.

[64] Wang, W., Narain, R. & Zeng, H. Hydrogels. in *Polymer Science and Nanotechnology: Fundamentals and Applications* 203–244 (Elsevier Inc., 2020). https://doi.org/10.1016/B978-0-12-816806-6.00010-8.

[65] Ahmed, E. M. Hydrogel : Preparation , characterization , and applications : A review. *J. Adv. Res.* **6**, 105–121 (2015). http://dx.doi.org/10.1016/j.jare.2013.07.006

[66] Apel, P. Y., Korchev, Y. E., Siwy, Z., Spohr, R. & Yoshida, M. Diode-like single-ion track membrane prepared by electro-stopping. *Nucl. Instruments Methods Phys. Res. Sect. B Beam*

Interact. with Mater. Atoms **184**, 337–346 (2001). https://doi.org/10.1016/S0168-583X(01)00722-4

[67] Lim, L., Rosli, N., Ahmed, I., et al. Synthesis and Swelling Behavior of pH-Sensitive Semi-IPN Superabsorbent Hydrogels Based on Poly(acrylic acid) Reinforced with Cellulose Nanocrystals. *Nanomaterials.* **7** , 399 (2017). https://doi.org/10.3390/nano7110399

[68] Cheng, L. J. Electrokinetic ion transport in nanofluidics and membranes with applications in bioanalysis and beyond. *Biomicrofluidics* **12**, (2018). https://doi.org/10.1063/1.5022789

[69] Daiguji, H., Yang, P., Szeri, A. J. & Majumdar, A. Electrochemomechanical energy conversion in nanofluidic channels. *Nano Lett.* **4**, 2315–2321 (2004). https://doi.org/10.1021/nl0489945

[70] Kim, D. K., Duan, C., Chen, Y. F. & Majumdar, A. Power generation from concentration gradient by reverse electrodialysis in ion-selective nanochannels. *Microfluid. Nanofluidics* **9**, 1215–1224 (2010). https://doi.org/10.1007/s10404-010-0641-0

[71] Weerakoon-Ratnayake, K. M., O'Neil, C. E., Uba, F. I. & Soper, S. A. Thermoplastic nanofluidic devices for biomedical applications. *Lab Chip* **17**, 362–381 (2017). https://doi.org/10.1039/c6lc01173j

[72] Kshama, B., Jirage, J. C. & Hulteen, C. R. M. Nanotubule-Based Molecular-Filtration Membranes. *Sci. (80-.)* **278**, 655–658 (1997). https://doi.org/10.1126/science.278.5338.655

[73] Abgrall, P. & Nguyen, N. T. Nanofluidic devices and their applications. *Anal. Chem.* **80**, 2326–2341 (2008). https://doi.org/10.1021/ac702296u

[74] Duan, C., Wang, W. & Xie, Q. *Review article: Fabrication of nanofluidic devices*. *Biomicrofluidics* vol. 7 (2013). https://doi.org/10.1063/1.4794973

[75] Pérez-Mitta, G., Trautmann, C., Toimil-Molares, M. E. & Azzaroni, O. *Single Ion Track-Etched Nanochannels for Analytical Applications*. *Chemically Modified Nanopores and Nanochannels* (Elsevier Inc., 2017). https://doi.org/10.1016/B978-0-323-40182-1.00003-8

[76] Ali, M., Ramirez, P., Mafé, S., Neumann, R. & Ensinger, W. A pH-Tunable nanofluidic diode with a broad range of rectifying properties. *ACS Nano* **3**, 603–608 (2009). https://doi.org/10.1021/nn900039f

[77] Poroca, D. R., Pelis, R. M. & Chappe, V. M. ClC channels and transporters: Structure, physiological functions, and implications in human chloride channelopathies. *Front. Pharmacol.* **8**, 1–25 (2017). https://doi.org/10.3389/fphar.2017.00151

[78] Portulano, C., Paroder-Belenitsky, M. & Carrasco, N. The Na+/I- Symporter (NIS): Mechanism and medical impact. *Endocr. Rev.* **35**, 106–149 (2014). https://doi.org/10.1210/er.2012-1036

[79] Petkov, G. V. Ion Channels. *Pharmacology* 387–427 (2009) doi:10.1016/B978-0-12-369521-5.00016-6. https://doi.org/10.1016/B978-0-12-369521-5.00016-6

[80] Davis, J. T., Okunola, O. & Quesada, R. Recent advances in the transmembrane transport of anions. *Chem. Soc. Rev.* **39**, 3843–3862 (2010). https://doi.org/10.1039/B926164H

[81] Günther, W., Lüchow, A., Cluzeaud, F., Vandewalle, A. & Jentsch, T. J. CIC-5, the chloride channel mutated in Dent's disease, colocalizes with the proton pump in endocytotically active kidney cells. *Proc. Natl. Acad. Sci. U. S. A.* **95**, 8075–8080 (1998). https://doi.org/10.1073/pnas.95.14.8075

[82] Mizusawa, Y. & Wilde, A. A. M. Brugada syndrome. *Circ. Arrhythmia Electrophysiol.* **5**, 606–616 (2012). https://doi.org/ 10.1161/CIRCEP.111.964577

[83] De La Escosura-Muñiz, A. & Merkoçi, A. Nanochannels preparation and application in biosensing. *ACS Nano* **6**, 7556–7583 (2012). https://doi.org/10.1021/nn301368z

[84] Ali, M. *et al.* Metal ion affinity-based biomolecular recognition and conjugation inside synthetic polymer nanopores modified with iron-terpyridine complexes. *J. Am. Chem. Soc.* **133**, 17307–17314 (2011). https://doi.org/10.1021/ja205042t

[85] Li, D. Nanochannel Fabrication. *Encycl. Microfluid. Nanofluidics* 1–8 (2013). https://doi.org/ 10.1007/978-3-642-27758-0

[86] Schiedt, B. CHARACTERIZATION AND APPLICATION OF ION TRACK-ETCHED NANOPORES. (2007) page#11. https://doi.org/10.11588/heidok.00007426

[87] Siwy, Z. *et al.* Rectification and voltage gating of ion currents in a nanofabricated pore. *Europhys. Lett.* **60**, 349–355 (2002). https://doi.org/10.1209/epl/i2002-00271-3

[88] Laucirica, G., Marmisollé, W. A. & Azzaroni, O. Dangerous liaisons: Anion-induced protonation in phosphate-polyamine interactions and their implications for the charge states of biologically relevant surfaces. *Phys. Chem. Chem. Phys.* **19**, 8612–8620 (2017). https://doi.org/ 10.1039/C6CP08793K

[89] Kioussis, D. R., Smith, D. F. & Kofinas, P. Ammonium perchlorate-binding poly(allylamine hydrochloride) hydrogels for wastewater remediation. *J. Appl. Polym. Sci.* **80**, 2073–2083 (2001). https://doi.org/10.1002/app.130

[90] Haynes, W. M. *CRC Handbook of Chemistry and Physics*. vol. 96 (1996).

[91] Hyde, A. M. *et al.* General Principles and Strategies for Salting-Out Informed by the Hofmeister Series. *Org. Process Res. Dev.* **21**, 1355–1370 (2017). https://doi.org/10.1021/acs.oprd.7b00197

[92] Mazzini, V. & Craig, V. S. J. What is the fundamental ion-specific series for anions and cations? Ion specificity in standard partial molar volumes of electrolytes and electrostriction in water and non-aqueous solvents. *Chem. Sci.* **8**, 7052–7065 (2017). https://doi.org/10.1039/c7sc02691a

[93] Shibata, A. *et al.* Photocurrent of purple membrane adsorbed onto a thin polymer film: Effects of monovalent and divalent ions. *Stud. Surf. Sci. Catal.* **132**, 635–638 (2001).https://

doi.org/ 10.1016/S0927-7765(01)00272-7

[94] Avtar, R., Tripathi, S., Aggarwal, A. K. & Kumar, P. Population-urbanization-energy nexus: A review. *Resources* **8**, (2019). https://doi:10.3390/resources8030136

[95] Heede, R. & Oreskes, N. Potential emissions of CO2 and methane from proved reserves of fossil fuels: An alternative analysis. *Glob. Environ. Chang.* **36**, 12–20 (2016). https://doi.org/10.1016/j.gloenvcha.2015.10.005

[96] Panwar, N. L., Kaushik, S. C. & Kothari, S. Role of renewable energy sources in environmental protection: A review. *Renew. Sustain. Energy Rev.* **15**, 1513–1524 (2011). https://doi.org/10.1016/j.rser.2010.11.037

[97] Perera, F. Pollution from fossil-fuel combustion is the leading environmental threat to global pediatric health and equity: Solutions exist. *Int. J. Environ. Res. Public Health* **15**, (2018). https://doi.org/10.3390/ijerph15010016

[98] Anderson, T. R., Hawkins, E. & Jones, P. D. CO2, the greenhouse effect and global warming: from the pioneering work of Arrhenius and Callendar to today's Earth System Models. *Endeavour* **40**, 178–187 (2016). https://doi.org/10.1016/j.endeavour.2016.07.002

[99] Wheatley, S., Sovacool, B. K. & Sornette, D. Reassessing the safety of nuclear power. *Energy Res. Soc. Sci.* **15**, 96–100 (2016). https://doi.org/10.1016/j.erss.2015.12.026

[100] Páez-Montoro, A.; García-Valderas, M.; Olías-Ruíz, E.; López-Ongil, C. Solar Energy Harvesting to Improve Capabilities of Wearable Devices. *sensors* **22**, 3950 (2022). https://doi.org/10.3390/s22103950

[101] Oliveira, P. F. G., Martins, N. M. C., Fontes, P. & Covas, D. Hydroenergy harvesting assessment: The case study of alviela river. *Water (Switzerland)* **13**, 1–12 (2021). https://doi.org/10.3390/w13131764

[102] Desalegn, B., Gebeyehu, D., Tamrat, B. & Tadiwose, T. Wind energy-harvesting technologies and recent research progresses in wind farm control models. *Front. Energy Res.* **11**, 1–21 (2023). https:// doi.org/ 10.3389/fenrg.2023.1124203

[103] Sentchev, A., Thiébot, J., Bennis, A. C. & Piggott, M. New insights on tidal dynamics and tidal energy harvesting in the Alderney Race: Tidal dynamics in the Alderney Race. *Philos. Trans. R. Soc. A Math. Phys. Eng. Sci.* **378**, 1–4 (2020). http://dx.doi.org/10.1098/rsta.2019.0490

[104] Heubner, C., Liebmann, T., Schneider, M. & Michaelis, A. Intercalation electrochemistry for thermoelectric energy harvesting from temperature fluctuations. *Chem. Commun.* **58**, 1203–1206 (2022).https://doi.org/ 10.1039/d1cc06121f

[105] Gunathilaka, G. & Randeniya, D. I. B. Energy harvesting from pressure forces. *2013 IEEE 8th Int. Conf. Ind. Inf. Syst. ICIIS 2013 - Conf. Proc.* 465–470 (2013). https://doi.org/10.1109/ICIInfS.2013.6732029

[106] Zhang, Y., Huang, Z., He, Y. & Miao, X. Enhancing the efficiency of energy harvesting

from salt gradient with ion-selective nanochannel. *Nanotechnology* **30**, (2019). https://doi.org/10.1088/1361-6528/ab0ed8

[107] Ma, T., Balanzat, E., Janot, J. M. & Balme, S. Nanopore Functionalized by Highly Charged Hydrogels for Osmotic Energy Harvesting. *ACS Appl. Mater. Interfaces* **11**, 12578–12585 (2019). https://doi.org/10.1021/acsami.9b01768

[108] Schaetzle, O. & Buisman, C. J. N. Salinity Gradient Energy: Current State and New Trends. *Engineering* **1**, 164–166 (2015). https://doi.org/10.15302/J-ENG-2015046.

[109] Kilsung, K., Seung Jun, L., Longnan, L., Changheon, H. & Daejoong, K. Energy harvesting system using reverse electrodialysiswith nanoporous polycarbonate track-etch membranes. *Int. J. ENERGY Res.* **38**, 530–537 (2014). https://doi.org/10.1002/er.3111

[110] Hong, J. G. *et al.* Potential ion exchange membranes and system performance in reverse electrodialysis for power generation: A review. *J. Memb. Sci.* **486**, 71–88 (2015). https://doi.org/10.1016/j.memsci.2015.02.039

[111] Sude, M., Wanga, Y., Chun, L., Xuaand, Q. & Zhonghua, M. Preparation and characterization ofnanoporous polyimide membrane by thetemplate method as low-kdielectric material. *Polym. Adv. Technol.* **27**, 414–418 (2015). https://doi.org/10.1002/pat.3686

[112] Siwy, Z., Dobrev, D., Neumann, R., Trautmann, C. & Voss, K. Electro-responsive asymmetric nanopores in polyimide with stable ion-current signal. *Appl. Phys. A Mater. Sci. Process.* **76**, 781–785 (2003). https://doi.org/10.1007/s00339-002-1982-7

[113] Ali, M. *et al.* Ionic circuitry with nanofluidic diodes. *Soft Matter* **15**, 9682–9689 (2019). https://doi.org/10.1039/C9SM01654F

[114] Qi, W. *et al.* Highly Selective Ionic Transport through Subnanometer Pores in Polymer Films. *Adv. Funct. Mater.* **26**, 5796–5803 (2016). https://doi.org/10.1002/adfm.201601689

[115] Darban, Z., Shahabuddin, S., Gaur, R., Ahmad, I. & Sridewi, N. *Hydrogel-Based Adsorbent Material for the Effective Removal of Heavy Metals from Wastewater: A Comprehensive Review*. *Gels* vol. 8 (2022). https://doi.org/10.3390/gels8050263

[116] Tassanapukdee, Y., Prayongpan, P. & Songsrirote, K. Removal of heavy metal ions from an aqueous solution by CS/PVA/PVP composite hydrogel synthesized using microwaved-assisted irradiation. *Environ. Technol. Innov.* **24**, (2021). https://doi.org/10.1016/j.eti.2021.101898

[117] Chen, W. *et al.* Improved Ion Transport in Hydrogel-Based Nanofluidics for Osmotic Energy Conversion. *ACS Cent. Sci.* **6**, 2097–2104 (2020). https://dx.doi.org/10.1021/acscentsci.0c01054

[118] Chai, Q., Jiao, Y. & Yu, X. Hydrogels for biomedical applications: Their characteristics and the mechanisms behind them. *Gels* **3**, (2017).https://doi.org/ 10.3390/gels3010006

[119] Thakar, H. *et al.* Biomolecule-Conjugated Macroporous Hydrogels for Biomedical Applications. *ACS Biomater. Sci. Eng.* **5**, 6320–6341 (2019). https://doi.org/ 10.1021/acsbiomaterials.9b00778

[120] Li, J., Liu, H., Wang, C. & Huang, G. A facile method to fabricate hybrid hydrogels with mechanical toughness using a novel multifunctional cross-linker. *RSC Adv.* **7**, 35311–35319 (2017).https://doi.org/ 10.1039/c7ra05645a

[121] Mei, Y. & Tang, C. Y. Recent developments and future perspectives of reverse electrodialysis technology: A review. *Desalination* **425**, 156–174 (2018). http://dx.doi.org/10.1016/j.desal.2017.10.021

[122] Hwang, J., Kataoka, S., Endo, A. & Daiguji, H. Enhanced energy harvesting by concentration gradient-driven ion transport in SBA-15 mesoporous silica thin films. *Lab Chip* **16**, 3824–3832 (2016).https://doi.org/10.1039/c6lc00844e

[123] Laucirica, G., Toimil-Molares, M. E., Trautmann, C., Marmisollé, W. & Azzaroni, O. Nanofluidic osmotic power generators - advanced nanoporous membranes and nanochannels for blue energy harvesting. *Chem. Sci.* **12**, 12874–12910 (2021).https://doi.org/ 10.1039/d1sc03581a

[124] Tong, X., Liu, S., Crittenden, J. & Chen, Y. Nanofluidic Membranes to Address the Challenges of Salinity Gradient Power Harvesting. *ACS Nano* **15**, 5838–5860 (2021). https://doi.org/10.1021/acsnano.0c09513

[125] Wu, Q.-Y. *et al.* Salinity-Gradient Power Generation with Ionized Wood Membranes. *Adv. Energy Mater.* **10**, (2020). https://doi.org/10.1002/aenm.201902590

[126] Chen, W. *et al.* Improved Ion Transport in Hydrogel-Based Nanofluidics for Osmotic Energy Conversion. *ACS Cent. Sci.* **6**, 2097–2104 (2020). https://dx.doi.org/10.1021/acscentsci.0c01054

[127] Fu, L., Jiang, J., Lu, B., Xu, Y. & Zhai, J. Using Smart Nanochannels as a Power Switch in Salinity Gradient Batteries. *ChemNanoMat* **5**, 1182–1187 (2019). http://dx.doi.org/10.1002/cnma.201900326

Publications

1. Nasir, S., Ali, M., Cervera, J., Gomez,V., **Haider, M. H. A.**, Ensinger, W., Mafe, S. & Ramirez, P. Ionic transport characteristics of negatively and positively charged conical nanopores in 1:1, 2:1, 3:1, 2:2, 1:2, and 1:3 electrolytes. *J. Colloid Interface Sci.* **553**, 639-646 (2019). https://doi.org/10.1016/j.jcis.2019.06.061

2. **Haider, M. H. A.**, Ali, M. & Ensinger, W. Anions effect on ion transport properties of polyelectrolyte modified single conical nanopores. *Chem. Phys. Lett.* **767**, (2021). https://doi.org/10.1016/j.cplett.2021.138349

3. **Haider, M. H. A.**, Nasir, S., Ali, M., Ramirez, P., Cervera, J., Mafe, S. & Ensinger, W. Osmotic energy harvesting with soft-etched nanoporous polyimide membranes. *Mater. Today Energy* **23**, (2022). https://doi.org/10.1016/j.mtener.2021.100909

List of Figure

List of Tables

List of Abbreviation

AA: Acrylic Acid

C_H: High concentrated salt solution

C_L: High concentrated salt solution

NPS: Networked Porous structure

DMF: Dimethyl Formamide

ED: Electrodialysis

FTIR: Fourier Transform Infrared

HP: Hydrogel-PET

I_o: Zero-voltage current

I-V: Current- voltage

NC: Normalised current

NRF: Normalised rectification factor

PAH: Polyallyamine hydrochloride

PC: Polycarbonate

PET: Polyethylene terephthlate

PI: Polyimide

P_{max}: Maximum Power

PPN: Parallel Porous network

PRO: Pressure retarded osmosis

RED: Reverse Electrodialysis

RF: Rectification Factor

RF/RF_o: Normalised Rectification Factor

SGE: Salinity gradient energy

SHI: Swift heavy ions

t_+: Cation transference number

UV: Ultraviolet

VARED: Voltage assisted reverse electrodialysis

V_{rev}: Reversal Voltage

η_{max}: maximum efficiency

Appendix

Table S 1: The table showing the conductivity of salts and ions at infinite dissolution [90].

Salt and ions	**Conductivity x 10^{-4} (m^2S/mol)**
NaCl	126.39
$NaNO_3$	121.51
$NaBrO_3$	105.78
$NaHCO_3$	95.30
NaH_2PO_4	86.08
Na_2SO_4	260.16
Na_2HPO_4	214.16
$Na_3C_6H_5O_7$	363.00
K^+	73.48
Na^+	50.08
Li^+	38.66

The table was also published in the following journal article
"**Anions effect on ion transport properties of polyelectrolyte modified single conical nanopores**" || ***M. H.A. Haider***, *M. Ali, W. Ensinger* || https://doi.org/10.1016/j.cplett.2021.138349

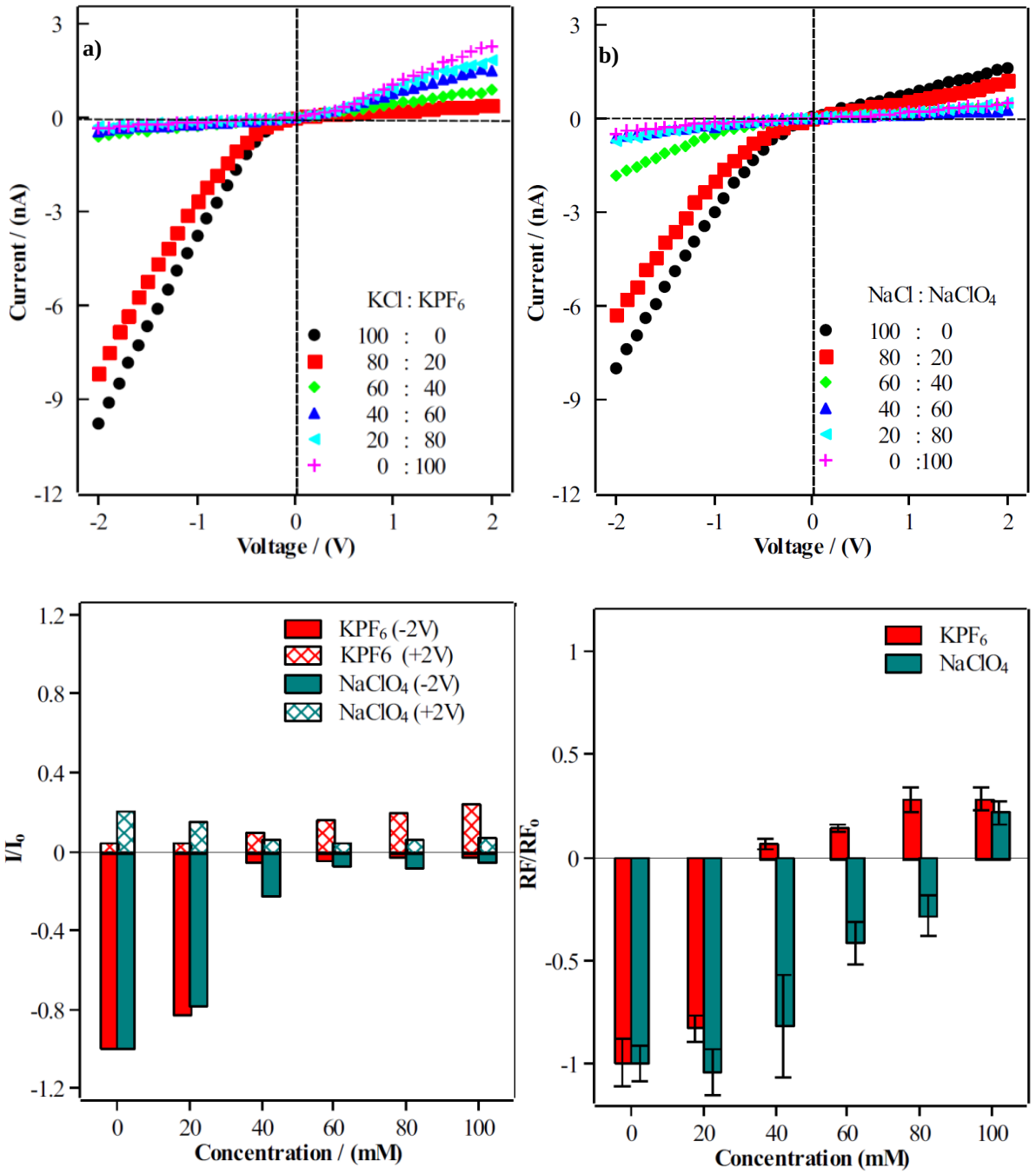

Figure S 1: Investigation of transportation behaviour of KPF_6 and $NaClO_4$ inside a PAH-modified nanopore. The total concentration of anions in each salt solution was maintained at 100mM. *I-V* curves were obtained for different concentration of (a) KPF_6 (b) $NaClO_4$ (c) Normalised current values were obtained for different concentration of KPF_6 and $NaClO_4$ (d) Normalised rectification factors were obtained for different concentration of KPF_6 and $NaClO_4$.

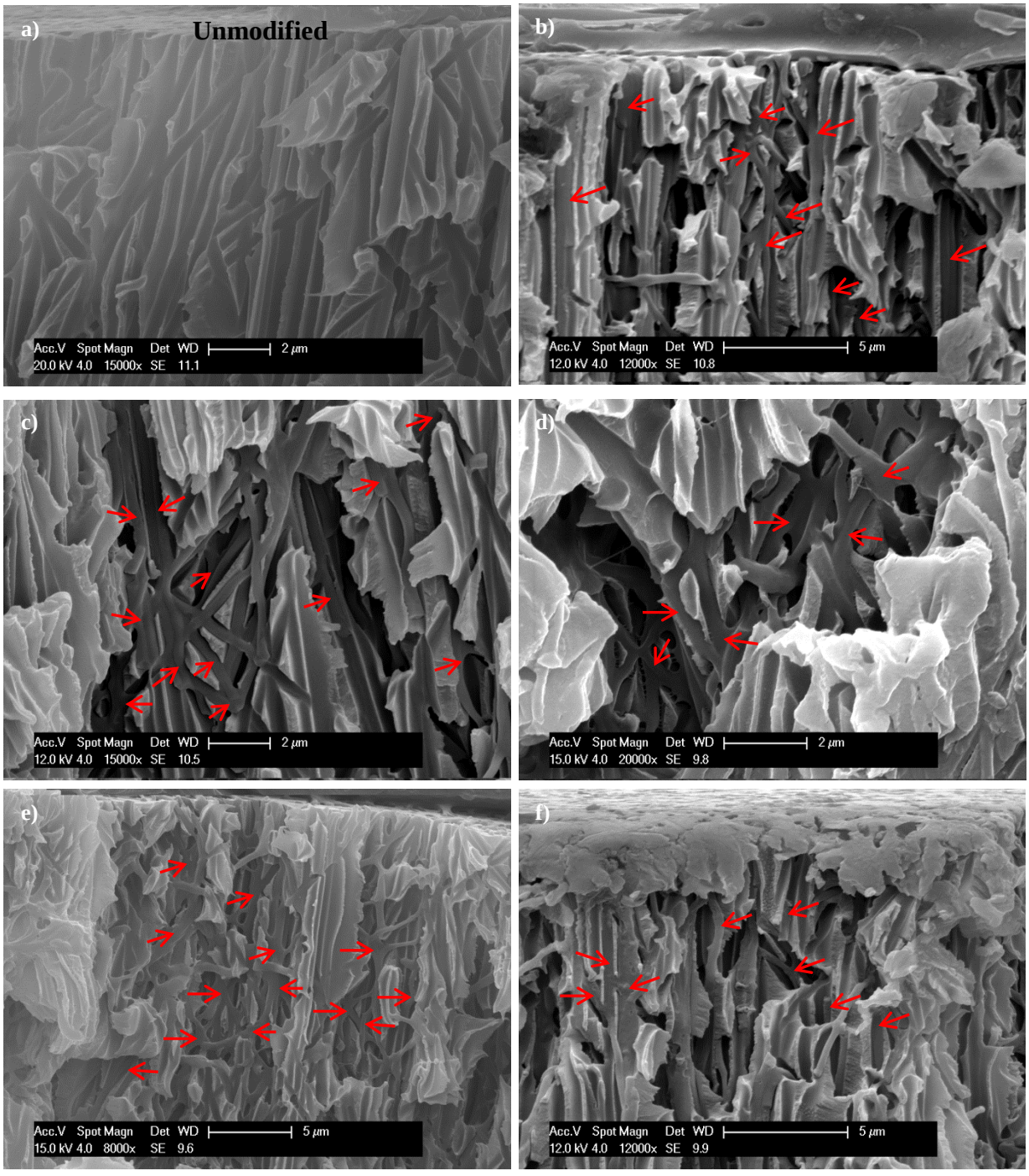

Figure S 2: SEM images of (a) Cross-section of un-modified porous cross networked Polycarbonate foil (b-f) Cross-section of hydrogel rods inside porous polycarbonate membrane.

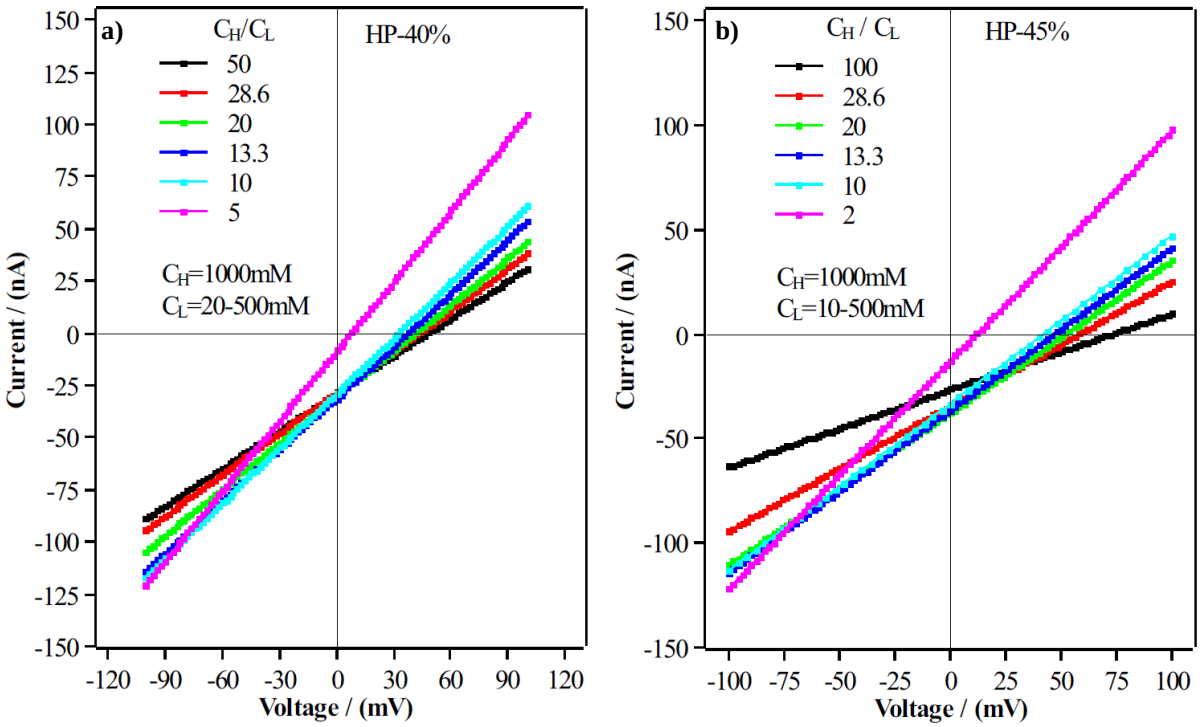

Figure S 3: *I-V* curves at different C_H /C_L ratios (a) HP membrane fabricated using 40 wt% Acrylic acid (b) HP membrane fabricated using 45 wt% acrylic acid.

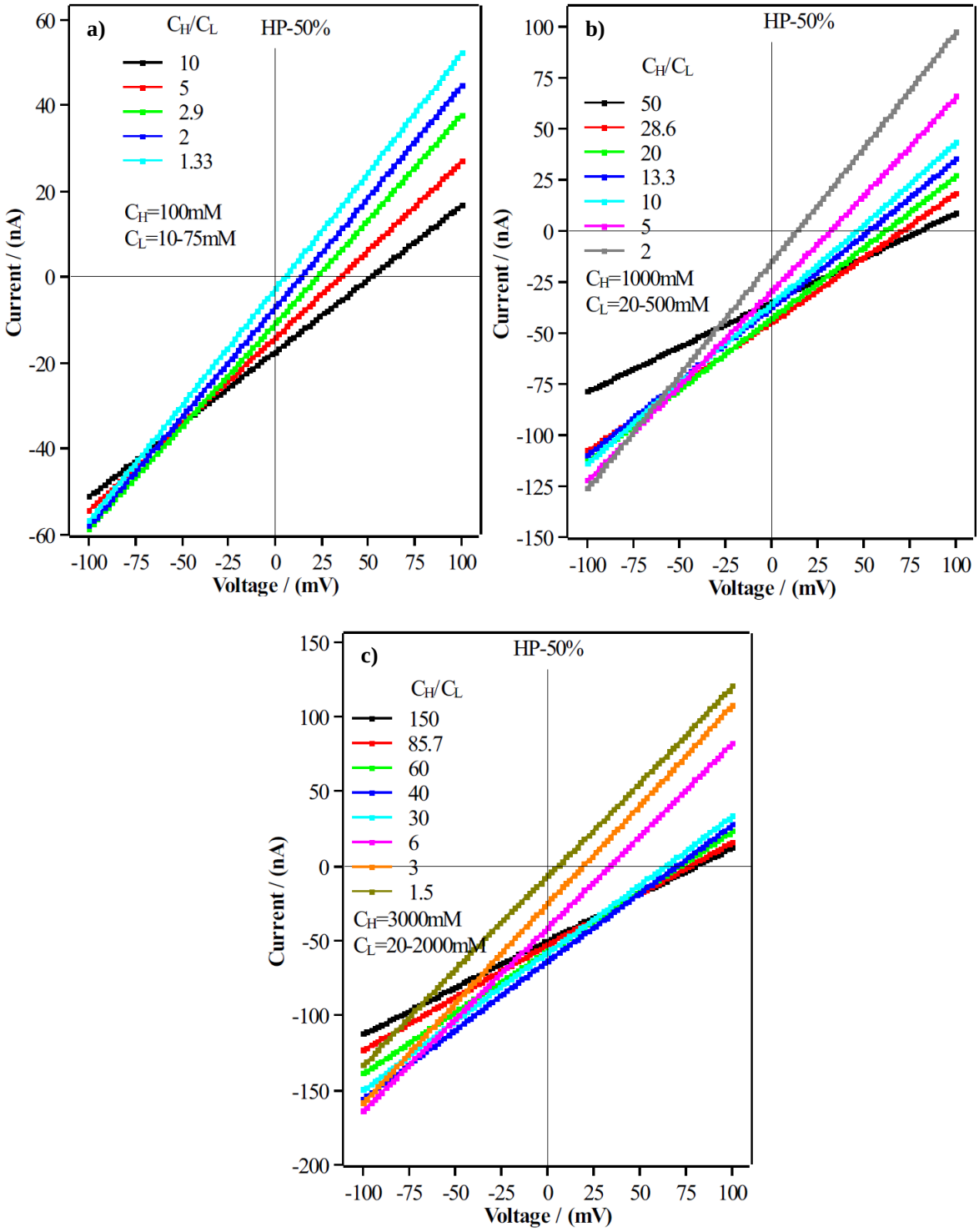

Figure S 4: (a-c) *I-V* curves at different C_H /C_L ratio. The membranes used in the investigation were fabricated using 50 wt% acrylic acid.

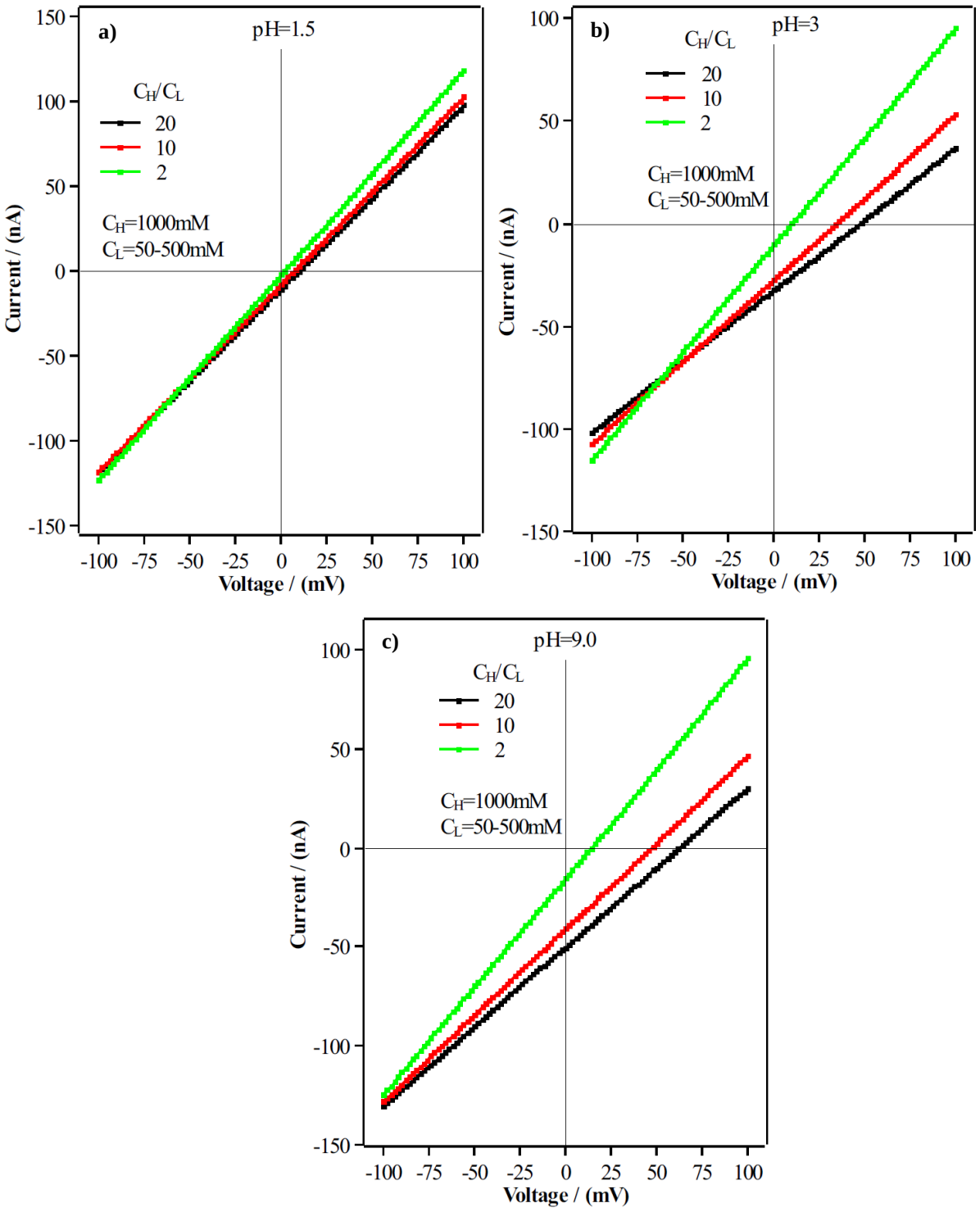

Figure S 5: *I-V* curves obtained at different pH medium. The HP membrane used in the investigation was fabricated using 50 wt% Acrylic acid (a) 1.5 (b) 3 (c) 9.

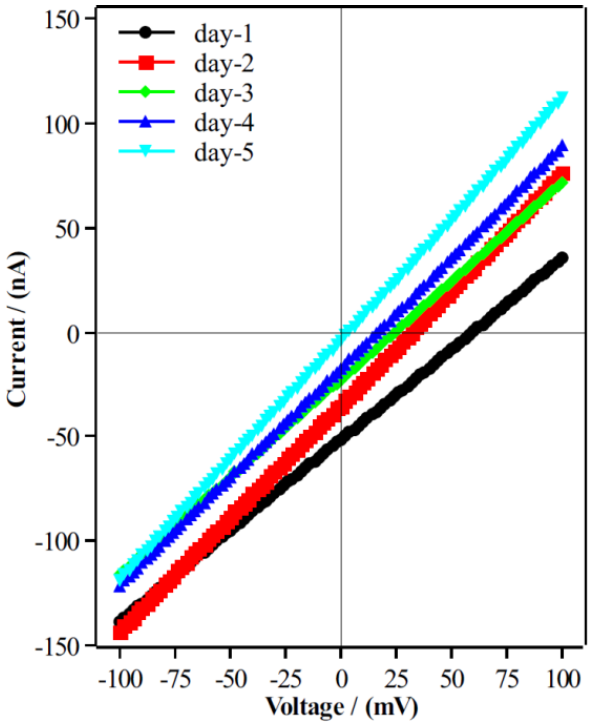

Fig S 6: Time dependent investigation of HP membrane.

Procedure to calculate % conversion of hydrogel

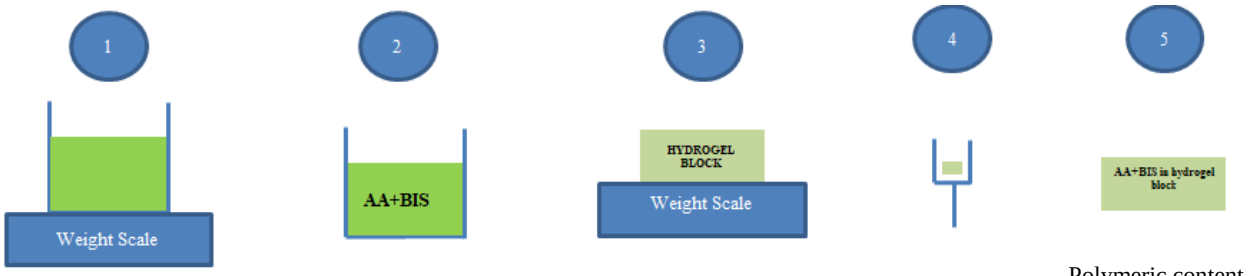

Weighing hydrogel solution

Polymeric content in hydrogel solution

Weighing hydrogel block

TGA

Polymeric content in hydrogel block

TGA: Thermogravimetric analysis

$$\% \text{ Conversion} = \frac{\text{Amount of AA+BIS+irgacure 2959 in hydrogel block}}{\text{Amount of AA+BIS+irgacure 2959 in hydrogel solution}}$$

Table S 2: Name and composition of acrylic acid hydrogel solution used in the research work.

Hydrogel solution	Acrylic acid concentration (wt%)	BIS concentration (wt%)	Irgacure 2959 (wt%)	Water (wt%)
Hy-30%	30	3	0.3	66.7
Hy-40%	40	3	0.3	56.7
Hy-45%	45	3	0.3	51.7
Hy-50%	50	3	0.3	46.7

Note: The hydrogel solution later cured with UV in order to synthesise the hydrogel.

% hydrogel conversion in Hy-50% hydrogel block

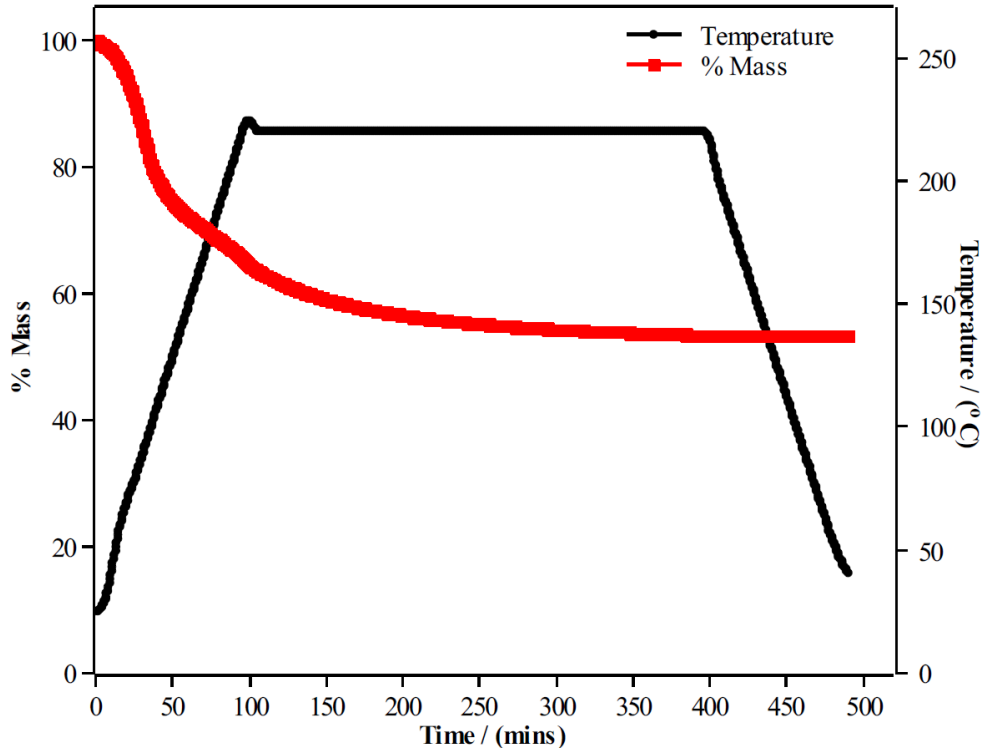

Figure S 7: TGA analysis of Acrylic acid hydrogel block prepared by using Hy-50% hydrogel solution

Table S 3: Hy-50% hydrogel block.

Mass of hydrogel solution /(g)	Mass of hydrogel block /(g)	Mass of AA+BIS+irgacure in hydrogel solution /(g)	% Residual mass in TGA	Mass of AA+BIS+irgacure in hydrogel block /(g)	Maximum Percentage conversion/ (%)	Minimum Percentage conversion/ (%)
10	8.25	5.33	53.3	4.40	79.6%	76.3%

Maximum percentage conversion: Calculation was made under the assumption that **all of the** BIS+irgacure have reacted.

Minimum percentage conversion: Calculation was made under the assumption that **none of the** BIS+irgacure have reacted.

% hydrogel conversion in Hy-45% hydrogel block

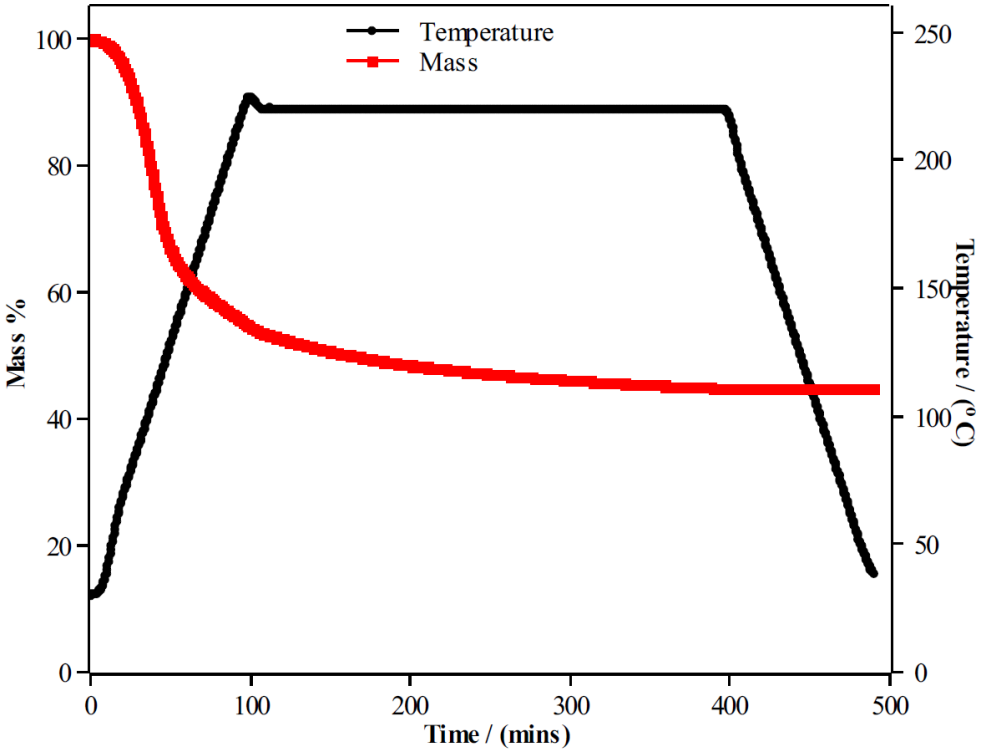

Figure S 8: TGA analysis of the Hy-45% hydrogel block that was prepared using Hy-45% hydrogel solution.

Table S 4: Hy-45% hydrogel block.

Mass of hydrogel solution/(g)	Mass of hydrogel block/(g)	Mass of AA+BIS+irgacure in hydrogel solution/(g)	% Residual mass in TGA	Mass of AA+BIS+irgacure in hydrogel block /(g)	Maximum Percentage conversion/ (%)	Minimum Percentage conversion/ (%)
11	9.688	5.313	44.7	4.33	81.5%	74.7%

Maximum percentage conversion: Calculation was made under the assumption that **all of the** BIS+irgacure have reacted.
Minimum percentage conversion: Calculation was made under the assumption that **none of the** BIS+irgacure have reacted.

% hydrogel conversion in Hy-40% hydrogel block

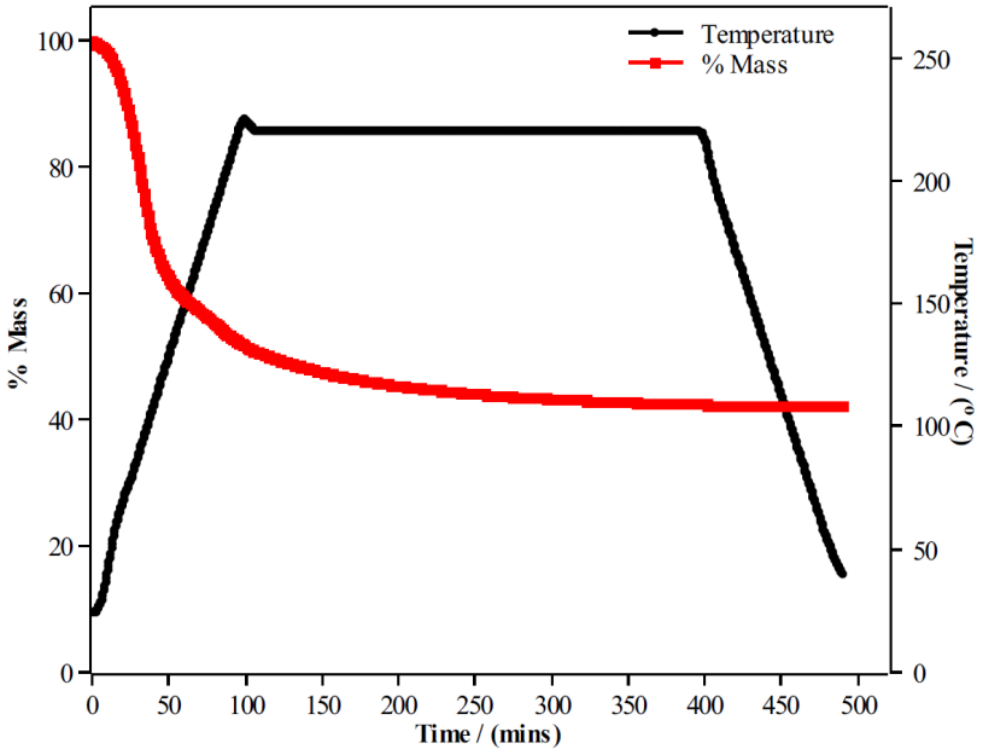

Figure S 9:TGA analysis of the Hy-40% hydrogel block that was prepared using Hy-40% hydrogel solution.

Table S 5: Hy-40% hydrogel block.

Mass of hydrogel solution/(g)	Mass of hydrogel block/(g)	Mass of AA+BIS+irgacure in hydrogel solution/(g)	% Residual mass in TGA	Mass of AA+BIS+irgacure in hydrogel block /(g)	Maximum Percentage conversion/ (%)	Minimum Percentage conversion/ (%)
10	8.06	4.33	42.53	3.43	79.2%	71.6%

Maximum percentage conversion: Calculation was made under the assumption that **all of the** BIS+irgacure have reacted.

Minimum percentage conversion: Calculation was made under the assumption that **none of the** BIS+irgacure have reacted.

% hydrogel conversion in Hy-30% hydrogel block

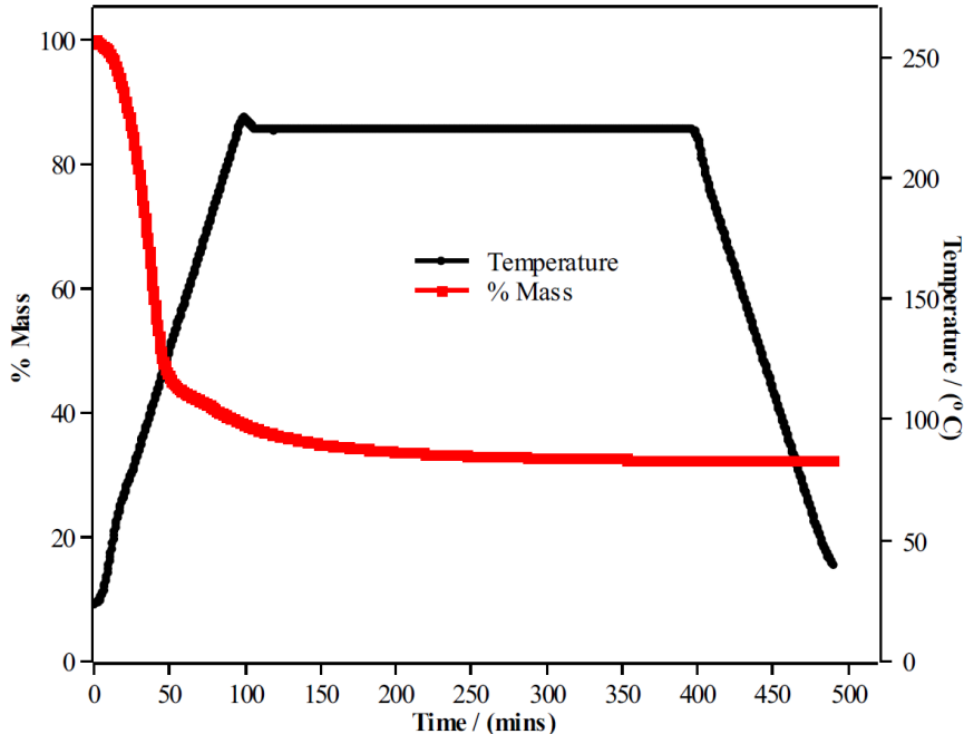

Figure S 10:TGA analysis of the Hy-30% hydrogel block that was prepared using Hy-30% hydrogel solution.

Table S 6: Hy-30% hydrogel block.

Mass of hydrogel solution/(g)	Mass of hydrogel block/(g)	Mass of AA+BIS+irgacure in hydrogel solution/(g)	% Residual mass in TGA	Mass of AA+BIS+irgacure in hydrogel solution /(g)	Maximum Percentage conversion/ (%)	Minimum Percentage conversion/ (%)
10	8.37	3.33	32.4	2.712	81.4%	71.5%

Maximum percentage conversion: Calculation was made under the assumption that **all of the** BIS+irgacure have reacted.

Minimum percentage conversion: Calculation was made under the assumption that **none of the** BIS+irgacure have reacted.

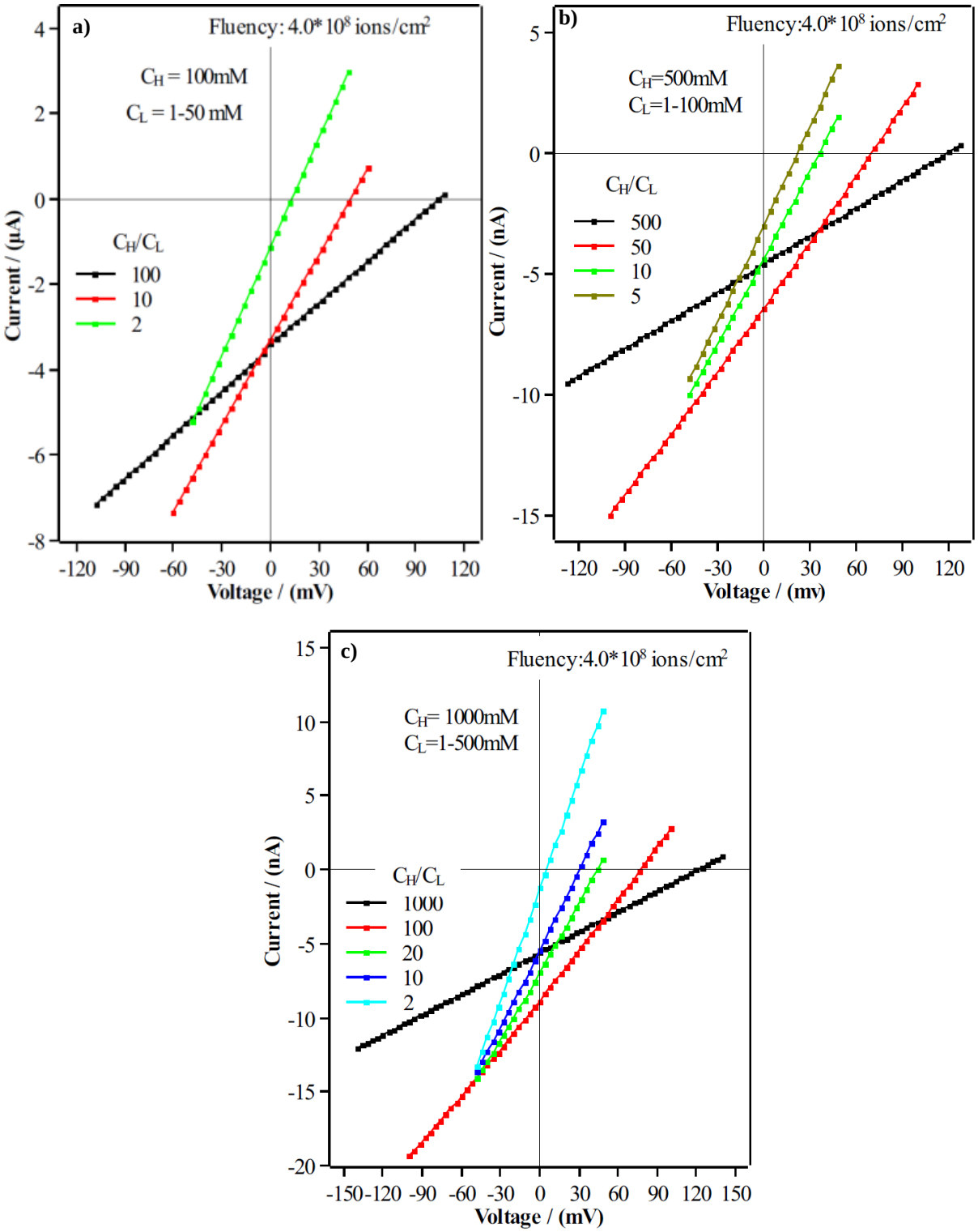

Figure S 11: (a-c) *I-V* curve at different C_H /C_L ratios. PI membrane having fluence of 4.0x10^8 pores/cm^2 was used in the investigation.

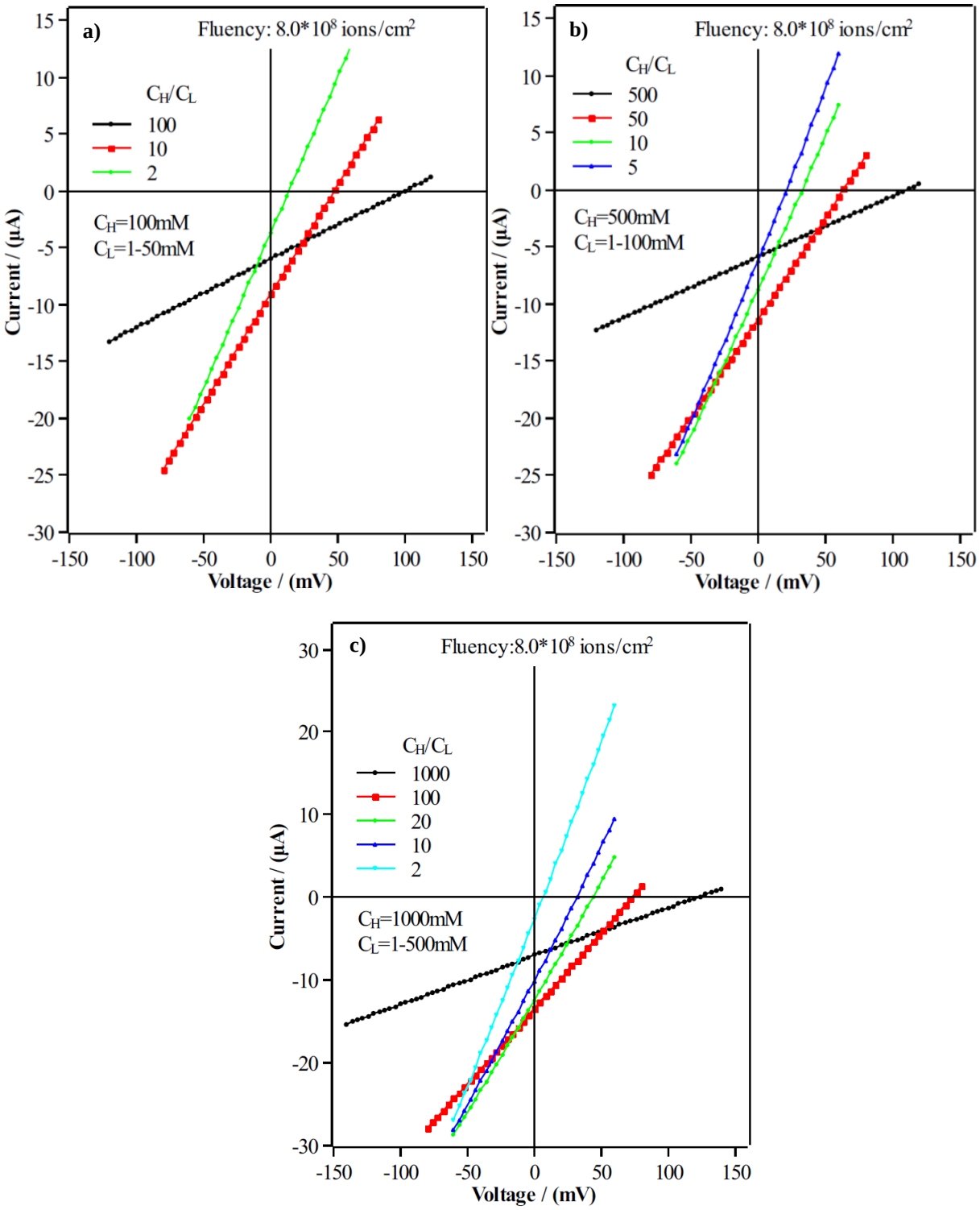

Figure S 12:(a-c) *I-V* curve at different C_H /C_L ratios. PI membrane having fluence of 8.0x10^8 pores/cm^2 was used in the investigation.

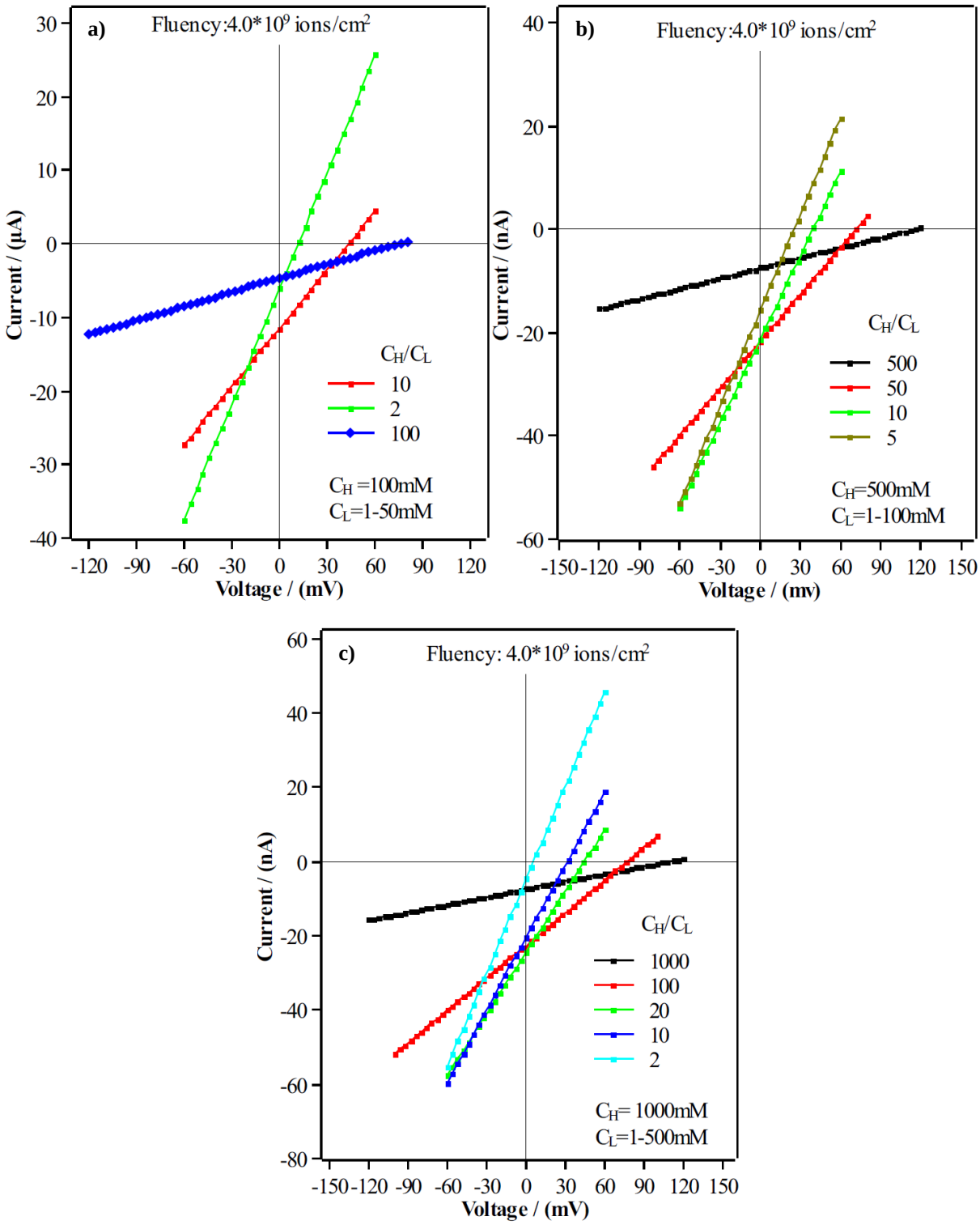

Figure S 13:(a-c) *I-V* curve at different C_H /C_L ratios. PI membrane having fluence of 4.0x10^9 pores/cm^2 was used in the investigation.

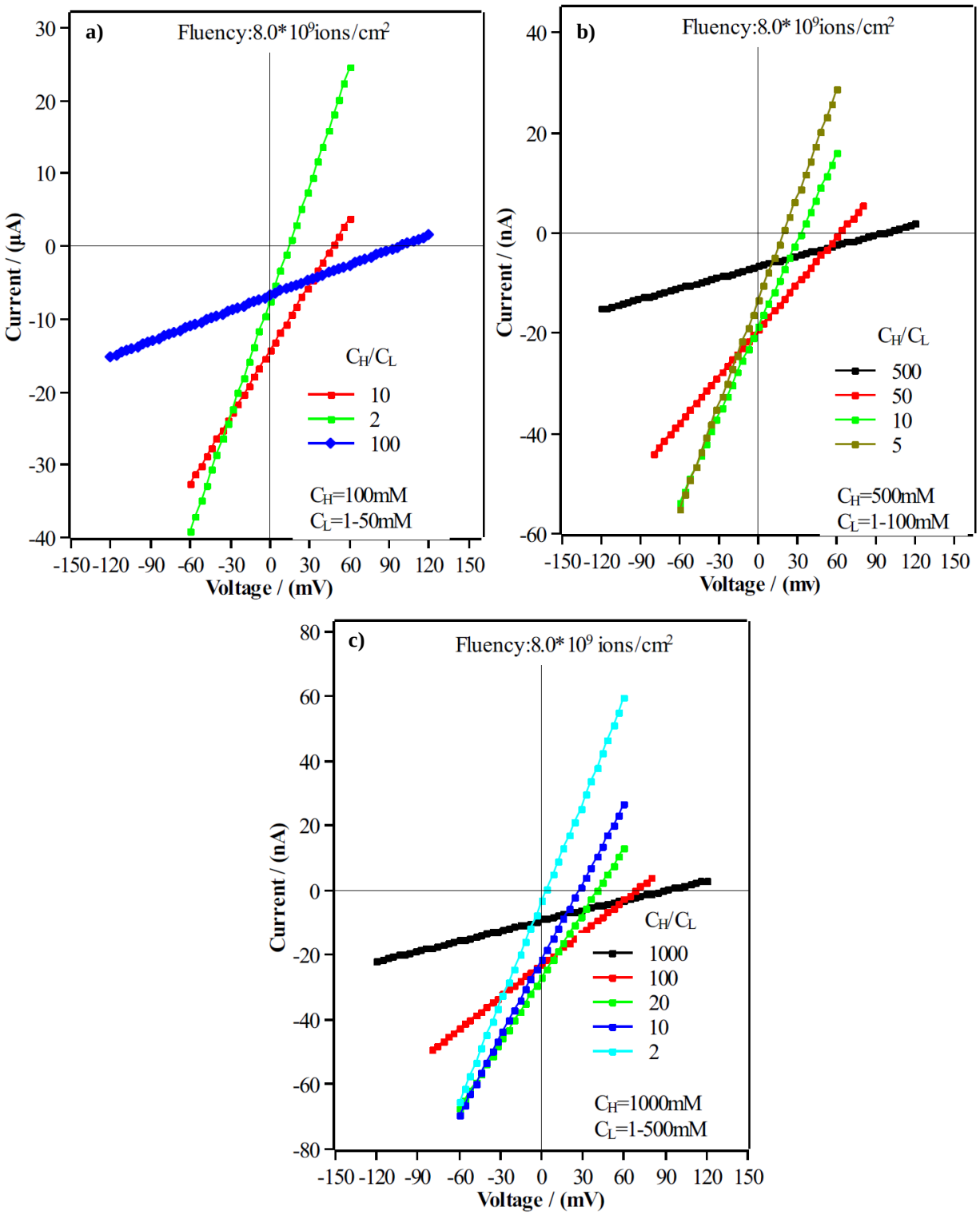

Figure S 14: (a-c) *I-V* curve at different C_H /C_L ratios. PI membrane having fluence of 8.0x10^9 pores/cm^2 was used in the investigation.

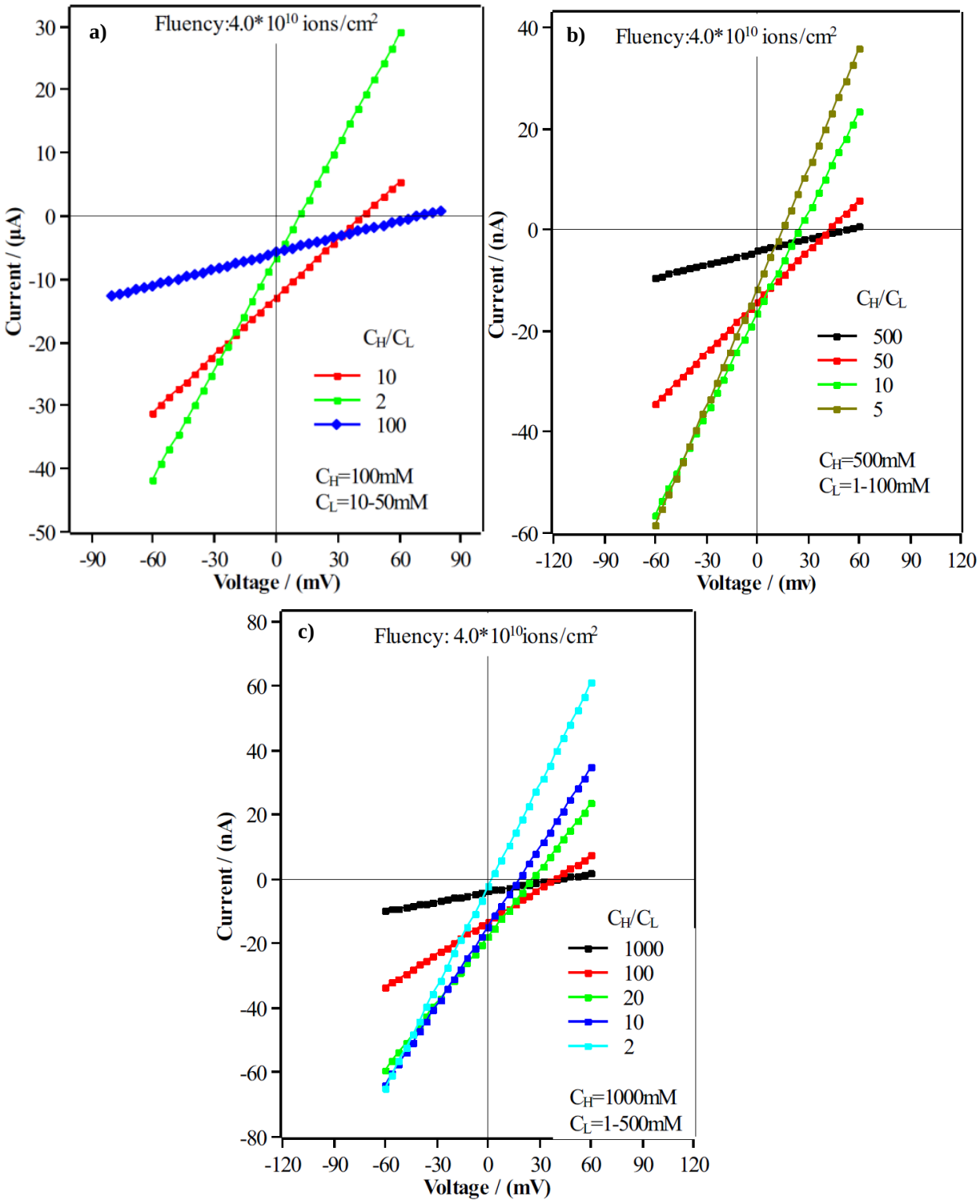

Figure S 15: (a-c) *I-V* curve at different C_H /C_L ratios. PI membrane having fluence of 4.0x10^{10} pores/cm^2 was used in the investigation.

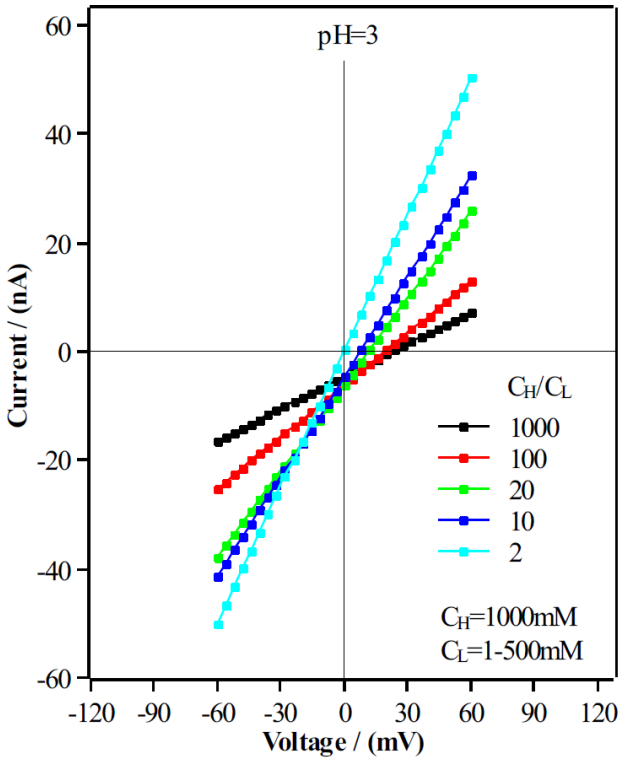

Figure S 16: *I-V* curve obtained at pH value of 3. PI membrane was used in the study.